Dynamic shoreline response to a shallow concentrated nearshore berm nourishment

C.J. Onnink

Delft University of Technology

TU Delft

Dynamic shoreline response to a shallow concentrated nearshore berm nourishment

by

C.J.(Casper) Onnink

In partial fulfillment of the requirements for the degree of

Master of Science
in Hydraulic Engineering

at the Delft University of Technology (TU Delft),
to be defended publicly on Tuesday September 15, 2020 at 15:00h.

Student number:	4301692	
Project duration:	October 2019 – September 2020	
Thesis committee:	Prof. dr. ir. S.G.J. Aarninkhof,	TU Delft, supervisor
	Dr. Ir. K. Brodie,	USACE, supervisor
	Dr. Ir. B. Bruder,	USACE, supervisor
	Dr. Ir. J.A. Hopkins	TU Delft, supervisor
	Dr. Ir. M.A. de Schipper,	TU Delft, chairman
	Dr. Ing. M.Z. Voorendt,	TU Delft, supervisor

An electronic version of this thesis is available at `http://repository.tudelft.nl/`.

Cover:
Sediment deposition in nearshore zone of New Smyrna Beach via a pipe outflow.
Source: www.surfline.com/surf-news/florida-pros-revel-man-made-sandy-slabs/47373

TU Delft

Acknowledgments

This Master thesis concludes seven years of study at the TU Delft. A period of hard-working, but most of all, an unforgettable and enjoyable period of my life. In this preface of the report, I would like to spend some time highlighting amazing (study-related) activities and people I have met.

What most certainly stands out are my trips aboard to The Gambia (2015), Cuba (2019), and the United States (2020). Studying at a well-known university such as the TU Delft really opens doors! Together with Sef and Kizjè, I learned how to survive in a third world country like The Gambia. After some lessons about how to conquer musquitos, malaria, food poison, it really was a fantastic trip. Absolute highlights are the workshops we gave at the secondary school at Janjanbureh, the visit of my brother and father, and a small holiday in Dakar, Senegal. My trip to Cuba was completely different. Surviving without nearly any internet and wíth defect software programs in a communistic country was inspiring (and sometimes frustrating). I would like to thank Bram, Jouke, and Joyce for sharing these fantastic memories. I most enjoyed the rock-paper-scissors games to decide who's turn it was to talk with our supervisor, the endless waiting for the school bus, and the sightseeing with my mom. Just before the Corona-lockdown, I visited the Field Research Facility in Duck to conduct an important part of my thesis. I absolutely enjoyed my staying at Nick, Benvy, and Yebo's house and the quality chats with my supervisors Kate and Brittany. Eventually, all three trips aboard were amazing experiences and contributed to my perspectives on life.

Regarding my thesis activities, I would like to thank my graduation committee at the TU Delft, consisting out of Matthieu, Stefan, Julia, Mark, Kate, and Brittany. Special thanks to Matthieu for all the weekly-meetings. Having you as a supervisor was a real asset to my personal and academic development. Your enthusiasm, dedication, and quality input helped me a lot. Furthermore, I want to mention Kate and Brittany, which whom I had plenty of meetings at 06 a.m. US timezone. That is dedication!

Lastly, I would like to thanks my family and friends for the moments during my study. From 'nog een biertje dan' and 'doei hé' at my sports association PC, to though times in which they had my back. Of course, studying at the TU Delft is synonymous with hard work, but you made it a lot more enjoyable! This thesis closes a period that was better than I could ever wished for. At this moment, I am ready to start a new chapter of my life. Enjoy reading!

C.J (Casper) Onnink
Delft, September 2020

Abstract

Worldwide, coastal regions are threatened by sea-level rise and an increasing number of extreme storm events as a result of climate change. Traditionally, hard engineering techniques were used for shoreline protection. However, due to the negative side effects at adjacent beaches, current strategies tend to focus more on sustainable, so-called soft solutions, such as nearshore berm nourishments. Although several manuals are available describing the preliminary design of nearshore berm nourishments, most of them are based on expert judgment and not on quantitative predictions. This can lead to design flaws and, therefore, to unnecessary costs. To overcome this problem, this research aims to increase the understanding of the development of nearshore berm nourishments in relation with the corresponding shoreline evolution. The shallow concentrated nearshore berm nourishment placed in 2018 at New Smyrna beach was used as a case study.

New Smyrna Beach, a city located in Volusia County, Florida, suffers from shoreline erosion and accretion to the local inlet. As a countermeasure, the inlet is regularly dredged and the obtained sediments are placed in the nearshore zone of New Smyrna Beach. The most recent maintenance operation included a sand placement of 350,000 m^3 and was monitored by a mini Argus-system, providing hourly imagery data of the nearshore zone. The data consisted of Snapshot, Timex, Variance, Brightest, and Darkest imagery data from August 2018 to September 2019. The dredging and nourishing activities started in the first week of August 2018 and continued until the last week of February 2019.

In three steps, the coordinates of the placement locations and position time-series of the berm/bar and shoreline were extracted from the Argus imagery data. In this thesis, the terminology berm/bar was used to describe both the nearshore berm and sandbar, as no separation between both features could be made using the Argus imagery data. First, the placement locations were obtained by a manual determination of the pipe outflow using georectified and merged Timex imagery, leading to a time-series of 87 daily position locations. Second, the berm/bar positions were found using the Bar Line Intensity Model (BLIM) in combination with georectified merged Timex imagery, resulting in 359 daily nearshore berm/bar position locations. The BLIM model extracts locations of persistent wave breaking from the imagery data by finding maxima in the image intensity profiles. Subsequently, the locations of persistent wave breaking are assumed to correspond with the crest of the berm/bar. Third, the shoreline positions were extracted via a manual determination approach using georectified merged Timex imagery, generating 165 daily positions. Before the extraction of the shoreline positions, the input images were adjusted to higher contrast and blue-tone levels. This led to increased visibility of the separation line between water and sand.

Behind the nourishment area, an offshore bar/berm movement and shoreline increase in the first six months was found via time-series analysis. After completion of the nourishment operation, an opposite berm/bar migration was found, and onshore movement occurred during the remaining seven months. Additionally, the shoreline positioning was stable for five months, after which it started eroding. Downdrift of the nourishment area, alternating erosion patterns up to 20 meters were found. Considering all alongshore sections, the maximum shoreline increase was nearly 80 meters and were observed one month after nourishment completion. The final shoreline increase was approximately 50 meters. In total, the beach gained more than 3,000m^2 of surface area, spread over an alongshore section of 1.2 kilometers.

The influence of the hydraulic forcing on the nearshore berm and shoreline migration was analyzed at the alongshore center of gravity of the nourishment, and two locations at the side of the nourishment. From time-series analysis, it was found that alongshore wave energy events corresponded with downdrift shoreline erosion. 72 % and 62 % of the total alongshore wave energy was related to erosive migration rates at respectively the south and the north side of the nourishment. At the alongshore center of gravity, the berm and shoreline migrations were related to the cross-shore wave energy events. It was found that during the nourishment activities, cross-shore wave energy was related to offshore berm migration, while after completion, the wave energy was related to onshore berm migration. Furthermore, during 34 % of the time, onshore berm migration corresponded with shoreline advance. In total, 33 % of the cross-shore wave energy could be related to this migration behavior.

By reflecting on the results, it is suggested that the theoretical Feeder and Leeside effects played an important role in shoreline dynamics. The Feeding effect is characterized by shoreward propagating accretionary waves (SPAWs) while the Leeside effect is depicted by shoreline erosion patters downdrift of the nourishment induced shadow zone. Contrary to most nearshore berm nourishments, the placement at New Smyrna Beach resulted in a significant increase of 45,000 m^2 of the sub-aerial beach. Although not validated in this study, it is hypothesized to be a result of the high cross-shore density of the nourishment, $\approx$ 875 m^3/m, and shallow placement location of 4-5 meters.

Contents

Acronyms and Abbreviations

Acronym / Abbreviation	Description
ANN	Artificial neural network
BLIM	Bar line intensity mapper
CCD	Color channel divergence
CG	Center of Gravity
CIRN	Coastal imaging research network
DOC	Depth of Closure
FRF	Field Research Facility
MHHW	Mean Higher High Water
MHW	Mean High Water
MLLW	Mean Lower Low Water
MLW	Mean Low Water
MSL	Mean Sea Level
NAD83	North American Datum of 1983
NADV88	North American Vertical Datum of 1988
NDBC	National Data Buoy Center
NOAA	National Oceanic and Atmospheric Administration
NSB	New Smyrna Beach
PIC	Pixel intensity clustering
RGB	Red Green Blue
ROI	Region of interest
SLIM	Shore line intensity maximum
SPAW	Shoreward propagating accretionary wave
Timex	Time exposure
USACE	United States Army Corps of Engineers

1 Introduction

1.1. Thesis motivation

Coastal regions are threatened by sea-level rise and an increasing number of extreme storm events as a result of climate change. Nearly 20 % of the world population, which accounts for 1.4 billion people, lives within a 25 kilometer radius of the coastline (Williams et al., 2018). Furthermore, 4.7 trillion in assets is exposed to coastal flooding. Both these numbers are likely to increase in the future due to socio-economic and demographic development. This makes coastal protection, to protect these people and assets, more relevant than ever.

One of the places that suffer from the effects of climate change is New Smyrna, which is located on Florida's Central Atlantic Coast. The local beach is prone to hurricanes (Bruder et al., 2019a) and suffers from erosion, which threatens private development, recreational interests, and sea turtle nesting habitats (Clark, 2019). To counteract shoreline retreat, the beach is replenished regularly. According to the American Shore and Beach Preservation Association, several beach fill and nearshore nourishment projects have been executed over the years (ASBPA et al., 2018). However, the most effective nourishment strategy for beach restoration is not yet found, causing unnecessary costs, recreational hinders, and environmental damage (Figure 1.1).

Figure 1.1: Beach erosion and property damage due to Hurricane Jeanne (2004) at New Smyrna Beach (left). The filling of sandbags which act as a temporary seawall (right).
Retrieved from: www.city-data.com/disaster-photos/11864.html

1.2. Problem analysis

Until the nineties, hard engineering techniques (e.g., breakwaters, sea walls, groynes, revetments) were traditionally used for shoreline protection. These man-made structures locally protect the coast by absorbing wave energy, limiting erosion rates, and reducing the risk of floods. The lifetime of these structures is mostly in the order of decades. However, the construction of these structures can be costly. The main disadvantage of hard engineering techniques are the potential negative side effects; in many cases, the interventions lead to significant erosion on adjacent shorelines. Furthermore, hard solutions are not preferred for recreational

issues, as it brings discontinuities in the natural look of the beach. Therefore, current strategies tend to focus more on sustainable, so-called soft solutions(Hamm et al., 2002).

Soft engineering focuses on the use of ecological principles. This means that the main goal is to reduce erosion, but at the same time achieves stabilization and safety of shorelines while enhancing habitat, improving aesthetics, and saving money (Caulk et al., 2000). Illustrations of soft engineering are nourishments, dune regeneration using vegetation, creating marshland, and beach re-profiling. One of the most used techniques is shore nourishment. Opposite to hard engineering techniques, the shoreline retreat is combated with a supplement of sediments. The nourishment fills the shortage in the sediment budget, leading to a temporal reduction of the original shoreline erosion rates. However, because the origin of erosion is not eliminated, nourishments have to be executed periodically for efficient coastal protection.

Maintaining or increasing the shoreline is the primary goal of most nourishment projects, which can be achieved by creating a nearshore berm or performing beach nourishment. The efficiency of nearshore berm nourishments, defined by the volume of sand reaching the coast within five years, is estimated between 20 and 30 percent (Van Rijn, 2011). Furthermore, it is difficult to predict as it depends on site-specific conditions (Brutsché et al., 2019). Beach nourishments are known to be more effective in reinforcing the shore. However, these kinds of nourishments also cause significant hinder to beach activities and are more expensive. For this reason, nearshore berm nourishments are increasingly proposed nowadays.

Although several manuals are available describing the preliminary design of the nearshore berm nourishment, most of them are based on expert judgment and not on quantitative predictions (Hamm et al., 2002). From a societal point of view, this is a problem. Contractors can only give estimations about the amount of sediment reaching the coast. If less sediment than expected reaches the coast, this results in a lower level of coastal protection. Consequently, the vulnerability of assets and the environment increases. Furthermore, dredging activities have to take place more frequently than expected, which leads to unnecessary costs. A surplus of sediments enhances the shoreline to a level that is potentially higher than required. Although providing extra protection, the money needed cannot be used for other societal purposes.

Due to climate change, the sea level is rising, and there is an increased likelihood of more extreme storms. Together with the negative impacts of hard engineering techniques, a better understanding of nearshore berm nourishments and associated shoreline responses are important to improve coastal management strategies

1.3. Research objective

This research aims to increase the understanding of the development of nearshore berm nourishments in relation with the corresponding shoreline evolution.

1.4. Scope

This study focuses on the nearshore berm nourishment placed in 2018 at New Smyrna Beach. By investigating the berm and shoreline development, it is desired to increase the predictability of subsequent nearshore nourishment at this location.

1.5. Research questions

The research objective is converted into the following main research question:

How does a nearshore, concentrated berm nourishment influence the beach during and after nourishment activities?

The following sub-questions support the research question:

1. How can the nearshore berm and the shoreline positions be optimally extracted from the New Smyrna Beach imagery data?
2. How did the nearshore berm and shoreline migrate during and after the nourishment activities?
3. What is the influence of the hydraulic forcing on the nearshore berm and shoreline migration?

Together, the three sub-questions answer the main research question. Additionally, it provides the opportunity to reflect on the Feeder and Leeside hypotheses.

1.6. Outline and Methodology

The outlines and general methodology of each chapter are stated point-wise.

- Chapter 2: the report starts with a literature review to provide a theoretical basis for answering the research question. Relevant findings on nearshore berm migration behavior and related shoreline processes are described. Additionally, coastal monitoring and, in particular, coastal imaging are discussed.
- Chapter 3: data acquisition and the New Smyrna Beach site are described in the third chapter of this thesis. After a site introduction, the local hydrodynamics and morphodynamics are discussed. This includes the description of the wave height, wave direction, water levels, and the bathymetry. Finally, the chapter concludes by stating relevant nourishment information and explaining the site imagery collection.
- Chapter 4: the first sub-question "How can the nearshore berm and the shoreline development be optimally extracted from the New Smyrna Beach imagery data?" is answered by comparing multiple data extraction methods. The available imagery data contains shoreline and berm positions, which need to be obtained most accurately. The berm position can be found using a pixel-intensity based extraction model, but the question remains which imagery format to use. Four available imagery output types are compared to find the type with the most consistent output. Subsequently, several shoreline extraction models are available, each based on different imagery characteristics and using specified output formats. Four available models are compared to find the model resulting in the most accurate and consistent shorelines for New Smyrna Beach.
- Chapter 5: the second sub-question "How did the nearshore berm and shoreline migrate during and after implementation of the nourishment?" is answered by a theoretical description and a description based on the time-series analysis. The first describes the theoretical berm migration based on the local hydraulics and the placement location, while the theoretical shoreline migration is defined by the Feeder and Leeside effects. The latter quantitatively describes the nearshore berm and shoreline migration in cross-shore and alongshore directions by analyzing the time-series. Furthermore, the evolution of beach width, beach surface area, and alongshore spreading are stated.
- Chapter 6: the third sub-question " What is the influence of the hydraulic forcing on the nearshore berm and shoreline migration?" is answered by relating the cross-shore and alongshore wave energy fluxes to the nearshore berm and migration behavior. In line with Chapter 5, both the theoretical influence and influence based on the time-series are analyzed. The theoretical influence of the hydraulic climate on the nearshore berm and shoreline is described via the Feeder and Leeside effects. Subsequently, the time-series are compared, and it is tried to find indications of both theoretical effects.
- Chapter 7: result interpretations, the limitations, and uncertainties are debated in a discussion. The chapter reflects on the berm and shoreline migration patterns and compares the behavior to other nourishment sites. Furthermore, this chapter is used to reflect on the Feeder and Leeside hypothesis.
- Chapter 8: the main research question, "How did the nearshore berm nourishment influence the New Smyrna Beach during and after nourishment activities?", is answered in this chapter. Additionally, recommendations for future nearshore berm nourishment at New Smyrna Beach and research suggestions for the Feeder and Leeside effects are given.

2

Theoretical background

The literature review provides the basic concepts of nearshore berm nourishments. The Chapter starts by stating the used definitions, followed by a description of nearshore berm migration behavior in alongshore and cross-shore direction. Subsequently, the theoretical shoreline response to a nearshore berm nourishment is discussed. The Chapter concludes by describing coastal monitoring systems.

2.1. Definition nearshore berm nourishment

A submerged placement of sediments in the nearshore area is called a nearshore berm nourishment (Huisman et al., 2019). Commonly, the nearshore berm nourishment is placed seaward of the outer bar (Figure 2.1, Dronkers (2016)). Synonyms for a nearshore berm nourishment are shoreface nourishment or just berm nourishment. The deposited sediments form a berm, which is also referred to as sandbar or sandbank. In this report, the terms nearshore berm nourishment and berm are used to describe the placement method and local bed elevation due to the nourishment. Already existing shoals are called (sand)bar.

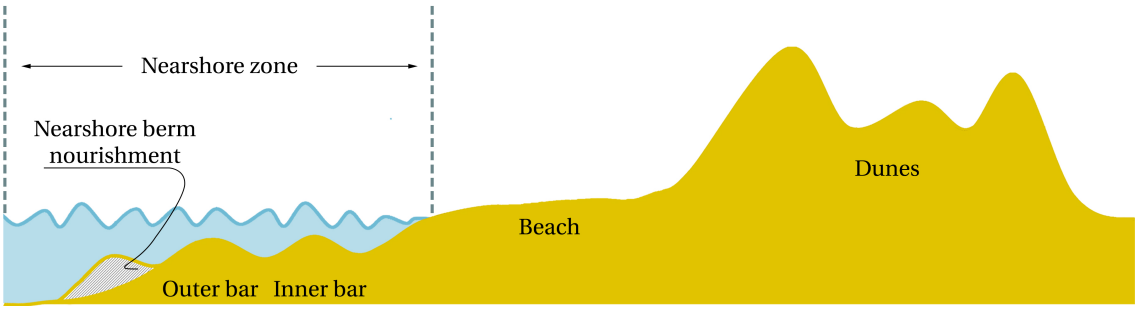

Figure 2.1: A cross-shore beach profile highlighting the nearshore zone and a commonly used nearshore berm nourishment location. Adapted from: van de Ven and van Zelst (2019).

2.2. Nearshore berm nourishment behavior

The behavior of the placed berm depends on local hydrodynamic and morphodynamic conditions and is difficult to predict (Brutsché et al., 2019). Several project sites, mostly in the United States, Australia, and the Netherlands, are extensively monitored and researched. In general, the spatial evolution of a nearshore berm can be divided into diffusion, alongshore migration and cross-shore migration.

2.2.1. Berm diffusion

Berm diffusion is the spatial spreading of sediments. Over long enough time scale, nearshore berm nourishments will diffuse in the alongshore and cross-shore direction. The extent is determined by the spatial characteristics of the nourishment and the hydrodynamic climate. In general, the larger the nourishment height and the smaller nourishment width and the more energetic wave conditions, the stronger the diffu-

sion. Additionally, if the nourishment grain size differs from the native sediments, this influences the diffusion processes. A smaller relative grain size speeds up the diffusion of the nourishment (Hamm et al., 2002).

Huisman et al. (2013) studied eight field sites in the Netherlands to isolate the advective and diffusive components of nearshore nourishments. The paper states that the diffusive character of the berms is the leading cause of coastline perturbations. Additionally, it concludes that the berm diffusion is more strongly correlated with the severity of the wave climate than with the spatial characteristics of the nourishment, as the diffusion rates were approximately the same for all nourishments.

2.2.2. Alongshore berm migration

Advection or alongshore berm migration is the movement of the berm in alongshore direction and is not studied in great detail yet (Huisman et al., 2013). The alongshore migration is triggered by waves approaching the coast with an angle of incidence. The resulting sediment transport causes the berm to advect (Hamm et al., 2002). In correspondence with the berm diffusivity, the alongshore migration is accelerated if the berm grain size is smaller than the native sediments (Hamm et al., 2002).

2.2.3. Cross-shore berm migration

A berm can be classified into two categories: a stable berm or an active berm. Over time, an active berm migrates towards the shore while a stable berm remains at the placement site. An overview of nearshore berm nourishments and observed migration from 1935 to 2010 is given in Appendix A.

According to Hands and Allison (1991), the stability or movement of the berm can be estimated by the closure depths of Hallermeier. Berms that are placed in the littoral zone are defined as active, whereas stable berms are found in the offshore zone. In the shoal zone, both active and stable berms are found. Additionally, Hands and Allison developed a second method. It is found that the berm movement is correlated with near-bed velocities. When 75 velocity-percentile exceeds 40 centimeters per second, the berm should be active. The same holds when the 95-velocity percentile exceeds 70 centimeters per second. During field tests, it was observed that using the depth of closure may lead to conservative results (Brutsché et al., 2019).

Alternatively, during a study at the FRF in Duck, NC, a relation between the Dean number and the berm migration behavior was established. If the Dean Number, defined as the wave height divided by the fall velocity times the period, is found to be larger than 7.2, the berm will migrate offshore. Otherwise, it will migrate onshore (Larson and Kraus, 1992). To validate the study, the criteria were tested to a nearshore berm at Silver Strand, California. The results validated the criteria obtained at the FRF as it successfully predicted the migration behavior of the nearshore berm (Larson and Kraus, 1992). Nowadays, this methodology can still be used to design a nearshore berm (Brutsché et al., 2019).

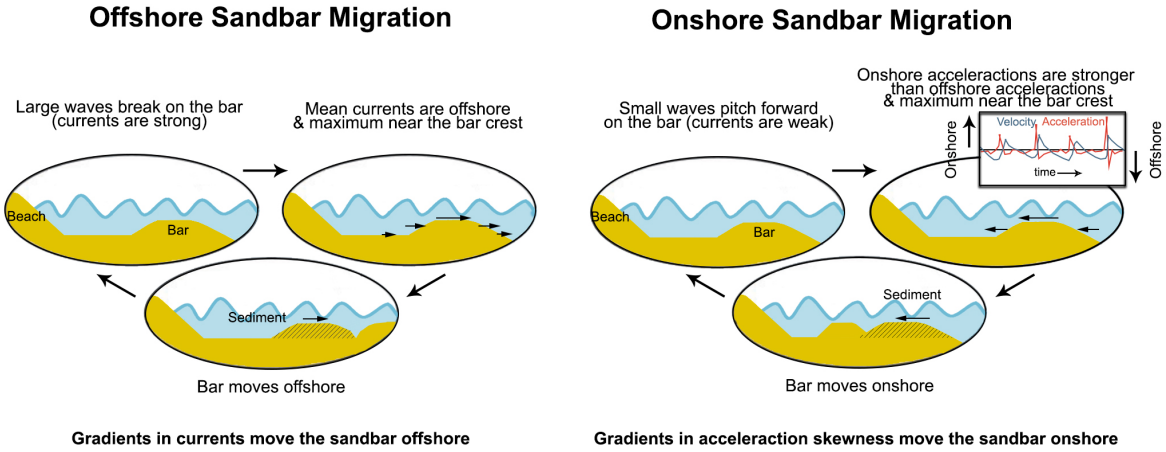

Figure 2.2: Left: large waves break at the sandbar, causing an offshore-directed current. The gradient in the undertow velocity results in an offshore movement of the berm. Right: non-breaking pitched forward waves are generating more substantial onshore accelerations than offshore accelerations, causing an onshore berm migration. Adapted from Hoefel and Elgar (2003).

Besides the migration trend caused by the placement location, berm development is also influenced by variabilities in the wave climate. In general, offshore berm migration is found during significant wave breaking (Figure 2.2 A) and onshore migration during a calm wave climate (Figure 2.2 B). Offshore migration is caused by gradients of the undertow velocity, which in turn, is generated by wave breaking on the bar (Hoefel and Elgar, 2003). On the other hand, skewed non-breaking waves on top of the bar crest are causing an onshore bar migration during a more mild wave climate (Hoefel and Elgar, 2003). The strength and duration of the hydraulic conditions determine the related migration velocities. During constant wave conditions, the beach profile tends to develop to the equilibrium shape (Cheng et al., 2016).

2.3. Shoreline response

Stable and active berms both influence the shoreline differently. Stable berms remain at the placement location and have relatively low diffusion rates compared to active berms (Section 2.2.3). Additionally, stable berms shelter the shoreline from high energy events, which is the so-called Leeside-effect (Otay, 1994)). Besides, the calmer wave climate leads to a reduction of the local alongshore transport capacity, which allows sediments to settle more easily. Downdrift, adjacent coastlines may suffer from erosion when the transport capacity picks up (Figure 2.3, left, van Rijn and Walstra (2004)).

As an example, an 8-year study of a nearshore berm nourishment at Perdido Key, Florida, showed minimal displacement (Brutsché et al., 2019). Simultaneously with the nearshore berm nourishment, a beach nourishment was placed. Site investigations and additional wave modeling confirmed that the berm acted as a breakwater, reducing the wave energy reaching the shoreline. Although several hurricanes passed by, 84 % of the initial beach nourishment was still in place after three years (Work et al., 1996). The final bathymetry survey was executed at the end of the study. After eight years, 41% of the beach nourishment remained (Browder and Dean, 2000).

Active berms migrate towards shore and diffuse over time (Section 2.2.3). Similar to stable berms, active berms also protect the shoreline from incoming wave energy. However, due to smaller water depth at the bar crest, the Leeside-effect already holds during a calmer wave climate. Additionally, active berms feed the shore with sediments. Whereas larger waves break at the seaward side of the berm, an increase in sediment transport is caused by shoaling non-breaking waves on top of the bar. The non-breaking waves will develop a pitch forward shape, which leads to a net shoreward near-bed velocity (Figure 2.2, right & Figure 2.3, right) and eventually shoreline accretion. The remaining waves behind the berm will lead to less stirring and lower wave-induced return flow, which causes offshore transport to decrease (Delft Hydraulics (2001), van Rijn and Walstra (2004)).

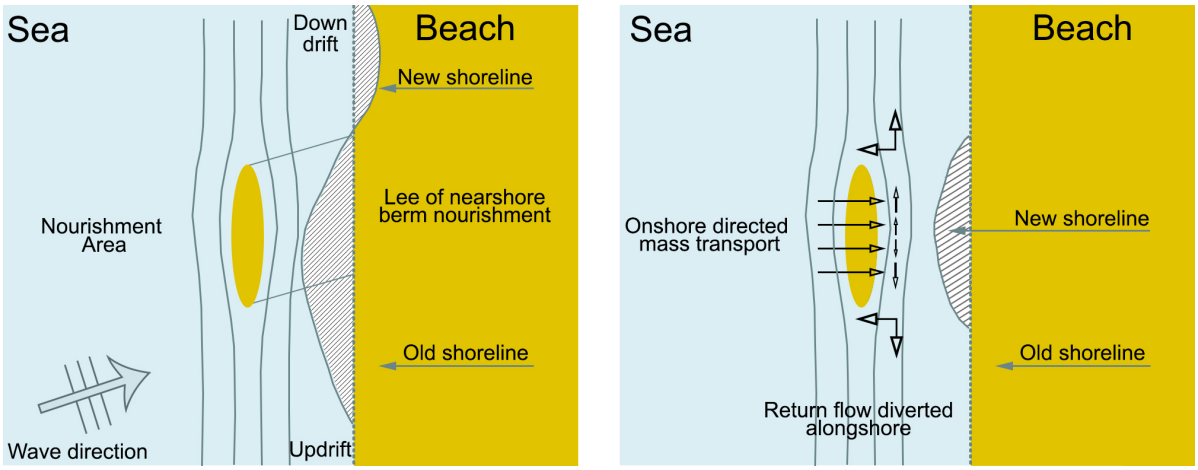

Figure 2.3: Expected shoreline change due to the Leeside-effect (left) and Feeder-effect (right). The shoreline is protected from incoming wave energy by the Leeside-effect. Additionally, it lowers the alongshore transport capacity, which allows sediments to settle. The Feeder-effect describes shoreline accretion due to onshore migration of sediments from the nourishment and a decrease in offshore transport capacity. Adapted from: van Rijn and Walstra (2004).

In 2009, a nearshore berm nourishment was executed in Fort Myers Beach, Florida, near the Northwest part of the island. The material consisted of up to 16 % fine material. During the monitoring period, it was found that the berm migrated in shoreward direction. Berm evaluation was influenced by high energy events, resulting in an accelerated equilibration process. After four years, the profile was returned to the pre-nourished dynamic equilibrium. Fort Myers Beach width was enlarged as a result of the feeding effect of the berm. Additionally, adjacent beaches also benefited from the dispensed sediments and gained in width. The dry beach grain size remained constant during the same over the four-year study, indicating an offshore movement of the fines (Brutsché et al., 2019).

2.4. Coastal monitoring

To gain insight into nourishment developments and resulting beach response, it is necessary to understand the processes happening in the nearshore zone. Traditionally, coastal monitoring is done by waterborne vessel as ships and jet skis and delivers accurate bathymetry data. To estimate the performance of a nearshore berm nourishment, Beck et al. (2012) suggests a semi-annually monitoring schedule throughout 1 to 3 years. However, to be able to understand the behavior during individual erosive events, more high-frequency monitoring is needed. Due to high costs and impractical working conditions during storm events, traditional surveying methods do not suffice. A preferred method for obtaining the necessary nearshore data is via optical imaging of the nearshore(Hamm et al., 2002).

Coastal imaging provides imagery data with a high spatiotemporal resolution at low costs relative to traditional monitoring methods. After processing, the imagery data can be used for coastal analysis. Examples are CoastalCOMS, Coastal SNAP, and Argus Coastal Monitoring.

The most established system, ARGUS, was initiated in 1980 by the Coastal Imaging Lab of Oregon State University. After continuous developments, the first station was set up in 1992 in Yaquina Head, USA (Holman and Stanley, 2007). The Argus system consists of several video cameras connected to a host computer and is installed on top of a specially designed tower. As the construction and installation of the tower and system are time-consuming and costly, the system is only cost-effective for long-term projects, ranging from multiple years to decades (Bruder et al., 2019b).

Dr. John Stanley and Dr. Shawn Harrison developed a mini Argus-system at the United States Geological Survey Institute to reduce the infrastructure barrier to entry (Bruder et al., 2019b). The miniaturized system utilizes the same architecture as the Argus system, but can be rapidly deployed and is with $6000 often cost-effective. Instead of designing and constructing the Argus-tower, the mini Argus system makes use of existing high rise buildings to match the spatial scope of the Argus system. So far, there are approximately 50 (mini)

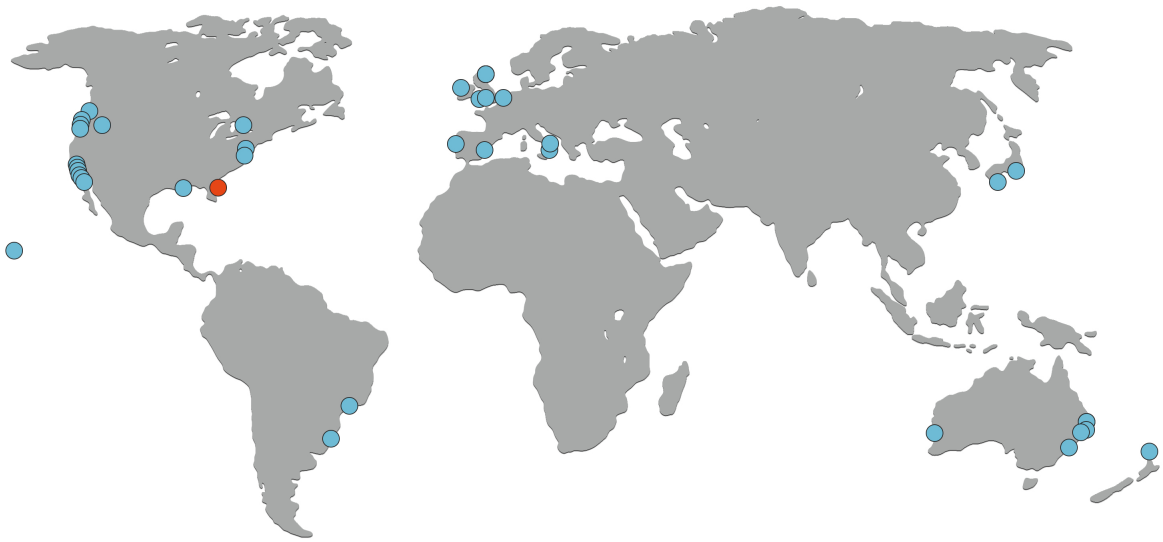

Figure 2.4: The world map displaying (former) Argus project (blue) and the New Smyrna Beach nourishment project (red).

Argus stations. Most of them are located in The United States, Europe, and Australia (figure 2.4) and aims to measure the change of shoreline in time. However, there is a wide variety of other monitoring goals. Popular are the approximations of sandbar locations, nearshore morphology and bathymetry, the behavior of rip currents, and the effectiveness of nourishments.

The (mini-) Argus system delivers five output types: Snapshot, Time-averaged image, Variance image, Brightest image, and a Darkest image.

- The Time-averaged image (Timex) is the average image during the compiling time of the Argus-system. Timex imagery are often used for extracting sandbar (Lippmann and Holman, 1989) and shoreline locations (Holman et al., 1993). Namely, one of the most noticeable features in Timex imagery are locations of persistent wave breaking. Because waves tend to break at certain wave height to water depth ratio, wave breaking is closely tied to the underlying bathymetry. In an unsaturated wave field, the first waves start to break at the most offshore sandbar, and the last waves will release their energy at the shoreline. Due to the averaging effect of the Timex, wave breaking appears as a bright band along the shore and is clearly visible adjacent to darker regions of less wave action (Holman et al., 1993).
- The Variance imagery, computed by time-standard deviation within the compiling time, are also occasionally used for the extraction sandbar and shoreline locations (Guedes et al., 2011). Variance imagery show change within the 10 minute sampling period and, therefore, can filter out non-changing features. However, the results of the Timex and Variance images are not necessarily the same. Regarding the extraction of sandbar locations, Variance images often lead to a more offshore location compared to Timex (Guedes et al., 2011).
- The use of the Brightest and Darkest imagery is still the subject of experimentation (Holman and Stanley, 2007). The Brightest imagery displays the maximum intensities during the sampling time and can be related to maximum wave run-up. Additionally, Darkest images, displaying the lowest intensities during sampling time, can be used for tracking more dark features in the sea, like sediment plumes and floating debris.

3

Data acquisition and site description

This Chapter starts with introducing the New Smyrna Beach site. Subsequently, the hydrodynamics and morphodynamics at the start and during the nourishment activities are discussed. This includes a bathymetry overview of August 2018 and the wave heights, wave directions, and water levels from August 2018 to September 2019. The Chapter concludes with specifying the site imagery collection and the stating of information about the most recent nourishment (August 2018 – March 2019).

3.1. Introduction

New Smyrna Beach is a beach town in Volusia County, Florida, and houses approximately 28,000 inhabitants. It is located on a barrier island and is enclosed by the Atlantic Ocean on the east-side, the Ponce de Leon Inlet at the north- and west-side. New Smyrna Beach has a humid subtropical climate, resulting in hot, humid summers and dry, mild winters.

At high tide, sediments are transported into The Ponce de Leon Inlet, causing chronic shoaling. Additionally, the area is prone to high energy wave events, causing erosion to the shoreline (Clark, 2019). The shoreline retreat threatens private assets and pressurizes recreational activities (Bruder et al., 2019a). To counter the shoaling effect, The Ponce de Leon Inlet is regularly dredged. The obtained sediments are used to strengthen the coast. Most recent maintenance dredging and nourishing operation was awarded to Cavache Inc in June 2018 by the US Army Corps of Engineers (USACE). The $ 8.55 million contract included the dredging of the Ponce de Leon Inlet and the placement of excavated material in the nearshore of New Smyrna Beach. Figure 3.1 illustrates the planned dredging route and placement template. The dredging activities (August 2018 – March 2019) and the subsequent response of the coast were monitored using a mini Argus-system. In September 2019, the monitoring stopped, and the mini Argus-system was uninstalled.

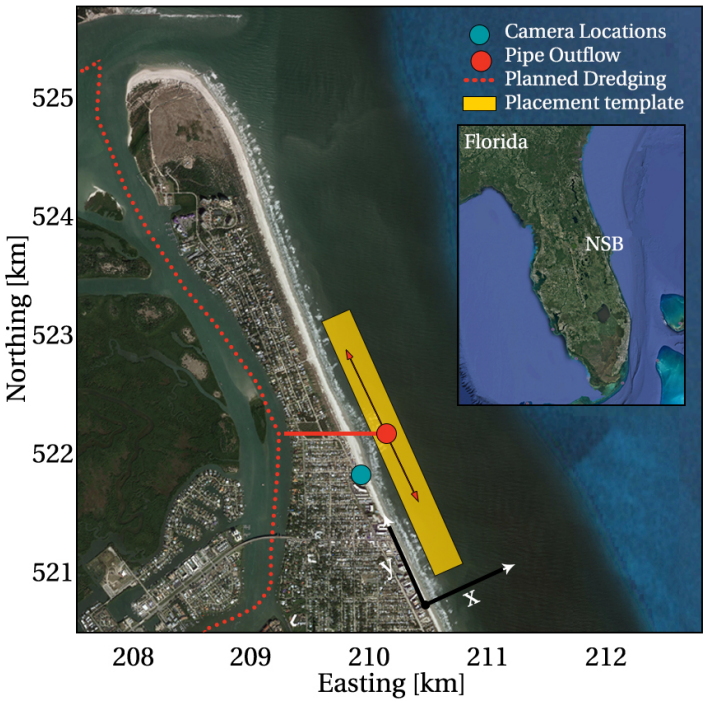

Figure 3.1: A satellite image of New Smyrna Beach and the Ponce de Leon inlet with the planned dredging and nourishing activities. The coordinates are NAD83/Florida East (km) coordinate system. Adapted from: Bruder et al. (2019a).

3.2. Hydrodynamics

The wave climate for New Smyrna Beach from July 2018 to October 2019 was obtained from the closest wave buoy, station 41009, of the National Data Buoy Center (NDBC). The buoy, located 90 kilometers south and 30 kilometers offshore of New Smyrna Beach, records, among others, the wave direction of the dominant waves, significant wave height, and dominant wave period every 10 minutes. In addition, water level information was extracted from the closest station, 8721120 of the National Oceanic and Atmospheric Administration (NOAA). The station is positioned at Daytona Beach, 13 kilometers north of New Smyrna Beach. Harmonic constituents deduced from the 1983 -2001 epoch of Daytona Beach were also obtained from the NOAA.

The wave climate had to be transformed from offshore to nearshore to explain morphodynamic changes (Chapter 5). The transformation of the wave climate (buoy 41009) was done using linear wave theory. In this Section, only the results are described. A detailed description of the wave transformation process is given in Appendix C. The resulting nearshore dominant wave directions and nearshore significant wave heights are displayed in Figure 3.2 and Figure 3.3. The mean significant wave height was calculated at 1.50 meters (August 2019 – September 2019). From June till August, the wave height was well below average. In the remaining months, the wave height was more variable and had a maximum of 9.0 meters in September 2019, when Hurricane Dorian approached the coast.

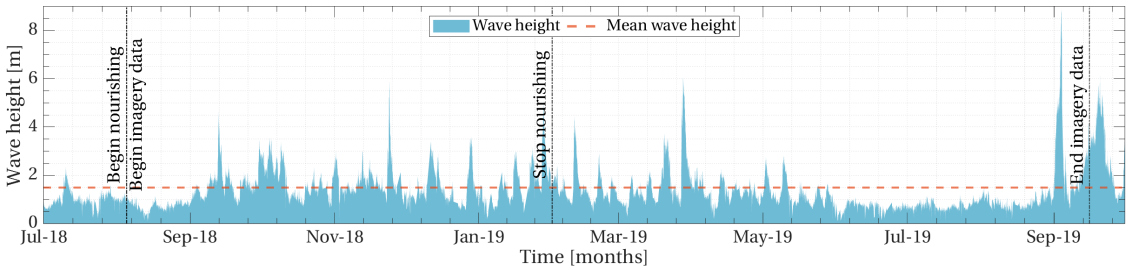

Figure 3.2: The nearshore significant wave height and mean wave height at NSB from July 2018 to October 2019 in meters.

The wave directions and shoreline orientation are illustrated in degrees and cardinal directions (Figure 3.3). The direction indicates the position from which the waves were coming. In nautical convention, the wave direction varied between 45 and 90 degrees, implying an angle of incidence between -20 and 25 degrees relative to the shore normal. From June till August, the waves were coming more from the East compared to the remaining months of the year. In general, the observed water levels at Daytona beach vary between

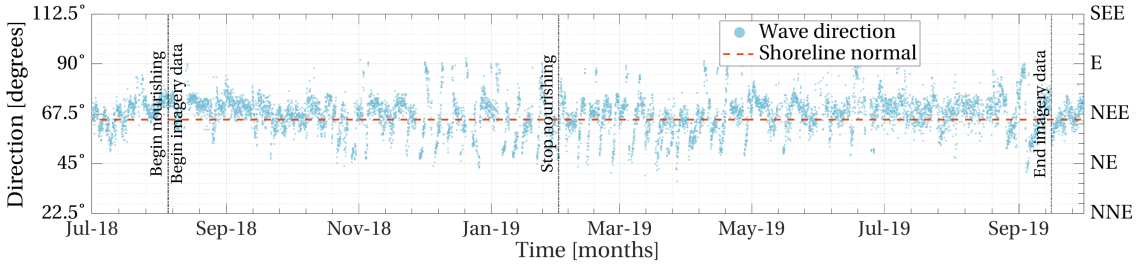

Figure 3.3: The nearshore wave direction of the dominant waves at NSB from July 2018 to October 2019 and shoreline orientation in degrees and cardinal directions.

+0.7 and -1.3 meters. However, local water level extremes went up to + 1.4 and -2.2 meters relative to NADV88 (Figure 3.4). The extremes often corresponded with energetic wave conditions (Figure 3.2) and, therefore, are the likely result of significant winds and low atmospheric pressure during storms. On a larger scale, a weekly signal caused variations in the water levels. Due to the different geographic locations, the water levels at New Smyrna Beach may be lagged compared to the water levels at Daytona Beach. However, no substantial water level differences were expected because both the collecting station and New Smyrna Beach are not situated in estuaries or have complex bathymetries.

A reconstruction of the tide at Daytona Beach was made using the principle of superposition. The used local

harmonics can be found in Appendix B. The two largest are the principal lunar and solar constituents. Both contributed significantly to the semi-diurnal tide at Daytona Beach. Together with the water levels, the daily low tide and high tide estimations are illustrated in Figure 3.4. All levels are given in meters and are relative to the NAVD88. With a Mean Higher-High Water level (MHHW) of 0.477 meters and a Mean Lower-Low Water level (MLLW) of -0.873 meters, the maximum mean tidal range was found to be 1.35 meters. The Mean Sea Level (MSL) was calculated at -0.242 meters. The surge caused the water level to deviate from the tide, with deviation peaks up to 1.0 meter (Figure 3.4).

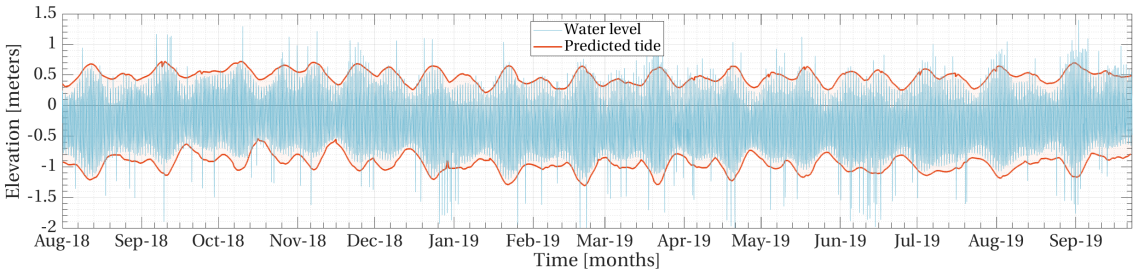

Figure 3.4: The tidal prediction and water level of Daytona Beach (station 8721120) from August 2018 to September 2019 in meters relative to NAVD88.

3.3. Topography and bathymetry

Prior to the nourishment activities (August 2018), the hydrographic and topographic beach were mapped by the Seaside Engineering & Surveying. The horizontal and vertical coordinates of the topographic survey were gathered using a Topcon GR3 Dual-Frequency GPS Receiver with Real-time Kinematic (RTK) corrections. The hydrographic survey was executed using both a single beam echo sounder (ODOMECHOTRAC CV100) and a multi-beam echo sounder (POS MV). The spatial resolution of the obtained survey data was approximately 5 meters in cross-shore direction and 300 meters in alongshore direction. The survey data was used to reconstruct the beach zone elevation, by interpolating on a rectangular 10 by 10 meter grid. Additionally, The bed level elevations were translated to meters relative to NAVD88. The total elevation map spans 5 kilometers in alongshore direction and 1 kilometer in cross-shore direction. The bathymetry displays parallel depth contour lines at the location of New Smyrna Beach (Figure 3.5). Near the Ponce de Leon Inlet, the contour lines deviate, indicating a more shallow area.

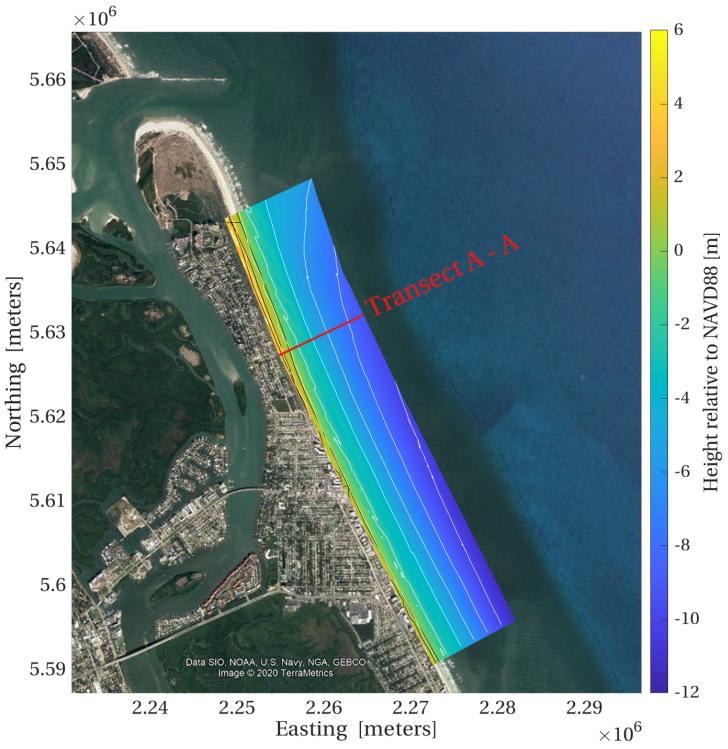

Figure 3.5: The beach zone elevation levels of New Smyrna Beach (August 2018) given in meters w.r.t. NAVD88. The coordinate system is EPSG: 2236 NAD83/Florida East [m].

Figure 3.6 is displaying the bed elevation of transect A – A. The locations of two sandbars can be deducted. The most offshore sandbar was positioned 200 meters from the coastline, and

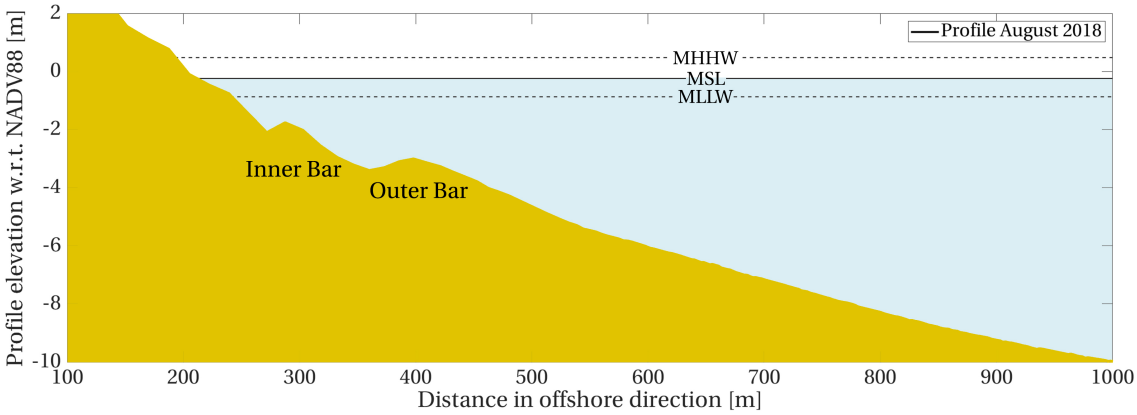

Figure 3.6: The bed elevation of cross-shore transect A-A (Figure 3.5). A two-bar system was found with an inner bar positioned 100 meters seaward and the outer bar 200 meters seaward of the coast.

the most shoreward sandbar approximately 100 meters. Additionally, the Mean Higher High Water level, the Mean Sea Level, and the Mean Lower Low Water level are illustrated. Both sandbar crests were lower than the MLLW, indicating that they were submerged at all times. Additionally, the bed elevation decreased from + 2.0 meters at the beach to −10 at the offshore edge of the image, leading to a nearshore slope of 1:75.

3.4. Nourishment information

In August 2018, Cavache Inc started the dredging of the Ponce de Leon Inlet. The obtained sediments were transported from the Inlet to the placement area via a pipeline sleeve. Figure 3.1 illustrates the dredging route and the planned placement template. However, due to unfavorable wave conditions and operational difficulties, the nourishment was placed more concentrated at an approximate depth of 4.25 meters with respect to mean sea level. Unfortunately, the exact sediment dumping spots are not known. Available data to this project was a time-series of deposited sediments per day.

The nourishing of the nearshore zone of New Smyrna Beach started in August 2018 and stopped in de final week of February 2019 (Figure 3.7). The daily deposited amount of sediments varied in time and had a maximum value of approximately 5000 m^3. In total, around 350,000 m^3 of sediments were placed (right axis).

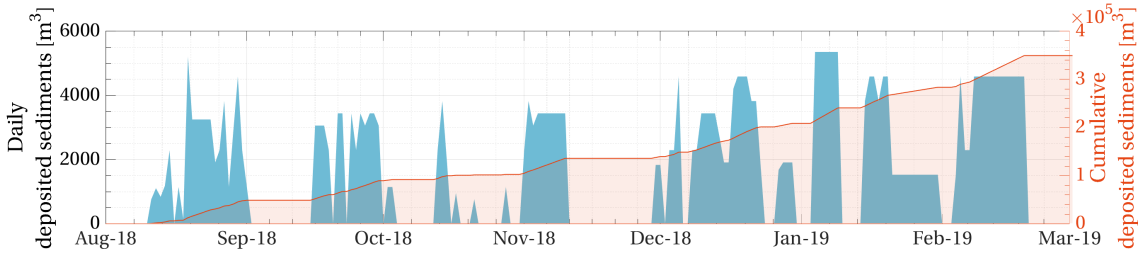

Figure 3.7: The daily deposited amount of sediment (left axis) and cumulative amount of deposited sediment (right axis) in m^3 in the nearshore zone of NSB between August 2018 and March 2019.

3.5. Site imagery collection

A mini Argus-system, consisting out of 4 cameras, was installed prior to the nourishment activities at a nearby high-rise hotel (Coronado tower, see Figure 3.1). The system monitored the New Smyrna Beach zone from August 2018 to September 2019. Each day from 07:00 am to 07:00 pm, the mini Argus-system collected imagery over a 10 minutes sampling period, with individual frames compiled at 2 Hz (Bruder et al., 2019a). The imagery products included Timex, Variance, Brightest, and Darkest imagery. This formed, together with a

snapshot at the start of each collection moment, the output of the mini Argus-system. To facilitate quantitative research, the imagery products were combined and georectified using the methodology of Holland et al. (1997), see Bruder et al. (2019a) for a more detailed description of the process. Figure 3.8 gives an example of the imagery before and after merging and georectifying.

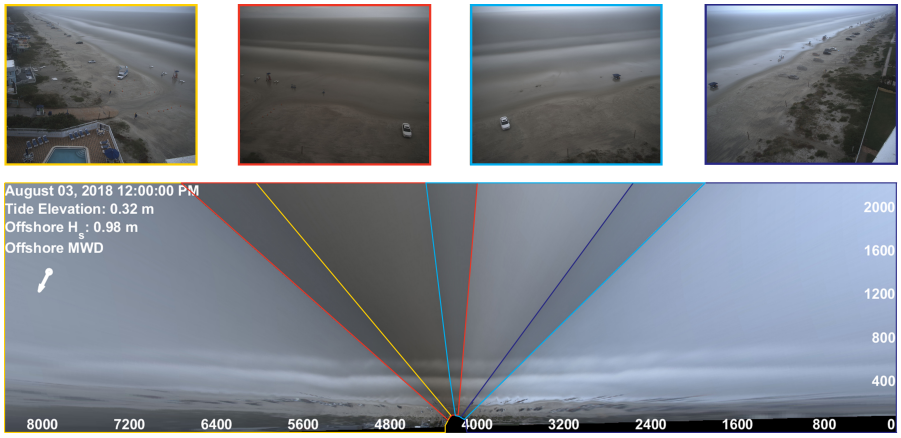

Figure 3.8: Top: oblique images obtained from the four cameras of the mini-Argus system at New Smyrna Beach, Florida, on August 3, 2018, 12:00. Bottom: the resulting merged image after is has been georeferenced and georectified (Bruder et al., 2019a). There is some overlap between the images to ensure accurate merging.

Image rectification forces pixels to resize to a pre-designed grid. As a consequence, the accuracy of a merged georectified images varies in both cross-shore and alongshore direction. The resolution of the New Smyrna Beach data was calculated using the StationDesign Toolbox from the CIRN (Koetje and Palmsten, 2020). Required input variables were the mini Argus-system extrinsic (position in world coordinates, height, orientation) and intrinsic parameters. The intrinsics were obtained before installation, and the extrinsics were obtained doing field measurements (Bruder et al., 2019a).

The cross-shore resolution of the mini Argus-system at New Smyrna Beach (Figure 3.9, left) had a maximum value of 0.8 meters per pixel. Lower accuracy levels were found for the alongshore direction (Figure 3.9, right), which had a maximum resolution value of 50 meters per pixel. To ensure a certain quality level, the merged georectified images were cut off at threshold resolution levels. In the alongshore direction, the threshold level was set at 30 meters per pixel. Theoretically, no limit should be necessary for the cross-shore direction. However, when the cameras see off into the horizon, the resolution becomes infinitely large. Therefore, the maximum cross-shore resolution was also set at 30 meters per pixel.

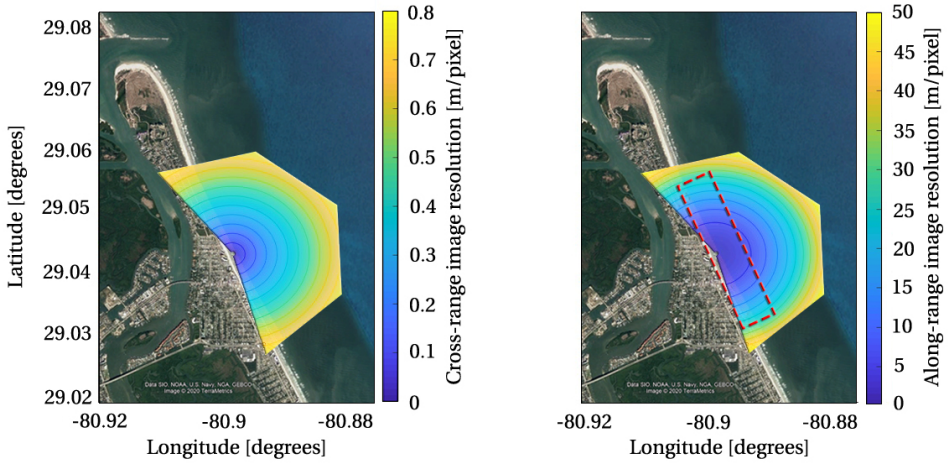

Figure 3.9: Cross-shore range resolution in meter/pixel of the Argus station located in NSB (left). B: Alongshore range resolution in meter/pixel of the Argus station located in NSB (right).

The available imagery data for describing the beach and nearshore berm nourishment include merged and georectified Snapshots, Timex, Variance images, Brightest, and (run-) Darkest images (Figure 3.10. In the next Chapter, the different imagery types were used to find the optimal approaches for the nearshore berm and shoreline position extractions.

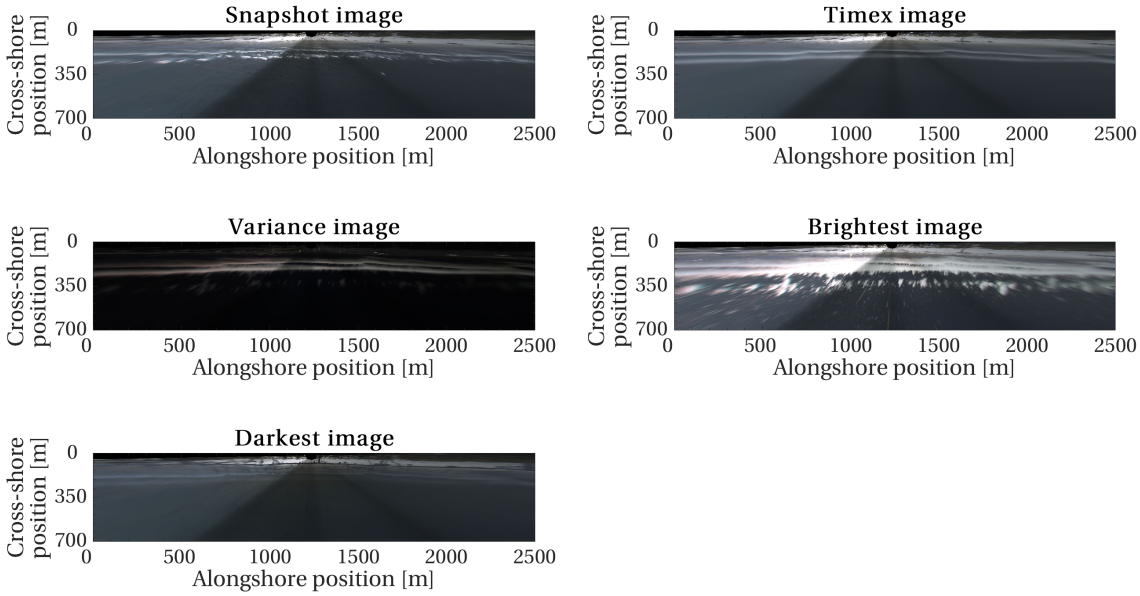

Figure 3.10: Available imagery data consists of merged georectified Snapshots, Timex, Variance, Brightest, and Darkest images (From top to bottom and left to right). The area covered by the imagery data is 2500 meters alongshore by 700 meters cross-shore.

4

Converting images to berm and shoreline positions

Together with the locations of sand deposition, the berm and shoreline positions can be used for describing the influence of the nourishment on the Beach of New Smyrna. This Chapter aims to find the best way to extract these position time-series and, therefore, answers the second sub-question, "How can the nearshore berm and the shoreline positions be optimally extracted from the New Smyrna Beach imagery data?". The optimal extraction methods for obtaining the positions of the sediment outflow, nearshore berm, and shoreline are discussed in sequence.

4.1. Introduction

Nourishment placement locations provide essential information for interpreting nearshore berm and shoreline migration patterns. However, the placement locations of the New Smyrna Beach nourishment had not been stored by the contractor. The sediments were deposited in the nearshore zone via a pipeline, which was visible in the Argus imagery data. The visibility made it possible to extract the placement locations.

After the placement, the sediments migrated freely under the influence of waves and currents. Whereas the sediment outflow positions were visible on the Argus imagery data, this was not the case for the nearshore berm nourishment. Because the nourishment was submerged nearly the entire time, it was challenging to find an accurate nourishment position extraction method. However, once the ratio depth to wave height on top of the nourishment crest became small enough, the crest positions could be followed by following the wave breaking locations. The produced foam was visible on the Argus imagery data and appeared as areas of high brightness intensity. In general, the locations of the nearshore berm crest, x_b, corresponds well with the location of maximum wave breaking, x_i (Lippmann and Holman, 1989). The deviation between x_b and x_i is in the order of 10 meters and caused by the shift in break point location relative to the bar crest. x_i shifts seaward when wave breaking becomes more intense until the wave climate is saturated and/or with altering water levels (Guedes et al., 2011).

However, the existence of the two sandbars in the nearshore zone of New Smyrna Beach (Figure 3.6) complicated this approach. In the wave braking patterns, it is difficult (if not impossible) to separate the nourishment and sandbars. Therefore, it is not possible to solitary extract the positions of the nearshore berm. In the remaining part of the thesis, the terminology "berm/bar positions" corresponds both to the sandbar and to the nearshore berm positions.

A fraction of the sediments was expected to reach the shoreline. To find out how much the shoreline was affected by the nourishment, shoreline position time-series were required. However, the extraction of the shoreline positions in time is difficult due to the changing appearance and the varying geomorphic and hydrodynamic environment. This resulted in a wide variety of shoreline detection models, each developed and validated on a different site (Plant et al., 2007). The four most used were tested on New Smyrna Beach to find the model that suits the site characteristics best and, therefore, leads to the most accurate shoreline positions.

4.2. Sediment outflow positions

This section aims to find the optimal approach for tracking the sediment outflow positions.

4.2.1. Applied method

The five georectified and merged Argus imagery types (Snapshot, Timex, Variance, Brightest, and Darkest) were compared to find the data type that visualized the pipeline best. The outflow locations on imagery types were compared qualitatively because, due to the specific image type characteristics, an image behavior explanation was thought to be more useful than metric comparisons. Finally, the positions were stored by manual determination of the pipeline locations on the optimal imagery type.

4.2.2. Imagery type selection

Figure 4.1 displays the outflow pipe on an aerial image, and subsequently, on the Argus imagery data. When visually comparing the images, it becomes clear that not all output types are optimally displaying the pipe outflow.

- **Snapshot image**: whereas the other imagery data types are the result of a 10-minute averaging, the Snapshot is the only type that was obtained instantly. Potentially, this can cause inaccurate positions if the pipeline was moved during data collection. In addition, possible noise (vessels, breaking waves, surfers) was not averaged out.
- **Timex image**: due to the averaging effect, the Timex is displaying the pipeline clearly. Little to no noise can be seen in the image.
- **Variance image**: because of the stable pipeline position within the 10-minute monitoring time frame, the Variance image is almost entirely black.
- **Brightest image**: the most white pixels were saved in the 10-minute time frame, which can result in a less distinct pipeline visualization. If wave breaking near the outflow position occurred, the Brightest image highlights the wave foam over the pipeline.
- **Darkest image**: opposite to the Brightest image, the Darkest image illustrates the darkest pixels within a 10-minute time frame and should highlight most of the black pipe. However, movements of the pipe can result in an inaccurate shape and, therefore, to a distorted location.

Concluding, the optimal imagery type for manual determination of the sediment outflow locations is the georectified and merged Timex. The averaging effect leads to a reduction of noise in the image and displays the mean pipeline location within the 10-minute sample period.

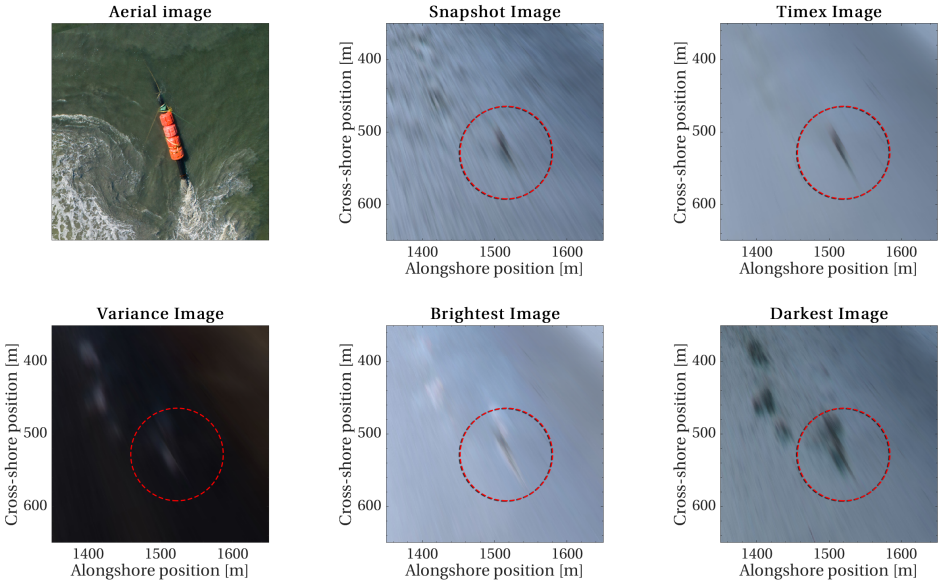

Figure 4.1: The sediment outflow position displayed on the Argus imagery data (Snapshot, Timex, Variance, Brightest, and Darkest image) and an Aerial photo (Retrieved June 12, 2020, from: https://www.surfline.com/surf-news/florida-pros-revel-man-made-sandy-slabs/47373).

4.2.3. Constructing time-series

Applied method

The sediment outflow positions were visible in the Argus imagery data. The visibility of the pipe outflow on georectified and merged Snapshots, Timex, Variance, Brightest, and Darkest imagery types were compared to find the type that resulted in the most accurate outflow positioning.

Imagery type selection

The optimal imagery type for extracting the sediment outflow locations was found to be the Timex. The 10-minute averaging effect canceled most noise and, compared to other imagery types, resulted in the cleanest image. Additionally, the pipeline location on the Timex imagery represents the average location, which removes inaccurate positions if the pipeline moved due to wave motions while sampling.

Input selection

It was assumed that throughout the day, the pipe outflow was not relocated. This led to the input data-set of 116 georectified merged Timex imagery, each taken at 01:00 p.m. starting in August 2018 en ending in March 2019. In 74 % of the time, it was possible to obtain the outflow position via manual determination.

Precision

An estimation of the precision of the manual determination approach was obtained by randomly selecting 10 images and, subsequently, determining the positions five times. The resulted outflow locations are illustrated in Figure 4.2. The points were color to the distance from the mean location. The precision of the manual determination approach was estimated at order 5 meters.

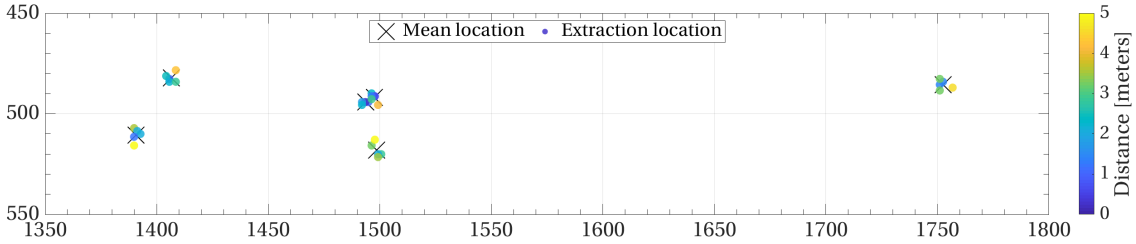

Figure 4.2: The precision of the manual determination approach of the sediment outflow positions.

Summarized

- Input: 116 georectified merged Timex imagery, each daily taken at 01:00 p.m.
- Extraction method: manual determination of the outflow position with an estimated precision of order 5 meters.
- Output: a time-series of 87 outflow locations in time, starting at August 2018 and ending in March 2019.

4.3. Nearshore berm/bar positions

This section aims to find the optimal approach for tracking of the nearshore berm/bar positions.

4.3.1. Applied method

The objective is to map the locations of the nearshore berm to link the migration patterns to the subsequent response of the shoreline. Nearshore berm locations are well related to locations of persistent wave breaking and, resultingly, to intensity peaks in the Argus imagery data (Guedes et al., 2011). The general extraction approach of the intensity peaks locations starts with transforming the imagery to grayscale and dividing it into cross-shore transects. At each transect, the peak locations are stored. Subsequently, the alongshore persistent wave breaking pattern is constructed by connecting the peak locations of each cross-shore transect. The Bar Line Intensity Mapper (BLIM) (Pape, 2008) is an accepted model that follows the described approach and was used in this research.

4.3.2. Imagery type selection

The mini Argus-system of New Smyrna Beach provided five imagery types: a Snapshot image, Timex, Variance image, Brightest image, and (run-) Darkest-image. However, literature is inconsistent about the optimal imagery type for the extraction of nearshore berm crest positions (Guedes et al., 2011). Therefore, the intensity profiles of the Timex, Variance, Brightest, and Darkest imagery types were analyzed and compared. The Snapshot imagery type was only used to analyze the initial conditions. Contrary to the Timex, Variance, Brightest, and Darkest imagery types, the position of maximum wave breaking on the Snapshot is instantaneous and does not necessarily match the location of persistent wave breaking. The aim is to find the data type that can be used for extraction during most weather conditions and results in the most accurate prediction of the position of the nearshore berm.

Two hydrodynamic conditions (Figure 4.3, 4.4) were used to test the image types:

1. Mild wave conditions: waves with a maximum height of 1.2 meters (August 6, 2018, 11:00 a.m.)
2. Energetic wave conditions: waves with a maximum height of 4.0 meters (January 28, 2019, 21:00 p.m).

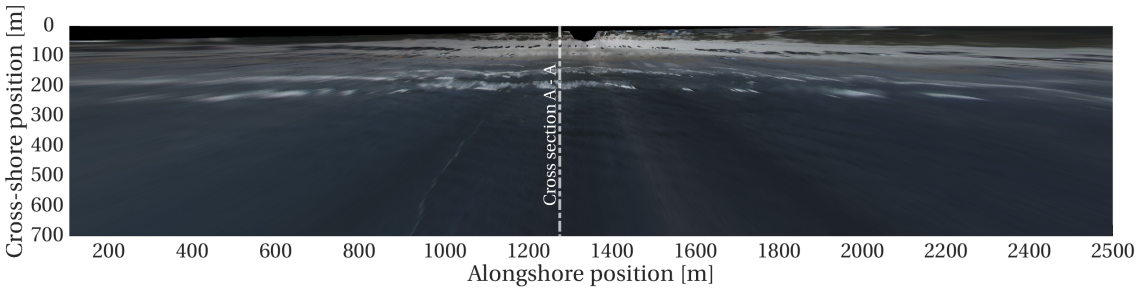

Figure 4.3: A Snapshot of NSB on August 6, 2018, 11:00 a.m. At this moment in time, the waves reached a maximum height of 1.2 meters.

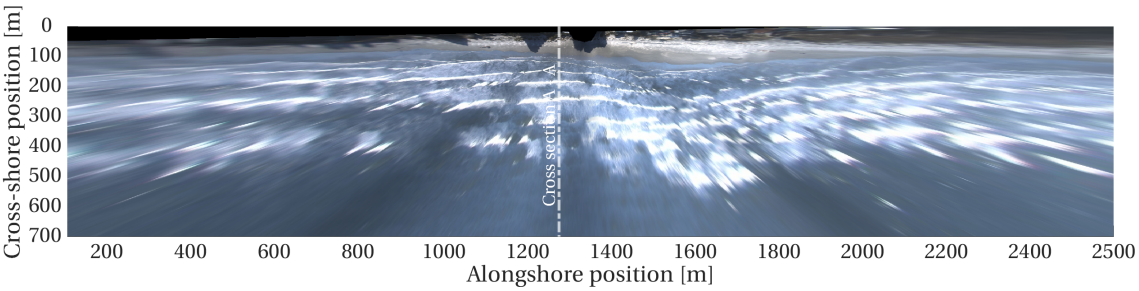

Figure 4.4: A Snapshot of NSB on September January 28, 2019, 21:00 p.m. At this moment in time, the waves reached a maximum height of 4.0 meters.

Mildly energetic waves (cross-shore)

The intensity profiles of the Timex, Variance, Brightest, and Darkest imagery types are first discussed using cross-section A-A (alongshore location y = 1325, see Figure 4.3). Figure 4.5 illustrates the intensity profiles for the imagery data types, and, subsequently, the found peak locations on to the corresponding Snapshot. To remove peak locations corresponding to small fluctuations in the intensity profile, it was assumed that locations of persistent wave breaking had a minimum width of 5 meters. The peak definitions and positioning of the intensity profiles were compared to find the most accurate and consistent imagery type for mildly energetic conditions.

- Starting at cross-shore location x = 700 and moving towards the shore, a low and stable intensity value is found for all four intensity profiles. This was caused by the dark watercolor and the absence of wave breaking.
- Near x = 220, the first waves started to break, which resulted in a first intensity peak for all imagery types. The intensity profile of the Darkest imagery type has the most shoreward peak location, and the Brightest imagery type the most seaward. The more dark color of a wavefront before breaking can

explain the more shoreward peak location of the Darkest imagery type compared to the Timex. Furthermore, the peak location of the Brightest imagery is most seaward due to the storing of white pixels caused by the first wave breaking. The difference between the two is approximately 20 meters.

- At cross-shore location x = 150 meters, the remaining waves break at the shoreline. The difference in intensity peak locations of the Timex, Variance, and Brightest is between 5 to 10 meters. The intensity profile of the Darkest imagery type peaked approximately 30 meters more shoreward at the darker colored wet sand.
- The remaining part of the intensity graph has more fluctuating intensity magnitudes, which is caused by different features on the shore. Examples are the color difference between wet and dry sand, water pools, people, cars, and parasols. The Variance filters out most of the non-changing features and, therefore, results in the least fluctuating intensity profile.
- Overall, clear peak definitions are found for the Timex, Variance, and to a lesser extent, the Brightest imagery type. The Darkest imagery resulted in an intensity profile without any significant peaks at sea. Within the 10-minute sampling frame, the Darkest imagery type stores the more dark pixels, corresponding to non-breaking waves, over the more white pixels of breaking waves. Eventually, this led to a profile with nearly no peaks at the seaward side of the shoreline.

Summarizing, both the Timex, Variance, and Brightest intensity profiles gave similar peak locations (order of 10 meters). On the contrary, the Darkest intensity profile had less distinct peak definitions, and the resulting peak locations did not necessarily correspond to wave breaking locations. Therefore, during a mild wave climate, the Darkest imagery type is not optimal for extracting wave breaking locations.

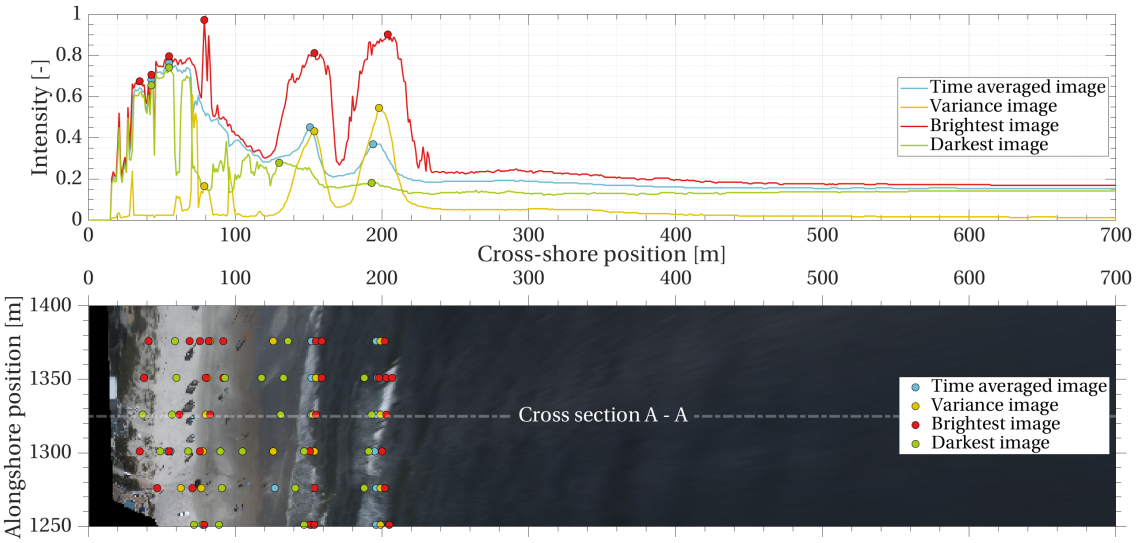

Figure 4.5: Top: the intensity profiles and peak locations (solid circles) of the Timex, Variance, Brightest and Darkest imagery types on August 6, 2018, 11:00 a.m. at cross-section A-A. Bottom: the resulting peak locations of the intensity profiles illustrated at the corresponding Snapshot. The maximum significant wave height was 1.2 meters.

Mildly energetic waves (alongshore)

The spatial consistency of the output locations for the Timex, Variance, and Brightest imagery were checked by focusing on the total monitored area (Figures 4.6a, 4.6b, and 4.6c). The Darkest imagery type was not considered because the results on Cross-Section A-A were not satisfying. The Timex, Brightest, and Variance resulted in three alongshore bands of peak locations. Most likely, there were caused by wave breaking on the inner sandbar, coastline, and scatter at the beach. It stands out that, compared to the Timex and Brightest, the Variance imagery resulted in fewer peak locations at the beach.

To compare the alongshore consistency, all peak locations were plotted on to the corresponding Snapshot (Figure 4.6d). It can be concluded that the resulting peak locations at sea are approximately similar for the Timex, Variance, and Brightest imagery during mild wave conditions, and match the wave breaking locations in the Snapshot.

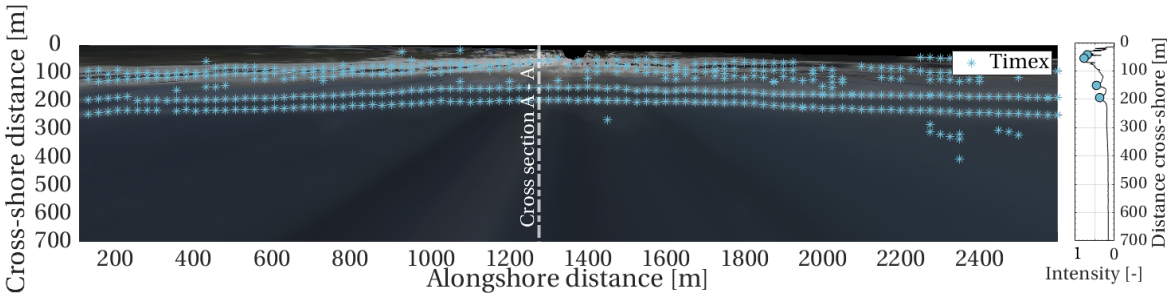

(a) The Timex imagery of NSB during mild conditions (August 6, 2018, 11:00 a.m., H_s = 1.2m) and the corresponding intensity peak locations. The intensity profile of cross-section A-A is displayed on the right.

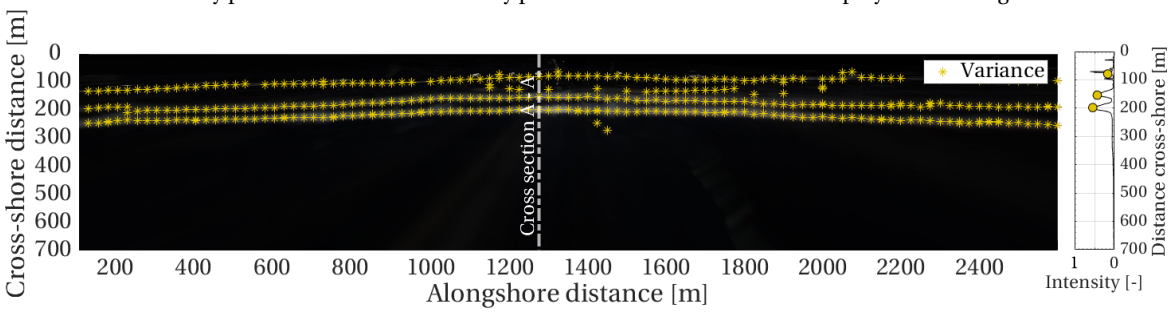

(b) The Variance imagery of NSB during mild conditions (August 6, 2018, 11:00 a.m., H_s = 1.2m) and the corresponding intensity peak locations. The intensity profile of cross-section A-A is displayed on the right.

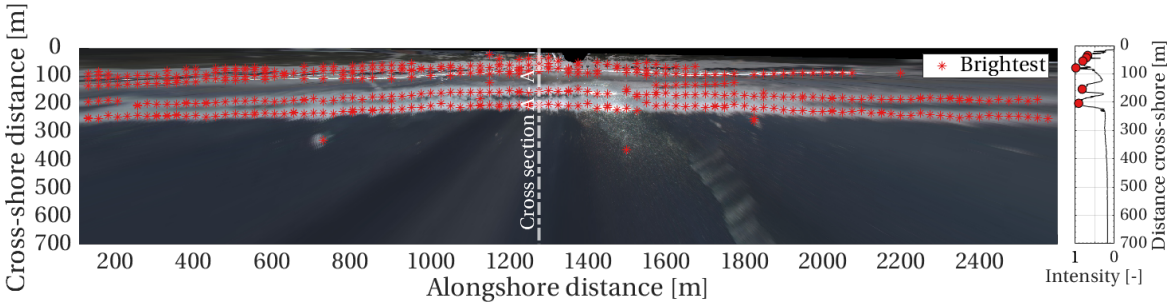

(c) The Brightest imagery of NSB during mild conditions (August 6, 2018, 11:00 a.m., H_s = 1.2m) and the corresponding intensity peak locations. The intensity profile of cross-section A-A is displayed on the right.

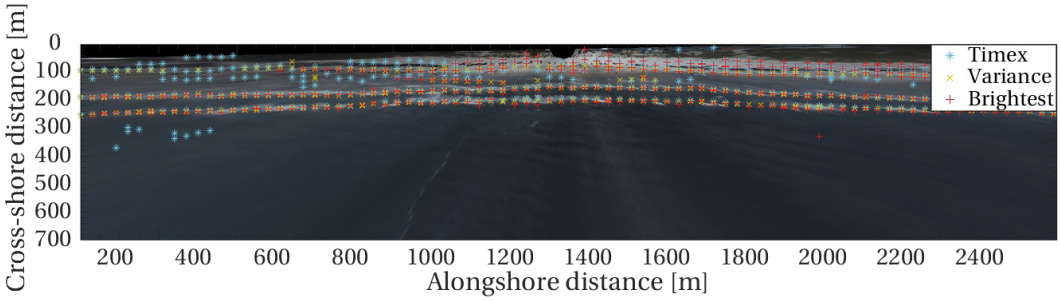

(d) The Snapshot imagery of NSB during mild conditions (August 6, 2018, 11:00 a.m., H_s = 1.2m) and the intensity peak locations found for the Timex, Variance, and Brightest imagery types.

Figure 4.6: A comparison of the intensity peak locations found using the Timex, Variance, and Brightest Imagery during mildly energetic conditions. First, the output is displayed on the corresponding imagery types to validate the obtained peak locations visually. Afterward, all output is illustrated together on the Snapshot to compare the positioning of the peak locations and the wave breaking locations.

Energetic wave conditions (cross-shore)
The intensity profiles of the Timex, Variance, Brightest, and Darkest imagery types are discussed using cross-section A-A (alongshore location y = 1325, see Figure 4.7). The peak locations found using the four imagery types are displayed in Figure 4.7. The peak locations were found using a minimum peak width of 5.0 meters to focus on locations of persistent wave breaking instead of occasional wave breaking.

- At cross-shore location x = 700, the obtained intensity values are already higher than the values obtained during mildly energetic conditions. This is caused by wave breaking throughout the whole nearshore zone.
- For the Brightest imagery, the first intensity peak occurred at x = 550. From this point onward, the Brightest intensity profile has a value of approximately 1.0, which can be explained by the intense wave breaking. For the Variance, the first peak location is near x = 460. Twenty meters more shoreward, the first peak of the Timex is found. The Darkest imagery results in a peak at x = 390. The significant difference between the Timex, Variance, and Darkest peak locations is caused by the fact that wave breaking near x = 450 was, apparently, not continuous. The Darkest imagery type stored the more dark pixels of the non-breaking waves over the more pixels white of the wave breaking induced foam. Eventually, this led to an intensity profile without a significant peak near x = 450 for the Darkest imagery type.
- Between the start of wave breaking and the shoreline at x = 100, multiple intensity peaks are visible. The Timex intensity profile has two distinct peaks; the first occurred at x = 320 and the second at 250. The peaks of the Darkest intensity profile are located approximately at the same location, indicating the occurrence of continuous wave breaking. The Variance intensity profile behaves opposite to the Timex and Darkest profiles and peaked at x = 270, 220, and 200.
- From x = 50 to x = 0, all intensity profiles fluctuate significantly due to the change in color of the sediment, dunes, bushes, and other features.
- Overall, the intensity profiles of both the Timex and the Variance have clear peak definitions. The Darkest intensity profile displays significant local fluctuations, and the Brightest intensity profile has no peaks at most of the cross-shore transect.

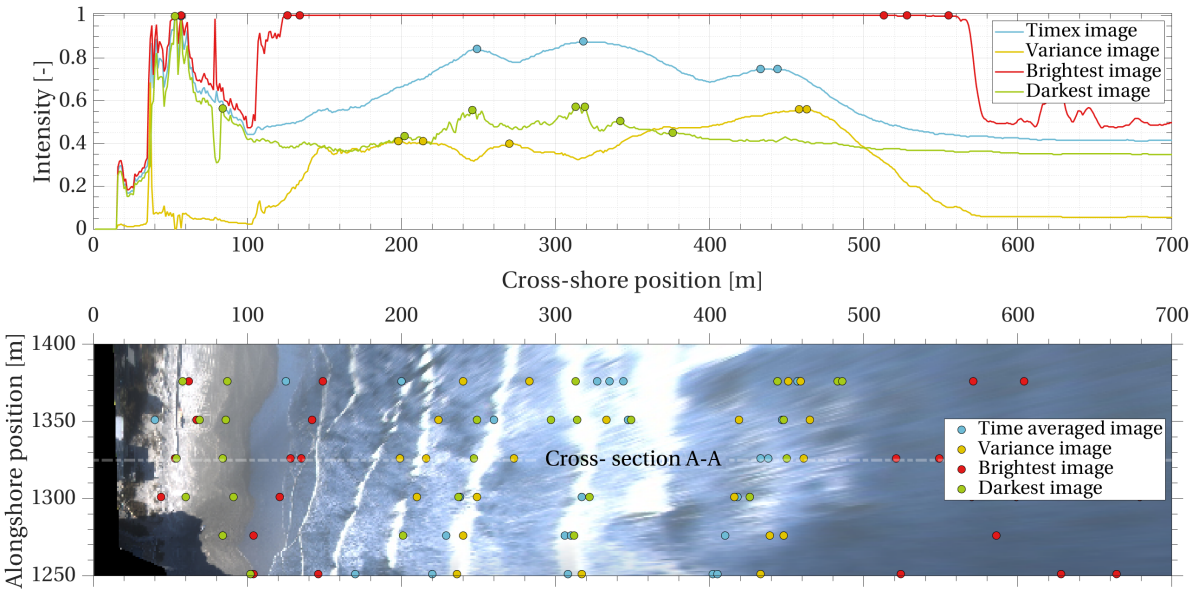

Figure 4.7: Top: the intensity profiles and peak locations (solid circles) of the Timex, Variance, Brightest and Darkest imagery type on January 28, 2019, 21:00 p.m at cross-section A-A. Bottom: the resulting peak locations of the intensity profiles illustrated at the corresponding Snapshot. The maximum significant wave height was 4.0 meters.

Summarizing, it was found that the intensity profiles of the Timex, Variance, Brightest, and Darkest did not lead to similar results. The Brightest intensity profile had a value of 1.0 for most of the cross-section, which cancels the possibility of identifying local maxima. Additionally, the Timex and the Darkest imagery types had similar peak locations near x = 250 and 320. Focussing on the peak definitions, it can be concluded that

the Timex and Variance intensity profiles were well defined. On the contrary, the Darkest intensity profile had significant local fluctuations. Although the peak locations of the Timex and Variance intensity profiles did not correspond, they did meet the peak definition demands. Therefore, the alongshore consistency was tested for both the Timex and the Variance imagery type.

Energetic wave conditions (alongshore)
The spatial consistency of the output locations for the Timex and Variance imagery were checked by considering the total monitored area (Figure 4.8a and 4.8b). The Brightest and Darkest imagery types were not considered because the results found at cross-section A-A did not meet the set peak definition demands.

Both the Timex and the Variance imagery resulted in 3 alongshore bands of peak locations and some scatter near the beach. The alongshore bands of both the Timex and Variance imagery display discontinuities between alongshore location y = 1300 and 1700, which is the approximate location of the nourishment. The altering bathymetry leads to deviations from the alongshore wave breaking bands. Furthermore, the peak locations of both intensity profiles visually correspond with their imagery types.

The peak locations of the Timex and Variance imagery are both illustrated with the corresponding Snapshot to analyze if the locations of persistent wave breaking match the initial conditions (Figure 4.8c). It becomes clear that the Timex peak locations correspond better to the wave breaking locations than the Variance peak locations. Although both followed a similar pattern, the intensity peak locations of the Variance image are located more offshore.

The locations of persistent wave breaking and underlying (sandbar) bathymetry differ with alternating wave conditions (van Enckevort and Ruessink, 2001). Although the results of the Timex imagery corresponds better to the locations of wave breaking, it does not necessarily mean that it better matches to the berm/bar crest locations. Guedes et al. (2011) analyzed the deviations between the locations of intensity peaks of the Timex (δx_{til}) and Variance imagery (δx_{val}) in relation to and the bar crest locations. For wave heights between 0 – 3 meters, δx_{til} deviates between 10 meters seaward and shoreward of the crest locations. Additionally, δx_{val} is approximated in the range of 0 and – 20 meters. Therefore, especially for more energetic wave conditions, the Timex imagery is more suitable for extracting the locations of the berm/bar crest.

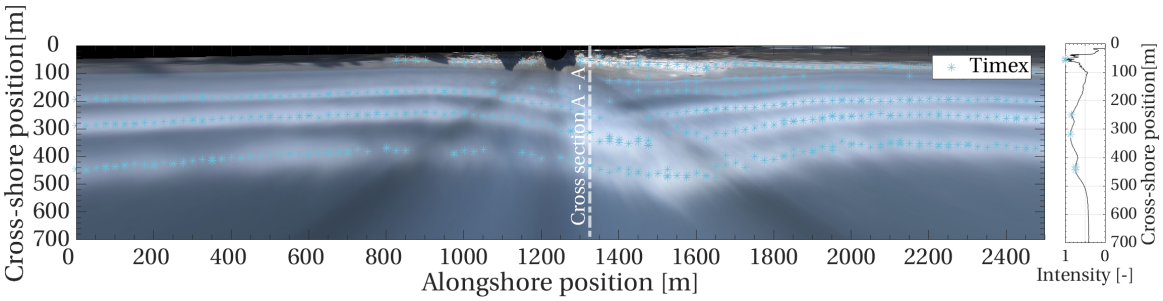

(a) The Timex imagery of NSB during energetic conditions (January 28, 2019, 21:00 p.m., H_s = 4.0 m) and the corresponding intensity peak locations. The intensity profile of cross-section A-A is displayed on the right.

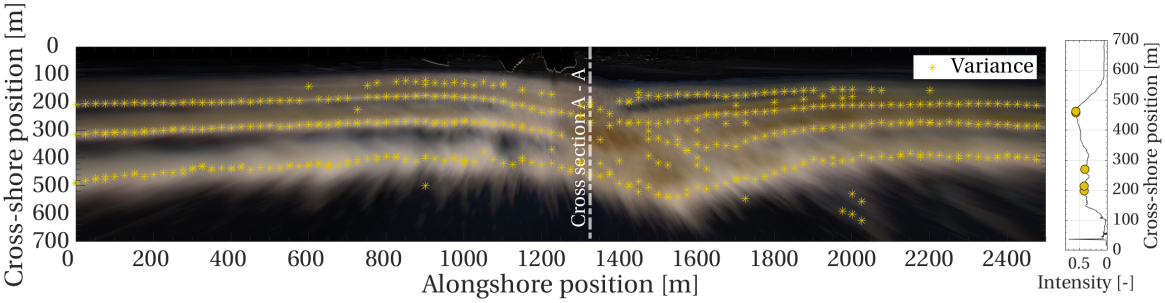

(b) The Variance imagery of NSB during energetic conditions (January 28, 2019, 21:00 p.m., H_s = 4.0 m) and the corresponding intensity peak locations. The intensity profile of cross-section A-A is displayed on the right.

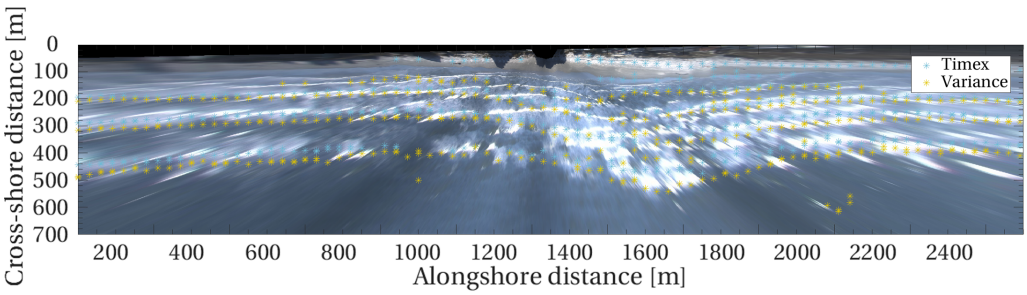

(c) The Snapshot imagery of NSB during energetic conditions (January 28, 2019, 21:00 p.m., H_s = 4.0m) and the intensity peak locations found for the Timex and Variance imagery types.

Figure 4.8: A comparison of the intensity peak locations found using the Timex and Variance Imagery during energetic conditions. First, the output is displayed on the corresponding imagery types to validate the obtained peak locations visually. Afterward, all output is illustrated together on the Snapshot to compare the positioning of the peak locations and the wave breaking locations.

4.3.3. Constructing time-series

The objective is to find the optimal approach for converting imagery data to nearshore berm/bar position time-series.

Applied method

The BLIM model was found to be an accurate model to extract the nearshore berm/bar positions from the Argus imagery data. The model assumes that the locations of wave breaking correspond with the locations of the nearshore berm/bar crest.

Imagery type selection

The Timex, Variance, Brightest, and Darkest imagery types were tested to find the type that resulted in the most consistent nearshore berm positions during alternating wave conditions. The Timex imagery was found to be the only imagery type delivered accurate berm/bar positions during mildly energetic and energetic wave conditions.

Input selection

Locations of persistent wave breaking correspond to nearshore berm/bar crest positions. However, with alternating wave heights and water levels, the locations of wave breaking shift relative to the berm/bar crest. Therefore, the Timex imagery data-set had to be filtered to obtain positions with the same correspondence to the bathymetry. Only imagery corresponding to a wave height of $0.5 \leq H_s \leq 2.5$, and a water level between $-0.50 \leq MLW \leq +0.50$ was used. Ideally, the filter restrictions would have been more limited, but this would influence the temporal density of the time-series. Additionally, some Timex imagery was manually rejected due to insufficient image quality. This, for example, happened during fog or sun-glare on the water surface. Eventually, this led to a time-series of 359 berm/bar positions in the alongshore, which is, on average, once a day.

Summarized

- Input: georectified merged Timex intensity imagery.
- Extraction method: extraction of berm/bar crest positions via the BLIM model.
- Output: a time-series of 359 sandbar crest locations in the period August 2019 to September 2019.

4.4. Shoreline positions

This section aims to find the optimal approach for tracking the shoreline positions. First, an overview is given of the used methods in the literature. Second, these methods and a visual determination approach are tested on the New Smyrna Beach site locations. Finally, the best method is selected and used for shoreline extraction.

4.4.1. Descriptions methods used in literature

An accurate procedure to extract shorelines from the imagery data was key to this research. Contrary to the extraction of berm/bar positions, multiple models could be applied. The visual shoreline appearance changes with alternating geomorphics, hydrodynamics, and weather conditions. This led to the development of multiple shoreline identification models, each developed and validated for different site locations. The four most used are the Shore Line Intensity Maximum (SLIM) model, the Pixel Intensity Clustering (PIC) model, the Color Channel Divergence (CCD) model, and the Artificial Neural Network (ANN) model (Plant et al., 2007).

- The SLIM model follows the same approach as the BLIM model. Both models aim to find alongshore intensity patterns in grayscaled pixels. In contrast to BLIM, the SLIM model focuses on the swash zone. High-intensity alongshore bands are produced by wave breaking and swash motions. The SLIM model assumes that the location of maximum intensity corresponds with the shoreline. According to Plant and Holman (1997), SLIM delivers accurate results in the order of 1-meter for reflective beaches with well-defined swash zones. However, the applicability of SLIM on more dissipative coastlines was questioned (Aarninkhof (2003), Plant et al. (2007), Turner et al. (2000)).
- The Pixel Intensity Clustering model was developed to overcome the failing SLIM model on more dissipative beaches. It defines the shoreline using the color difference between dry and wet sand. Additionally, to make the model also suitable for reflective beaches, a second discrimination function, similar to the SLIM model, was added. If the model fails to detect a shoreline based on the color difference, it generates the shoreline based on grayscale intensities. Therefore, the model should deliver accurate positioning on both reflective and dissipative beaches (1 - 6 meters, (Aarninkhof, 2003)).
- In line with the PIC model, the Color Channel Divergence model uses color difference to determine the shoreline positions (Turner et al., 2000). In contrast to the PIC model, the CCD model relies upon the expectation that more blue tones are found in water-pixels, and more red tones are found in beach pixels. A shoreline point is defined if the intensity profile, found by extracting the red channel from the blue channel, crosses a certain threshold level. The model was developed and validated on a dissipative coastline. The accuracy should be in the order of 10 meters (Turner and Adamantidis, 2001).
- The Artificial Neural Network identifies the shoreline via pixel characteristics and can be used on reflective and dissipative shorelines. Beforehand, the network must be tuned by manually determining shoreline positions on an image training set(Smit et al., 2007). The model saves the characteristics of dry and wet pixels and, subsequently, applies it to identify shorelines on new images. The accuracy of the model depends on the diversity of the training set and the manual tuning quality.

Table 4.1: Data return percentages of the SLIM, ANN, PIC, and CCD models tested on four different sites. Adapted from: Plant et al. (2007).

		Detection Model			
Site	Images	SLIM %	ANN %	PIC %	CCD %
Duck	43	50	92	78	76
Teignmouth	42	24	57	61	0
Egmond	44	15	32	24	17
Gold Coast	28	37	76	73	91

Plant et al. (2007) analyzed the four extraction algorithms using Timex imagery as input. The performance was tested at four different sites, exhibiting a range of morphological and hydrodynamic conditions. Although the output was well correlated, the cross-shore positions of the shoreline varied between the different approaches. Depending on the site and detection models, the difference was between 0 and 23 meters.

Additionally, it was found that all extraction algorithms were sensitive to change of the incident hydrodynamic conditions. The SLIM model was found to be the most unstable, while the ANN and the PIC model were most reliable (Table 4.1). At the time of writing, the ANN model was not available for this study.

4.4.2. Method selection

The SLIM model, CCD model, PIC model, and a manual extraction approach were tested to find the optimal extraction method for the New Smyrna Beach site.

SLIM model

The SLIM model was developed and validated the shoreline of Duck, North Carolina, which has a relatively steep beach slope and narrow, well-defined swash zone. Typically, the SLIM model was found to provide accurate shorelines if the coast is classified as reflective (Plant et al., 2007). In general, a reflective shoreline is characterized by a narrow surfzone without bars and a nearshore slope around 0.15.

From August 2018 to September 2019, New Smyrna Beach had two distinctive wave height seasons. In the summer months (June till August), the wave height was between 0.5 and 1.0 meters. During the remaining months (September till May), more energetic conditions resulted in wave heights up to 8.0 meters and a surfzone of a couple of hundred meters. The different surfzone widths are illustrated in Figure 4.9. In addition, the nearshore slope in August 2018 was calculated at ≈ 0.01, which is relatively flat.

Based on previous findings (Aarninkhof (2003), Plant et al. (2007)), it was concluded that the SLIM model only performs well on reflective beaches with well defines swash zones. During most of the year, New Smyrna Beach has an energetic wave climate. In combination with the relative flat nearshore slope, the shoreline has more a dissipative than reflective character. Resultingly, the location of wave breaking cannot be used as an accurate proxy for the shoreline, which is the primary assumption of the SLIM model. Therefore, the SLIM model was not taken into consideration as a shoreline extraction tool for New Smyrna Beach.

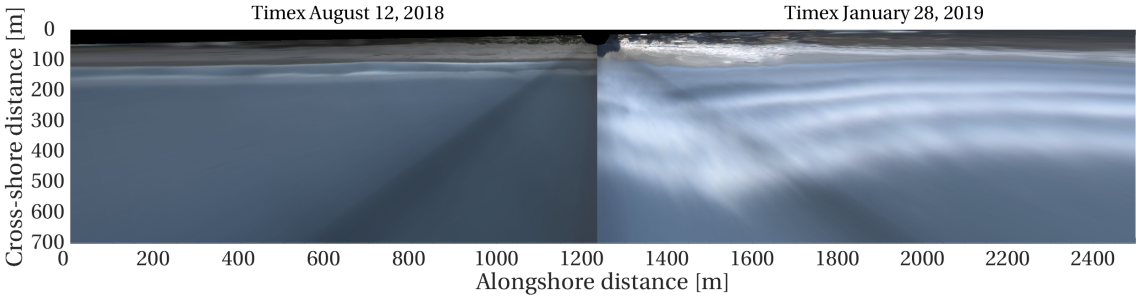

Figure 4.9: Left: the New Smyrna Beach during mild wave conditions (H_s = 0.5 meters). Right: the New Smyrna Beach during energetic wave conditions (H_s = 4.0 meters).

CCD model

The CCD model was developed to overcome the failing SLIM model on more dissipative coastlines (Plant et al., 2007). The model uses the intensity profiles of the blue-red color channels to extract possible shoreline locations. Focusing on a certain cross-shore transect and starting at the beach moving offshore, the RGB values are approximately equal at the white sandy beach. While crossing the wet sediments near the shoreline, the RGB values drop due to the more dark color of the sand. Moving further in the offshore direction, water pixels are causing the RGB channels to deviate from each other. A shoreline point is defined if the intensity of the blue minus red profile crosses a certain threshold level. After finding all possible shoreline points at each cross-section of the image, the final output consists of the longest continuous line of shoreline points. The threshold divergence value of 20 used in this study is similar to the value incorporated in the Coastsnap algorithm and was validated on the beaches of Southeast Australia (Harley et al., 2019).

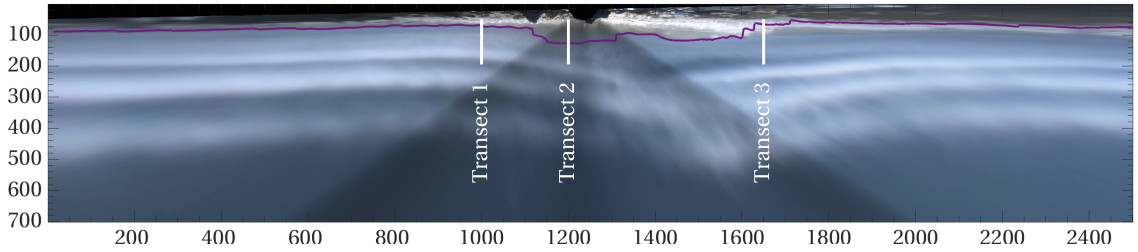

Figure 4.10: A Timex of New Smyrna Beach on January 28, 2019 during energetic wave conditions (H_s = 4.0 meters). The purple line illustrates the generated shoreline of the CCD model.

The Timex of January 28, 2018, was used to test the model capabilities. The corresponding significant wave height was 4.0 meters, and the coast could be classified as dissipative. The shoreline obtained using the CCD model was found to be inconsistent (purple line, Figure 4.10). In some parts, the model resulted in accurate shoreline positions, but in others, a clear difference between the visually estimated shoreline and the calculated shoreline could be seen. The results at three transects were described and compared to a visually picked shoreline. Besides, the CCD threshold level used to obtain the generated shoreline position is compared to the threshold level required to find the visually picked shoreline.

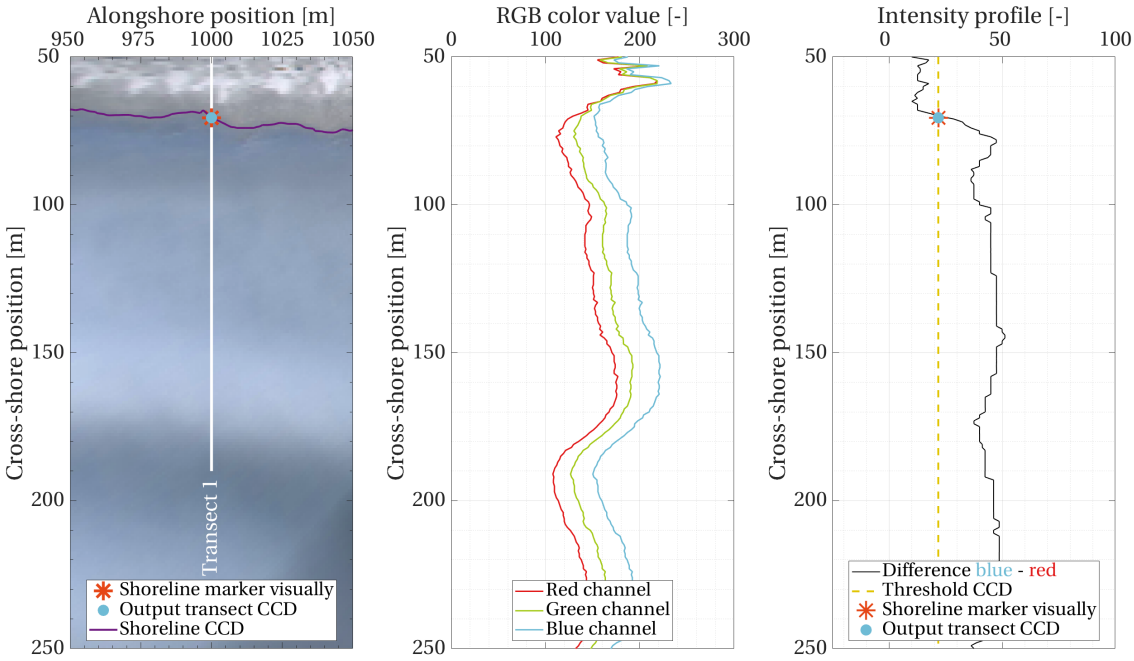

Figure 4.11: Left: the CCD generated shoreline (purple) and output at transect 1 (blue). A visual shoreline marker (orange) is displayed for comparison. Middle: the RGB color values at transect 1. Right: the intensity profile of the blue-red channels at transect 1.

- At the first transect (y = 1000), the obtained shoreline seems to align with the original shoreline. The CCD model generated one possible shoreline location (Figure 4.11, left), which matches the visually picked shoreline point. The RGB intensity profiles have approximately equal values at the beach and deviate when crossing the shoreline (Figure 4.11, middle). Because the CCD generated shoreline point equals the visually picked shoreline point, the optimal threshold level for this transect is similar to the used threshold level of 20 (Figure 4.11, right).
- The obtained shoreline point of the CCD model at the second transect (y = 1200) mismatches the visually picked shoreline. In line with the first transect, only one possible shoreline point was generated (Figure 4.12. left). The RGB intensity profiles have similar values at the shore and deviate when crossing water pixels (Figure 4.12, middle). However, the used threshold levels caused an inaccurate position of the shoreline point (Figure 4.12, right). To generate accurate output, the threshold level for this transect should be near 5.
- The shoreline at the third transect (y = 1650) mismatches the visually picked shoreline point. Contrary to the first two transects, multiple possible shoreline points were calculated by the CCD model (Figure 4.13, left). This can be explained by the lack of divergence of the RGB intensity profiles at the shore (Figure 4.13, middle). The used threshold level crosses the resulting blue-red intensity profile multiple times (Figure 4.13, right). Visually, the optimal threshold level for this transect would be near 50.

Summarizing, the CCD model is not capable of providing robust and accurate shoreline estimates.The model output was inconsistent and did not represent the visually marked shoreline accurately. Because of the changing image characteristics, an adaptation of the fixed threshold level will not necessarily lead to improved results. The merging process resulted in different brightnesses within the image. Additionally, in time, the image characteristics changed due to the weather conditions. In conclusion, the CCD model was not used further in this research.

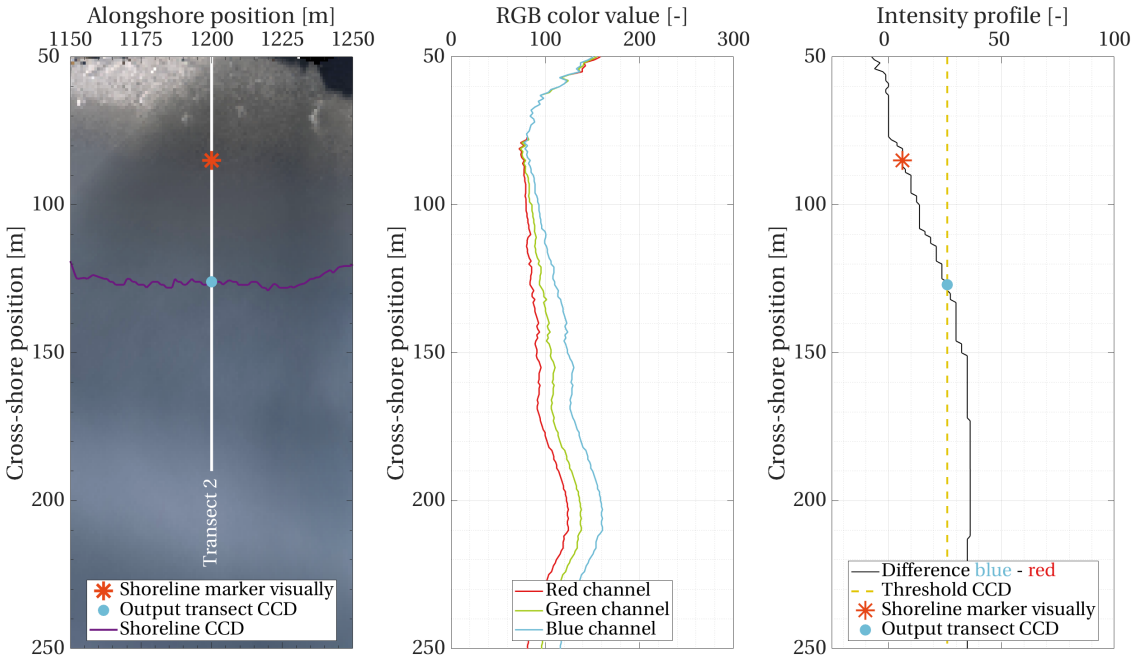

Figure 4.12: Left: the CCD generated shoreline (purple) and output at transect 2 (blue). A visual shoreline marker (orange) is displayed for comparison. Middle: the RGB color values at transect 2. Right: the intensity profile of the blue-red channels at transect 2.

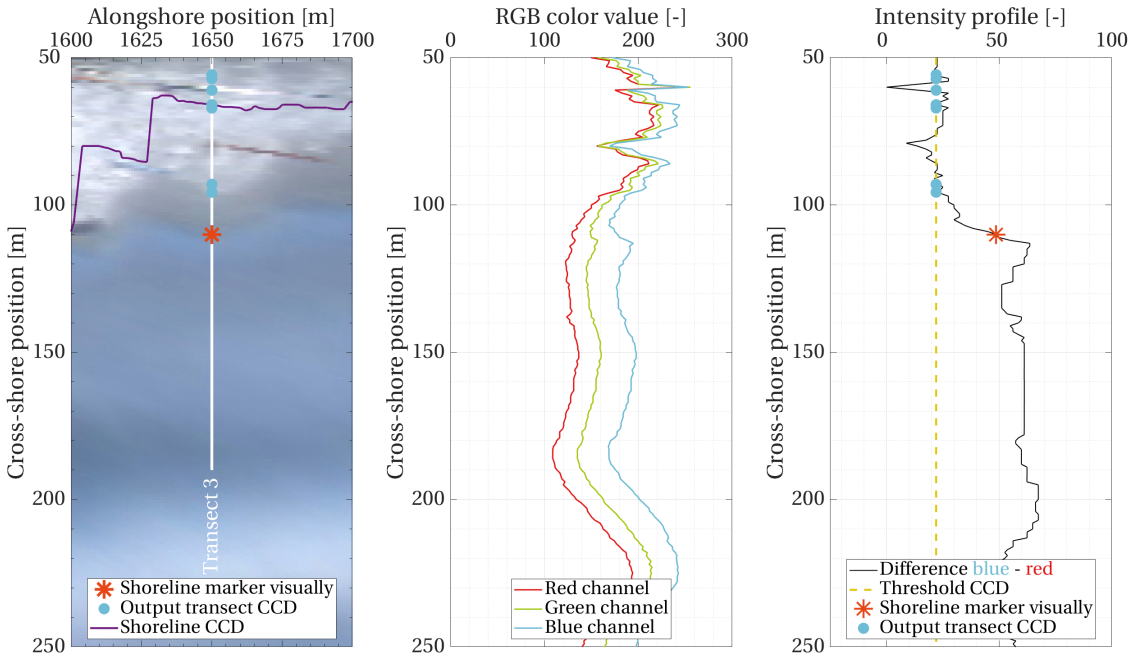

Figure 4.13: Left: the CCD generated shoreline (purple) and output at transect 3 (blue). A visual shoreline marker (orange) is displayed for comparison. Middle: the RGB color values at transect 3. Right: the intensity profile of the blue-red channels at transect 3.

PIC model

In line with the CCD model, the PIC model was developed to overcome the failing SLIM model on more dissipative coastlines (Plant et al., 2007). The shoreline is identified by the color difference between wet and dry sediments. Two discrimination functions are implemented to increase redundancy. The first differentiates dry and wet sediment pixels using the Hue and Saturation channels of the image, the second using the grayscale intensity profiles. Depending on the weather conditions, the shoreline may be identified better using the grayscale information instead of the Hue and Saturation. Contrary to the SLIM and CCD models, oblique Timex imagery is used as input.

In general, the PIC model converts the input image to Hue, Saturation, and intensity values and grayscale intensity values. Subsequently, two histograms are constructed. The first is based on the Hue and Saturation intensities, the second on the grayscale intensities. Because each image consists out of two main components (water and sand), two distinct clusters arise in the histograms. Finally, a discriminator function assigns negative values to wet pixels and positive to sand pixels. The shoreline is the line dividing the two components.

Figure 4.14: The oblique Timex of January 28, 2019, used a input for the PIC model and the defined region of interest.

To test the PIC model, an oblique Timex of January 28, 2019, was chosen. The image was taken by the second camera (Figure 3.8, red). The wave height reached up to 4.0 meters, and the shoreline could be classified as dissipative. The focus on the area near the shoreline, a Region of Interest (ROI) was defined (Figure 4.14). The two generated histograms, the first based on the grayscale intensities, the second on the Timex on the Hue and Saturation of the image, display altering results (Figure 4.15). Two distinct clusters were found in the Grayscale discrimination histogram and only one in the Hue and Saturation. The discriminator function is displayed in blue.

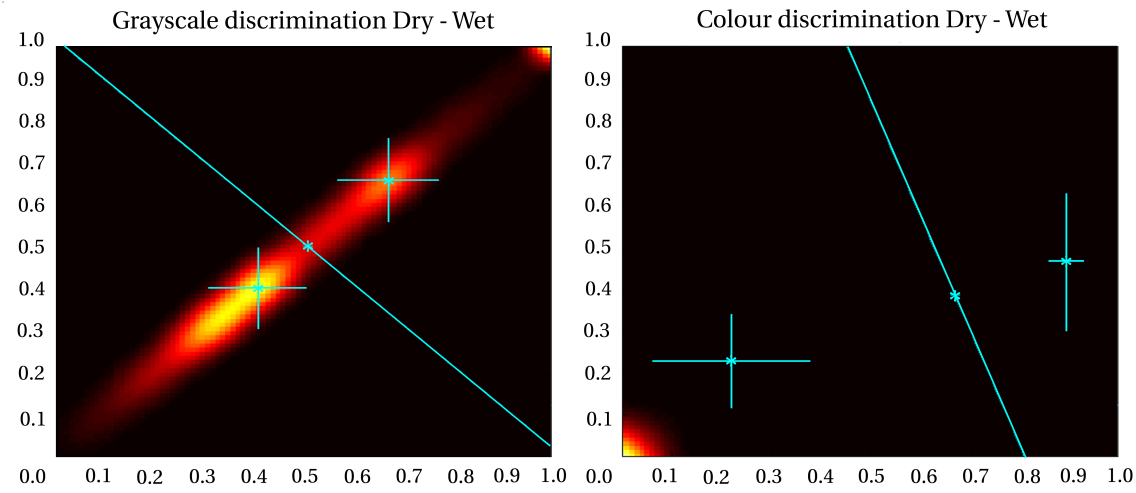

Figure 4.15: Left: histogram and discriminator function based on the grayscale intensities. Right: histogram and discriminator function based on Hue and Saturation.

Two shorelines were generated by the PIC model (Figure 4.16). The shoreline corresponding to the discrimination based on grayscale intensities is displayed left, the shoreline based on Hue and Saturation differences at the right. Although both partly follow the visual shoreline, distinct deviations can be seen. The grayscale based shoreline tends to be positioned more seaward and the Hue and Saturation based more landwards.

Summarizing, the PIC model was not capable of providing robust and accurate shoreline estimates. Although the model has two discrimination functions to increase accuracy during altering weather conditions, the results were not satisfying. Therefore, the PIC model was not used further in this research. It must be mentioned that the available PIC model for this research was not optimized for the New Smyrna Beach shoreline. Optimizing would potentially lead to more accurate results, but was not in the scope of the thesis.

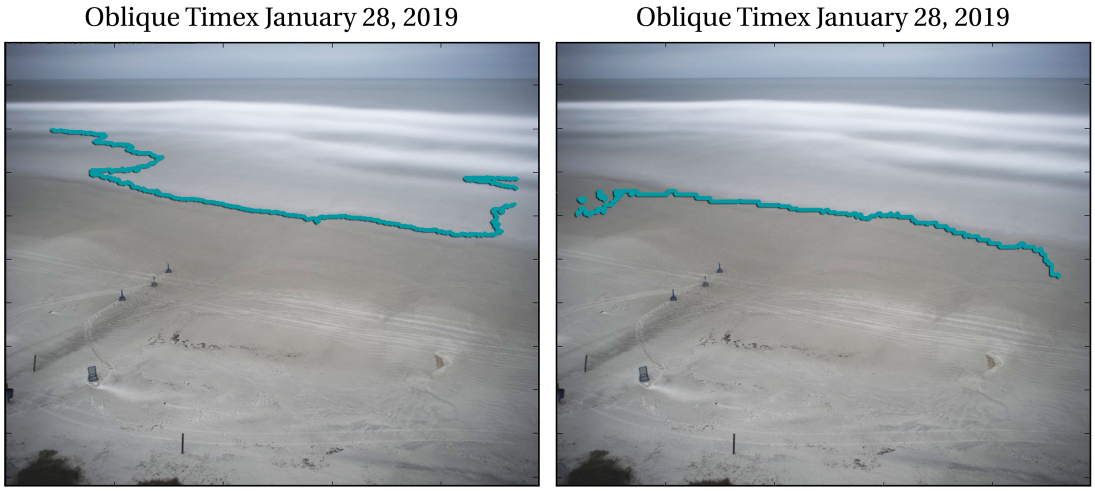

Figure 4.16: Left: generated shoreline using the discriminator function based on grayscale intensities. Right: generated shoreline using the discriminator function based on Hue and Saturation values.

Manual extraction

The final approach for the extraction of shoreline positions was manual extraction. In this case, the shoreline was defined as the visual separation line between water and sand. The shoreline positions were located and stored using a Matlab-script, which used georectified merged Timex imagery as input. In order to increase shoreline visibility, first, the blue tones and image contrast were increased (Figure 4.17). For each input Timex, approximately 50 shoreline points were stored in the alongshore direction, resulting in a spatial density of 1 in 50 meters.

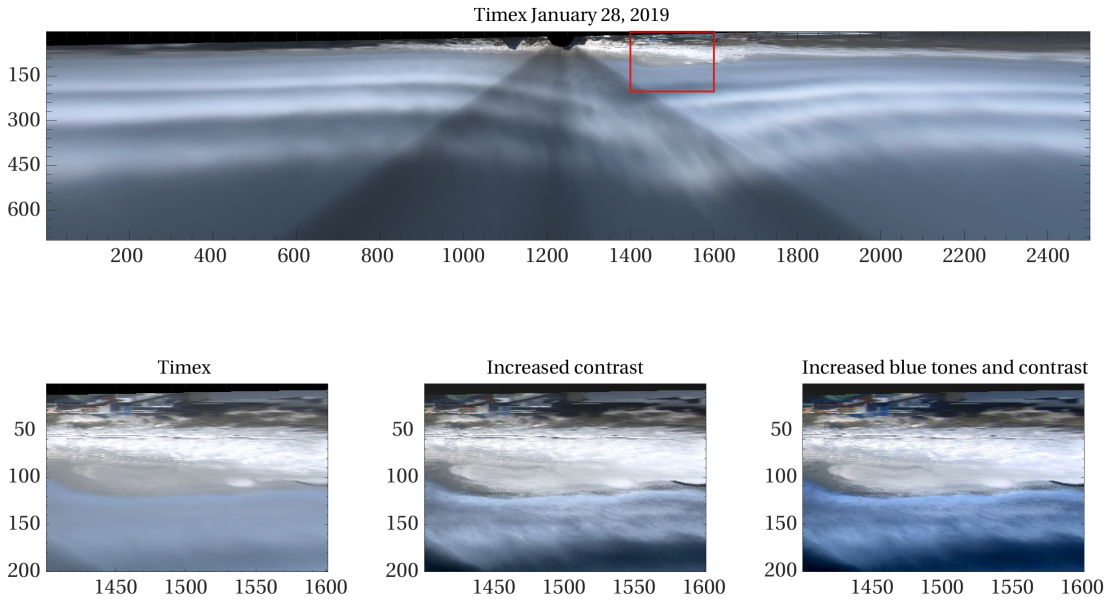

Figure 4.17: Top: the Timex of January 28, 2019. Bottom, from left to right: the standard Timex, the Timex with increased contrast, and the Timex with increased contrast and blue tones.

The shorelines of August 12, 2018 (reflective conditions), and January 28, 2019 (dissipative conditions) are displayed as an example (Figure 4.18). Visually, it seems that both lines follow the shorelines correctly.

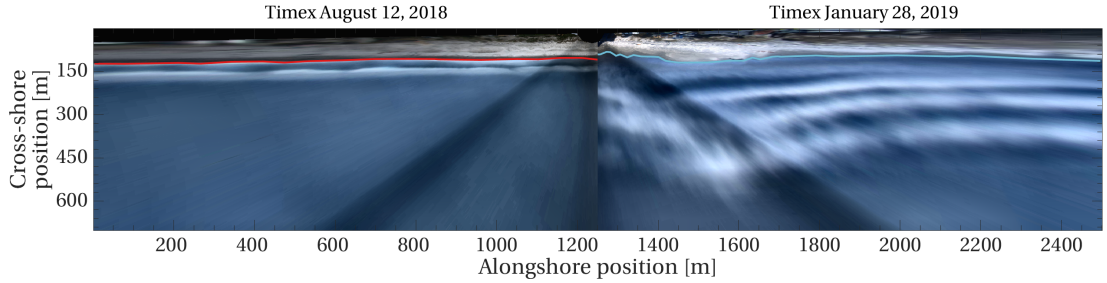

Figure 4.18: Left: the Timex and resulting shoreline of August 12, 2018 (reflective conditions). Right: the Timex and resulting shoreline of January 28, 2019 (dissipative conditions).

To determine the precision of the manual determination approach, 10 randomly selected Timex images were processed five times. Subsequently, the mean shoreline for each image was found. An estimation for the precision was obtained by analyzing the minimum and maximum distance from the mean shoreline (Figure 4.19). In the alongshore, the deviation between the minimum, mean, and maximum varies between 0 to 8 meters. Therefore, the precision of the manual shoreline determination approach is estimated at the order of 10 meters.

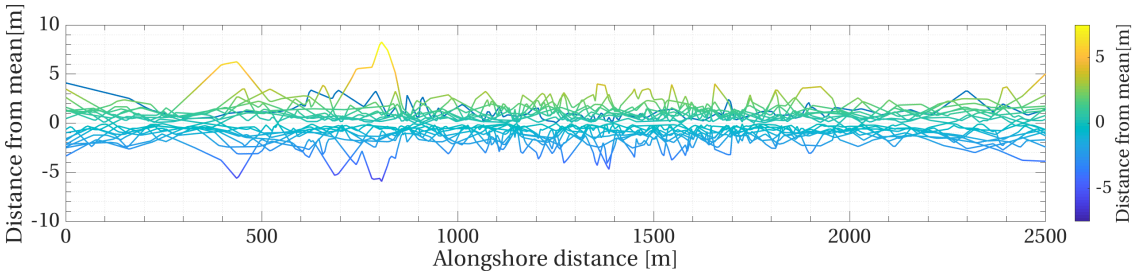

Figure 4.19: An estimation for the precision of the manual determination approach was found by five times processing ten randomly selected Timex imagery. The lines illustrate the deviation from the mean shoreline, which is in the order of 5 - 10 meters.

4.4.3. Constructing time-series

The objective is to find the optimal method for converting imagery data to shoreline position time-series

Method selection

Four extraction approaches were tested and described. The models used in literature were not suitable for New Smyrna Beach (SLIM), or did not provide accurate and robust shoreline positions (CCD and PIC). On the other hand, the manual extraction approach showed promising results. The found shoreline position have an estimated accuracy of the order of 10 meters. Because the errors of the other models were estimated larger, the visual determination approach was used to extract shoreline positions.

Imagery type selection

The shoreline is best visible on the georectified and merged Timex Imagery. The image contrast and blue tones were increased to improve the visibility of the separation line between sand and water.

Input selection

Because shoreline shifts due to the water level change were unwanted in this research, the imagery data set was filtered on an approximately constant water level. Besides, extreme storms were filtered out to limit the wave-run up. This resulted in the following filter demands: $-0.1 \leq \text{MHWL} \leq +0.1$ and $0.5 \leq H_s \leq 3.0$. Compared to the automated extraction models, the visual determination approach is more labor intensive. Therefore, the shoreline positions were extracted once every 3 three days. A stable shoreline position in between the time steps was assumed. Eventually, this led to 165 shoreline positions during the monitoring period.

Summarized

1. Input: georectified and merged Timex Imagery data with increased contrast and blue tones.
2. Extraction method: visual determination of the shoreline with estimated precision of order 10 meters.
3. Output: a time-series of 165 shoreline locations in the period August 2018 to September 2019.

4.5. Concluding remarks

This section concludes Chapter 4 and answers the sub-question: 'How can the nearshore berm and the shoreline positions be optimally extracted from the New Smyrna Beach imagery data?'. Multiple extraction models were discussed to obtain nourishment and shoreline locations. The following methodologies were found to be optimal for the New Smyrna Beach data set:

Sediment outflow position extraction:
Manual determination of the pipe outflow using georectified and merged Timex imagery gave the most accurate position results. The method assumed stable pipe positioning within the tracked day. This resulted in 87 of the in 116 possible positions extractions, which corresponds to a tracking percentage of 75 %.The precision of the manual extraction method is in the order of 5 meters.

Nearshore berm position extraction:
The BLIM model, in combination with georectified merged Timex, resulted in the most (visually) accurate and consistent nearshore berm/bar position time-series. The imagery data-set was filtered to wave height and water level to prevent a varying relation between the patterns of persistent wave breaking and the underlying bathymetry. The wave height was limited to $0.5 \leq H_s \leq 2.5$, and a water level to $-0.50 \leq MLW \leq +0.50$. Eventually, the BLIM model tracked 359 nearshore berm/bar positions, resulting in a temporal density of roughly one a day.

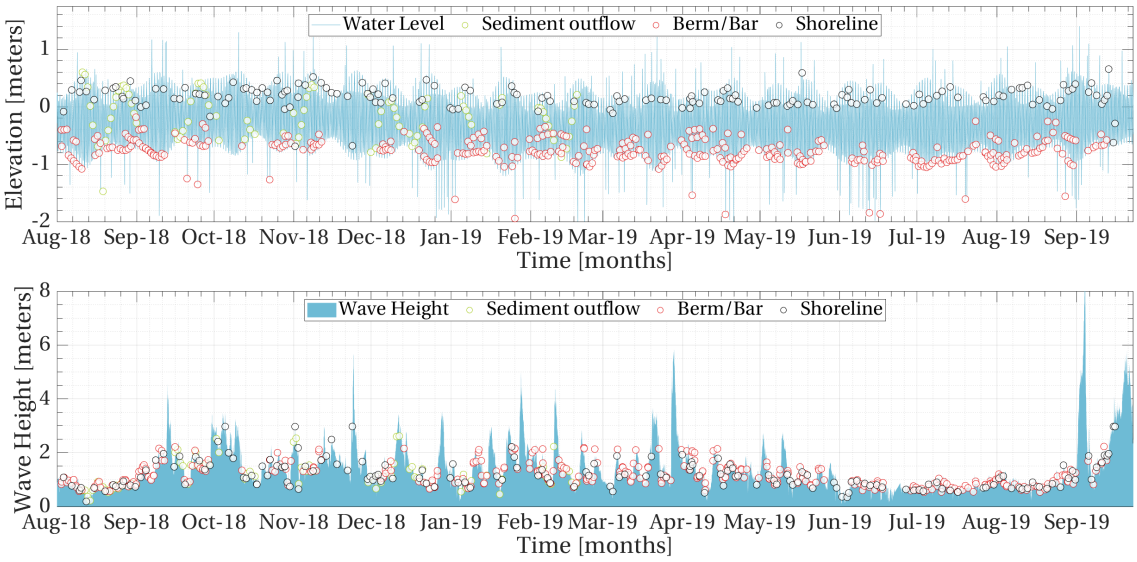

Figure 4.20: The extraction moments of the sediment outflow, berm/bar, and shoreline illustrated together with the corresponding water level (top) and wave height (bottom).

Shoreline position extraction:
Multiple shoreline detection models were tested. In combination with georectified and merged Timex imagery, the manual extraction approach was concluded to deliver the most accurate and consistent results. The shoreline was defined as the visible separation line between water and sand. To increase the visibility of the separation line, the Timex imagery were adjusted with higher contrast and blue tone values. The Timex imagery data-set was filtered to wave height and water level to provide accurate proxies of the shoreline. A constant water level and limited wave run-up are required to limit local fluctuations in the shoreline migration time-series. This resulted in the following filtering demands: $-0.1 \leq MHWL \leq +0.1$ and $0.5 \leq H_s \leq 3.0$. Eventually, the method tracked 165 shoreline positions, which is, on average, once every three days. The

precision of the manual extraction method is in the order of 10 meters.

The extraction moments of the sediment outflow, nearshore berm/bar, and shoreline are illustrated with the corresponding wave height and water level in Figure 4.20. Extraction moments that correspond to water level or wave height outliers were not considered in the proceeding of this study. The outliers were defined if the water level or wave height were smaller/larger than two standard deviations of the aimed filter demand.

5

Description of nearshore berm and shoreline migration

This chapter answers the sub-question: "How did the nearshore berm and shoreline migrate during and after the nourishment activities?". First, the nearshore berm/bar and shoreline migrations are described based on theory. Secondly, the migration patterns are discussed via the time-series obtained in Chapter 4. Finally, the migration predictions and migration time-series are compared in the concluding remarks.

5.1. Introduction

Two method were applied to describe the nearshore berm and New Smyrna Beach shoreline migration:

1. Theoretical predictions based on the findings of Hallermeier (1981), Hands and Allison (1991), and van Rijn and Walstra (2004).
2. Time-series analysis of the extracted imagery data.

5.2. Theoretical migration

The migration patterns of the nearshore berm and shoreline were predicted using theory stated in Chapter 2.

5.2.1. Nearshore berm

Depending on the placement location, a nearshore berm nourishment can be classified as Stable or Active. The classification is based on the nourishment depth, the inner depth of closure (DOC), and outer depth of closure. The outer depth of closure is defined by the significant wave height H_s and the associated standard deviation σ_{Hs} (Hallermeier, 1981):

$$DOC_{outer} = 2H_s + 11\sigma_{H_s} \tag{5.1}$$

Besides the effective wave height, the inner depth of closure formula includes the significant wave period T_s associated with H_s, the gravitational acceleration g, and a grain size term D (Hallermeier, 1981):

$$DOC_{inner} = (H_s - 0.3\sigma_{H_s})T_s\sqrt{\frac{g}{5000D}} \tag{5.2}$$

Theoretically, a berm can be called active if the local placement depth is shallower than the outer and inner depth of closure (Figure 5.1).

The United States Army Corps of Engineers provided the depth of closures boundaries at the Ponce de Leon Inlet for the years 1980 to 2012. The conditions of 2012 were assumed to be similar to the conditions of 2018 and were used for estimating the berm movement. Assuming a D of 0.3 mm and using the wave climate found in Section 3.2, the inner depth of closure was calculated at a value of 9.90 meters and the outer depth of closure of 27.67 meters. With an approximated placement depth of 4.25 meters, the NSB nourishment was be added to the stability graph (Figure 5.1). Based on this classification it is most likely that the NSB nourishment will behave like an active berm with shoreward migration.

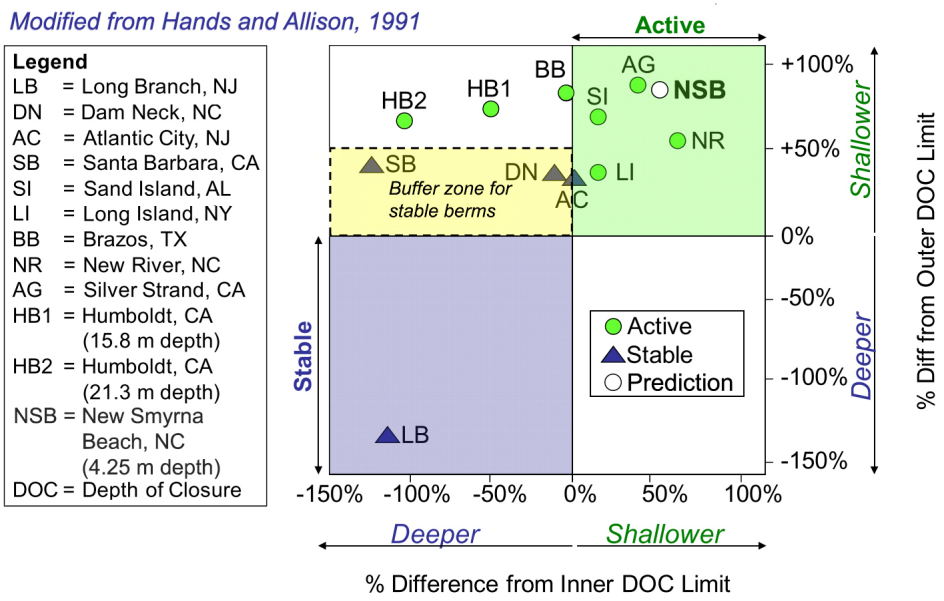

Figure 5.1: Nearshore berm stability graph indicating the berm classifications. (Adapted from Hallermeier (1981).

5.2.2. Shoreline

The theoretical shoreline response to a nearshore berm nourishment can be divided into two effects: the Feeder and Leeside-effect (see also Section 2.3). Depending on the berm classification, the one effect can be more dominant than the other.

- In the case of Stable berms, the Leeside effect results in shoreline advance in the sheltered zone behind the nourishment. Additionally, downdrift of this area, local erosion is expected (Figure 5.2, left).
- In the case of Active berms, both the Leeside and the Feeder effect influence the shoreline. Shoreline advance near the nourishment is expected, because both the Leeside and Feeder effects result in accretion in the sheltered area. Additionally, shoreline erosion is expected downdrift as a consequence of the Leeside effect (Figure 5.2, left, right).

Because the nearshore berm at New Smyrna Beach was classified as Active, both the Feeder and Leeside effect are predicted to play a role. The expected shoreline would, therefore, accrete near the alongshore center of gravity of the nourishment, and erode downdrift.

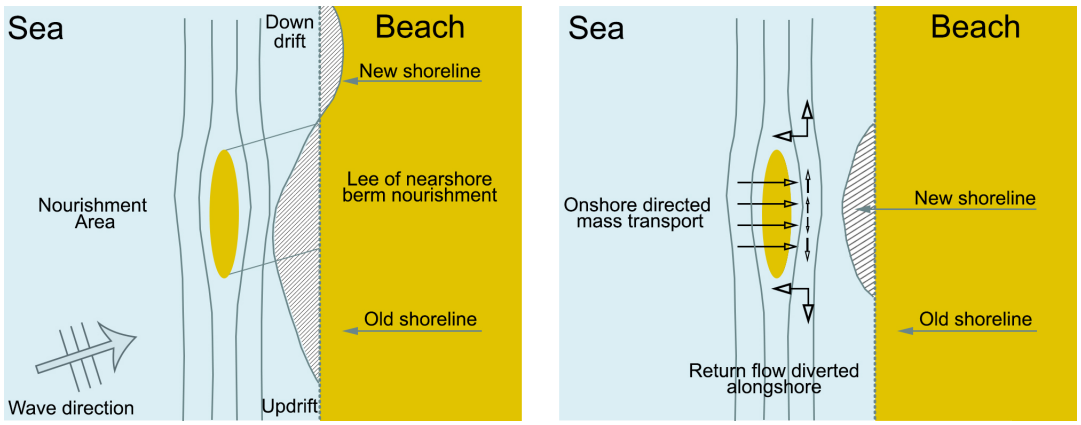

Figure 5.2: Expected shoreline change due to the Leeside-effect (left) and Feeder-effect (right). Adapted from: van Rijn and Walstra (2004).

5.3. Imagery time-series analysis

The description of the imagery time-series starts with specifying the sediment outflow positions. Afterwards, the nearshore berm migration is illustrated by utilizing the sandbar behavior, and, lastly, the shoreline migration is discussed.

5.3.1. Sediment outflow

The optimal method for sediment outflow position extraction led to a time-series of outflow positions in the period from August 2018 to March 2019 (Section 4.2). This time-series was linked to the nourishing time-series (Section 3.4. In total, 87 of the 116 days of the nourishing activities were tracked, which equals 270,000 of the in total 350,000 m^3 of sediments (Figure 5.3). A placement graph was made (Figure 5.4) using the

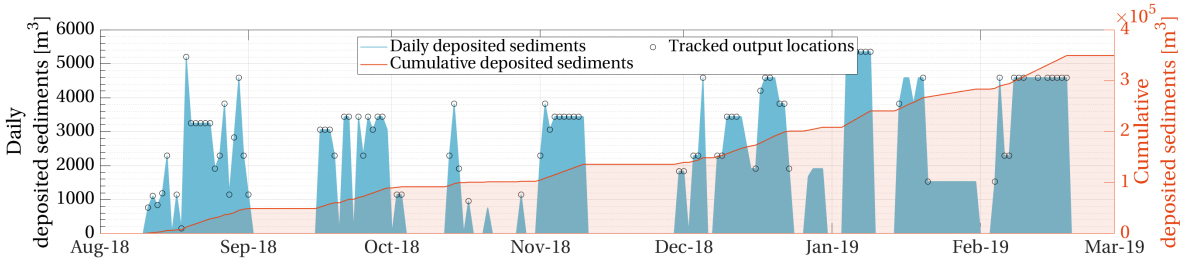

Figure 5.3: The daily (blue) and cumulative (red) sediment deposition time-series and the tracked outflow locations (white dots).

sediment outflow locations and the nourishment time-series. The daily deposited sediment volumes were integrated on a 25 by 25 meters grid. Most sediments were placed between y = 1350 and 1800 meters; the center of gravity of the nourishment was approximately 1500 meters in alongshore direction.

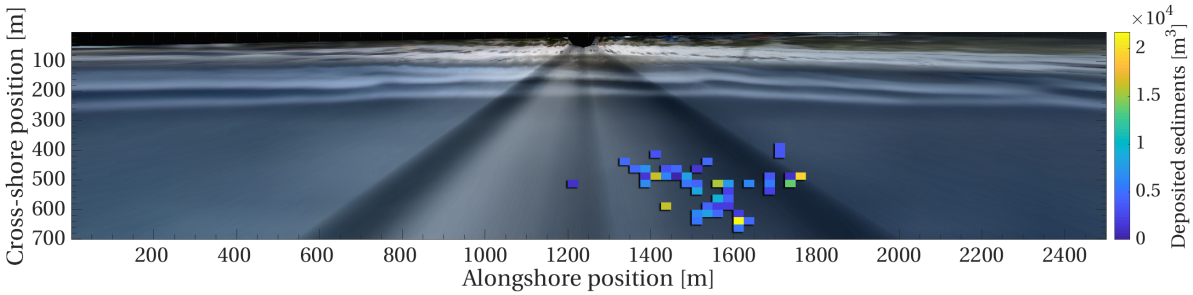

Figure 5.4: The nearshore nourishment dump locations are spatially visualized on a 25 by 25 meters grid. The colors represent the cumulative amount of deposited sediments within a grid cell.

5.3.2. Nearshore berm/bar migration

The optimal position extraction methodology led to a time-series of 359 nearshore berm/bar crest locations in the period August 2018 to September 2019. The nearshore berm/bar migration is discussed in cross-shore and alongshore direction.

Cross-shore migration

The time-series were analyzed through five transects, located at alongshore position y = 600, 1200, 1500, 1800, and 2400 (Figure 5.5). At each time step, the berm/bar crest locations at the five transects were stored. The transects at alongshore position y = 600 (red) and 2400 (purple) were assumed to represent the autonomous berm/bar migration signal, uninfluenced by the nearshore nourishment. The transect at alongshore position y = 1500 (blue) is located near the nourishment center of gravity. The yellow and green transects are positioned near the edges of the nourishment placement.

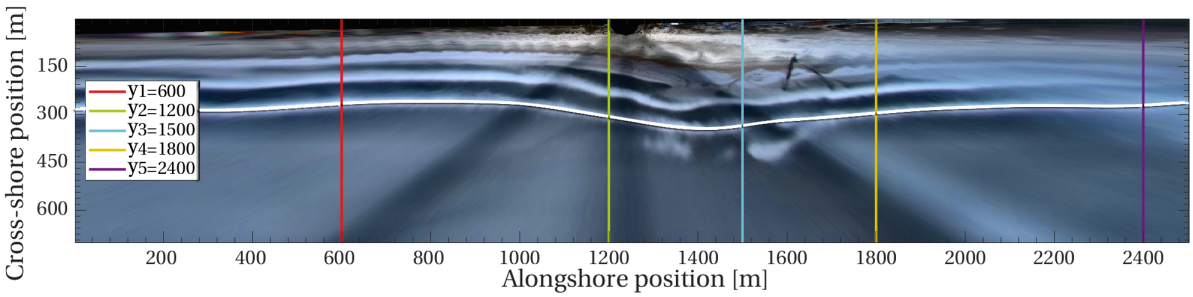

Figure 5.5: The five transects used for describing the cross-shore migration of the nearshore berm nourishment. The displayed bar line (white) was obtained with the BLIM-model.

The autonomous migration signal, which is the average of the berm/bar position at y = 600 and 2400, was subtracted from the time-series at the remaining three transects (green, blue, yellow) to remove remaining noise due to varying water levels and altering wave heights. Subsequently, to make the time-series relative to August 2018, the berm/bar positions at t_0 were also subtracted. Because the resulting signal is relative to the autonomous sandbar trend and the start of monitoring, the influence of the nourishment is visible.

The relative signals of the transects at alongshore position y = 1200 (green), 1500 (blue), and 1800 (yellow) are displayed in Figure 5.6. Positive values indicate an offshore sandbar movement and negative values an onshore movement. The following statements, all relative to t_0 and the autonomous berm/bar trend, can be made:

- From August till September, the berm/bar position at y = 1200, 1500, and 1800 was fairly stable.
- In September, the berm/bar at y = 1500 started to migrate in the offshore direction.
- In October, the berm/bar at y = 1200 and 1800 followed the development and started to migrate offshore.
- At alongshore position y = 1200, a significant offshore movement was followed by a shoreward movement in January.
- In February, the most offshore position berm/bar of 150 meters relative to the autonomous trend was reached. This was at alongshore position y = 1500.
- From February till September, the berm/bar at y = 1200 and y = 1800 slowly moved back from approximately 70 to 30 meters seaward.
- After a substantial shoreward and seaward movement between February and May, the sandbar at y = 1500 converged in the following months with the bar at positions y = 1200 and 1800.

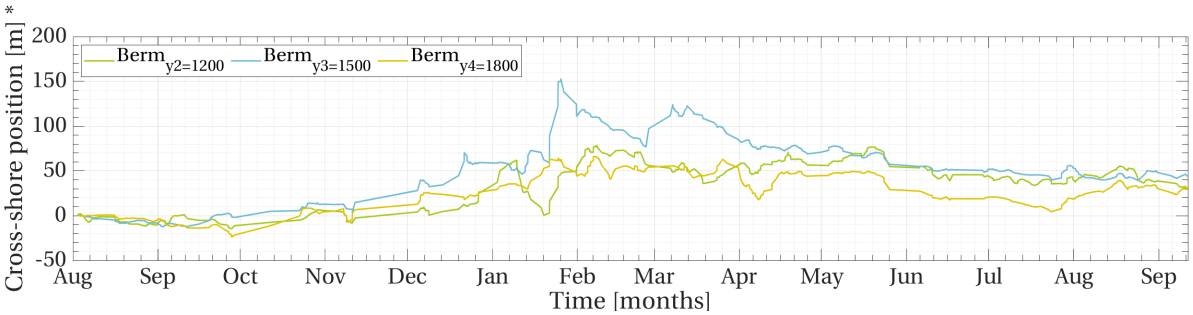

Figure 5.6: The berm/bar positions at alongshore locations y = 1200, 1500, and 1800 meters, relative to $t_0$the autonomous sandbar trend, obtained at locations y = 600 and 2400 meters. On the Y-axis, the positive values indicate a relative offshore position, while negative values indicate a relative shoreward position.

Alongshore migration
The alongshore berm/bar evolution was analyzed by comparing positions at the start of each month (Figure 5.7). In line with the cross-shore migration analyses, the berm/bar time-series are relative to t_0 and the autonomous trend. The following statements can be made:

- No significant growth could be seen in September and October.
- The first alteration in berm/bar shape occurred in November; the maximum offshore position was 40 meters relative to the August and the migration trend.
- From November to February, the berm/bar developed a bulge-like shape, that increased in width and height. The position of the most offshore extent varied between 1400 and 1600 meters alongshore. Additionally, the most offshore extend was found in February and was 120 offshore of t_0 and the migration trend.
- From February to March, no significant changes in shape were found.
- From March to May, the profile spread out in the alongshore direction, resulting in an increased bulge width and a reduction in shoreward extent.
- In June and July, the berm/bar shape developed further, leading to two bumps at y = 1300 and y = 1550. Additionally, the alongshore profile continued to migrate shoreward.
- In September, the maximum difference between the autonomous trend and the berm/bar was 40 meters, indicating that the berm/bar had almost returned to equilibrium.

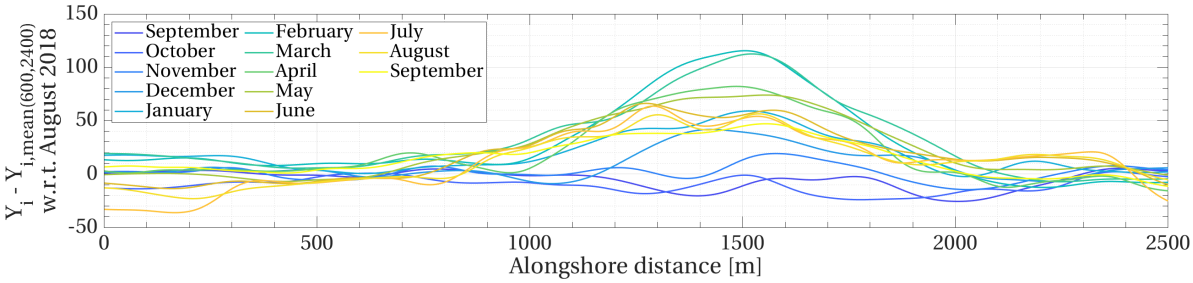

Figure 5.7: The nearshore berm/bar positions at the start of each month, relative to t_0 and the autonomous sandbar trend, obtained at locations y = 600 and y = 2400 meters. On the Y-axis, the positive values indicate a relative offshore position, while negative values indicate a relative shoreward position.

5.3.3. Shoreline migration
The optimal extraction methodology led to a time-series of 165 shoreline locations in the period August 2019 to September 2019. The shoreline migration is discussed in cross-shore and alongshore direction.

Cross-shore migration
In line with Section 5.3.2, the cross-shore shoreline migration is discussed utilizing five transects, location at alongshore position y = 600 (red), 1200 (green), 1500 (blue), 1800 (yellow), and 2400 meter (purple) (Figure 5.8). The shorelines at outer transects, located at y = 600 and 2400, were assumed to follow the autonomous shoreline trend, uninfluenced by the nearshore nourishment. To highlight the influence of the nourishment and to remove noise, the signals at the inner three transects are relative to August 2018 and the autonomous shoreline trend.

The relative shoreline signals at alongshore position y = 1200 (green), 1500 (blue), and 1800 (yellow) are displayed in Figure 5.9. The following statements, all relative to the autonomous shoreline trend, can be made:

- In November, the shoreline at positions y = 1200 and 1500 started to migrate offshore.
- The shoreline at position y = 1800 started advancing in December.
- From December to May, a steady offshore movement at all three transects occurred.
- In May, the maximum shoreline advance of 70 meters appeared at alongshore position y = 1500 meters.

- From May to August, the shoreline did not migrate relative to the autonomous trend.
- In August, a steep shoreward movement followed by a seaward movement occurred at all the transects.

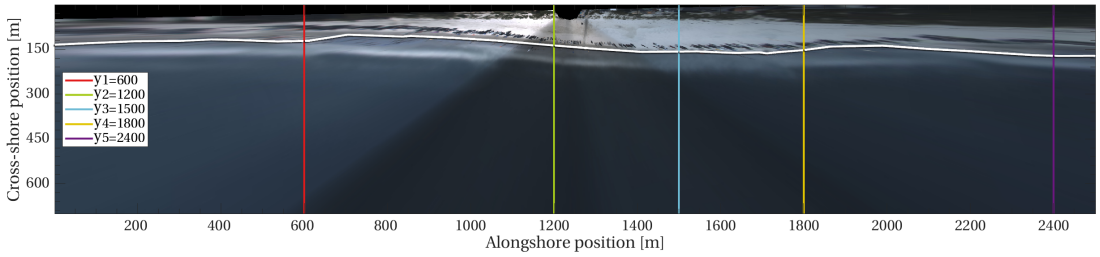

Figure 5.8: The five transects used for describing the cross-shore migration of the shoreline. The displayed shoreline (white) was obtained by visual determination.

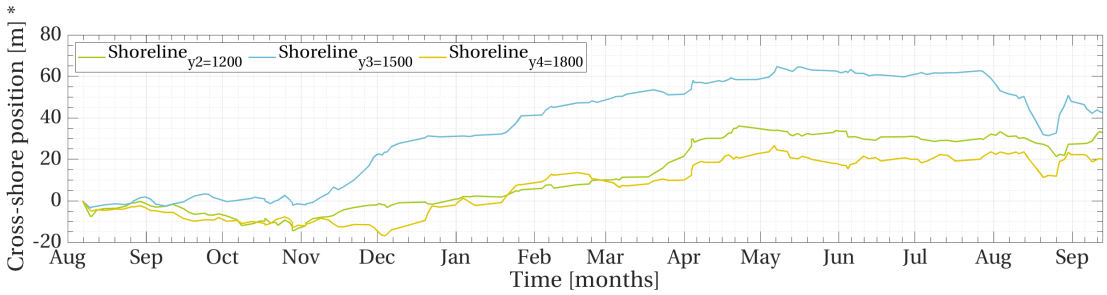

Figure 5.9: The shoreline positions at alongshore locations y = 1200, 1500, and 1800 meters, relative to the autonomous shoreline trend obtained at locations y = 600 and 2400 meters.

Alongshore migration

The alongshore shoreline evolution was analyzed by comparing shoreline positions at the start of each month (Figure 5.10). In line with the previous analyses, the shorelines are relative to t_0 and the autonomous trend. The following statements can be made:

- From September to November, the shoreline was relatively stable with variations of approximately 10 meters.
- The first substantial change in shape was noticed in December. The shoreline extended maximally 20 meters seaward compared to the previous month and obtained a bulge-like shape.
- From December to May, the shoreline advanced seaward to a maximum offshore location of 70 meters and an estimated bulge width of 1000 meters.
- From May to August, the shoreline shape was approximately constant.
- From August to September, the shoreline diffused in alongshore direction, leading to an increased width and a shoreline retreat. The shoreline extent was 45 meters, and the bulge width approximately 1100 meters.

The characteristics of the relative shoreline positions were quantified in more detail. The following methodology was used to extract the height, width, area, and most seaward extent of the shoreline bulge (Figure 5.11, top):

1. First, the most offshore shoreline extent (X_{peak}) and corresponding alongshore location (Y_{peak}) were found.
2. The bulge width was defined as the length between the first points left (Y_1) and right (Y_2) of Y_{peak} having a zero slope.
3. In addition, the bulge height was calculated as the X_{peak} minus the average cross-shore location of the Y_1 and Y_2.
4. The surface area is the area below the shoreline and above the connection line Y_1 and Y_2.

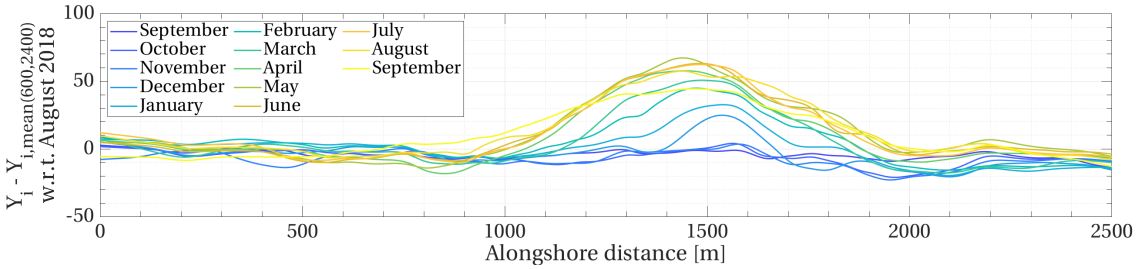

Figure 5.10: The shoreline positions at the start of each month, relative to t_0 and the autonomous sandbar trend, obtained at locations y = 600 and y = 2400 meters. On the Y-axis, positive values indicate a relative offshore migration, while negative values represent relative shoreward migration.

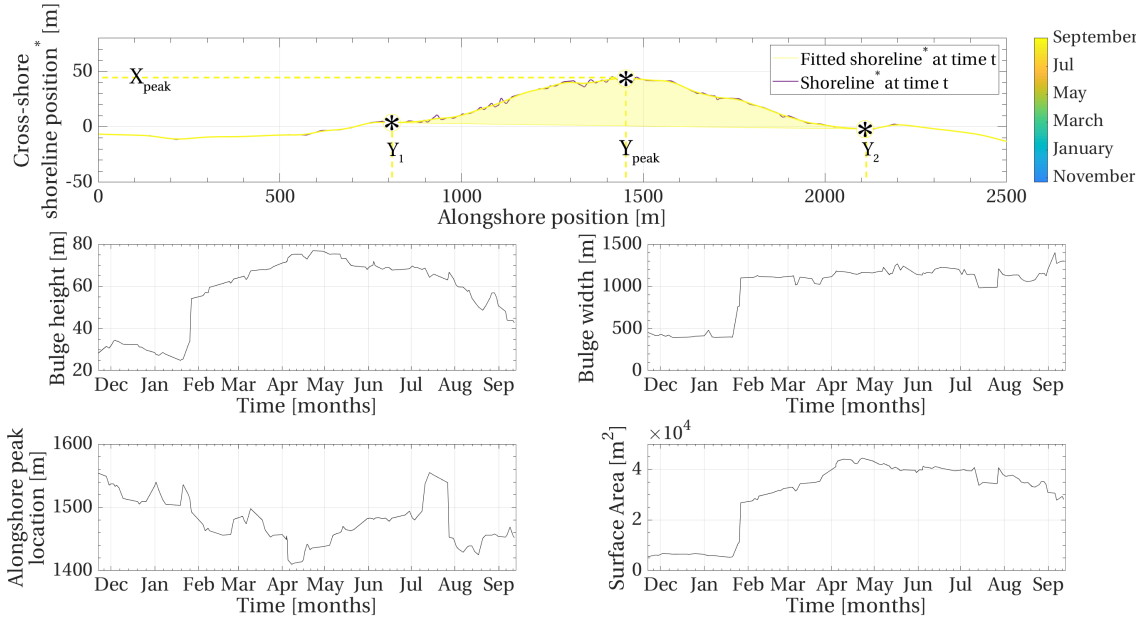

Figure 5.11: The shoreline bulge height and corresponding alongshore location, width and surface area, obtained from the relative shoreline positions. The top image illustrates the extraction methodology of the characteristics, the middle and bottom four the characteristics time-series.

The methodology only holds when the shoreline had a bulge-like shape. In December, this occurred for the first time. Therefore, the time-series of the characteristics starts in December 2018. The following statements can be made according to the Bulge height and alongshore location, width, and surface area (Figure 5.11):

- Bulge height: From December to the end of January, the bulge height decreased slightly to a value of 20 meters. Afterward, a substantial increase of 30 meters took place. From February to May, the bulge height kept growing to a maximum of 75 meters. A decrease in bulge height followed the stable period from May till July.
- Alongshore peak location: In December, the alongshore location of the most seaward extent was near Y = 1550. From December to the second week of April, the locations moved approximately 150 meters to Y = 1400. In the following four months, the peak locations moved back to its initial position at Y = 1550. After a significant alongshore variation in July, the final location of the most seaward extent was near Y = 1450.
- Bulge width: From December to the end of January, a stable bulge width of 450 meters was found. After a steep increase of 550 meters in the third week of January, the bulge width became approximately 1.100 meters. From February to August, the width fluctuated around this value. In September, the largest bulge width of 1.400 meters was found.

- Bulge Area: The bulge surface area started in December with a value of 5,000 m^2 and remained constant until the end of January. After a steep increase of approximately 20,000 m^2, the bulge surface area kept on growing till it reached the maximum value of 45,000 m^2 at the end of April. In May and June, the surface area was constant at a value of 40,000 m^2. After a fluctuation in July, a decrease was found from August to September. The final bulge surface area was 3,000 m^2.

Note: The shoreline data in Figures 5.9 and 5.10 are relative to the autonomous shoreline, which is defined as the average of the shoreline at transects Y = 600 and 2400: $Y_{aut,i}$ = 0.5*$Y_{600,i}$ + 0.5 * $Y_{2400,i}$. However, the graphs in Figure 5.11 are relative to Y_1 and Y_2, which are defined by the shoreline slope. Due to the different definitions, the output can deviates slightly. Additionally, this method only allows for data extraction when the shoreline has a bulge shape. This was from December 2018 to September 2019 (Figure 5.10).

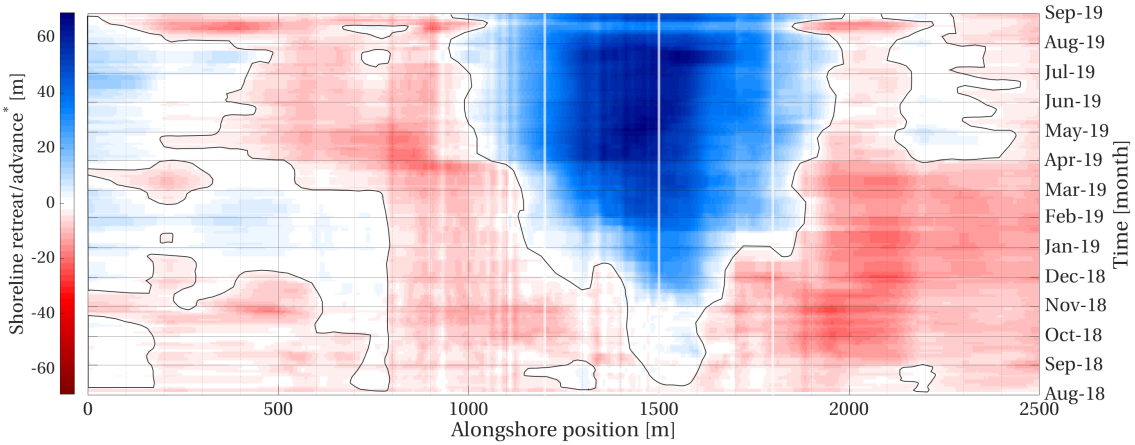

Figure 5.12: Time stack of the shorelines relative to t_0 and the autonomous trend illustrating the erosion and accretion patterns.

According to the predicted shoreline migration (Section 5.2.2), erosion patterns at the side of the shoreline bulge were expected due to the Leeside effect. Therefore, the alongshore shoreline evolution was discussed by focusing on the shoreline advance and retreat patterns in time (Figure 5.12). The accretion and erosion patterns are relative to t_0 and the autonomous shoreline trend.

The following statements can be made regarding the shoreline evolution left of the shoreline bulge (Figure 5.12):

- From August 2018 to December 2018, the shorelines between Y = 0 and the bulge were stable or retreating.
- From December 2018 to March 2019, the shorelines between Y = 0 and Y = 800 accreted the majority of the time. Between transects Y = 800 and the shore bulge, the erosion continued.
- From March 2019 to August 2019, the shorelines between Y = 0 and Y = 400 advanced. On the other hand, erosion occurred at the shorelines between Y = 400 and the bulge.
- In August 2019 to September 2019, mostly erosion was found left of the shoreline bulge.
- Maximal shoreline advance occurred at position Y = 100 (June 2019, 10 meters); maximum shoreline retreat at position Y = 900 (April, 20 meters).

The following statements can be made regarding the shoreline evolution right of the shoreline bulge (Figure 5.12):

- From August 2018 to April 2019, shoreline erosion took place between the shoreline bulge and alongshore position Y = 2500.
- From April 2019 to September 2019, the erosion occurred between the shoreline bulge and Y = 2100. From Y = 2100 to Y = 2400, the shoreline accreded most of the time, followed by erosion at the final 100 meters of the monitoring area.
- Maximal shoreline advance occurred at position Y = (April, 5 meters); maximum shoreline retreat at position Y = 2000 (October, 25 meters).

5.4. Concluding remarks

The sub-question "How did the nearshore berm and shoreline migrate during and after the nourishment activities?" was answered in this chapter. The explanation was given in two-fold. First, the migration was described theoretically, and secondly, according to the imagery time-series.

Migration behavior based on theory

The chapter started with a description of the theoretically expected migration behavior of the nearshore berm/bar. Based on the wave climate, nourishment location, and nourishment characteristics, a shoreward migration was predicted. Subsequently, the migration behavior of the shoreline was discussed. Based on the active berm classification, the shoreline was expected to migrate seawards in the area near the nourishment placement, and shoreward downdrift of the placement area

Migration behavior based on imagery time-series

The nearshore berm/bar and shoreline position time-series were analyzed from August 2018 to September 2019. The theoretical berm/bar migration partly matched the empirical migration behavior. In September 2018, the sandbar near the nourishment location started moving offshore, indicating the feeding and/or attaching of the nourishment. At this position, the maximal offshore berm/bar position was found in February, after which the sandbar gradually moved shoreward again. In September 2019, the berm/bar near the nourishment was almost converged with the autonomous sandbar trend.

Additionally, both the accretion and erosion patterns described by the theoretical migration were found in the shoreline position time-series. In November, four months after the start of the nourishment activities, shoreline advance was noticed near the nourishment location. The accretion continued till May, followed by a period of stable shoreline positioning. Eventually, the start of shoreline retreat was found in August. The maximum shoreline increase was nearly 80 meters (May), and the final shoreline increase approximately 50 meters (September). In total, the beach gained more than 3,000 m^2 of surface area, spread over 1.2 kilometers. Furthermore, local shoreline erosion was found at the edges of the shoreline bulge. From August 2018 to April 2019, shoreline retreat up to 20 meters was found at the left-hand side of the shoreline bulge. On the right-hand side, the erosion values were less, and even shoreline accretion occurred. In the remaining months, the behavior flipped, resulting in more erosion at the left side and less at the right.

6

The influence of the hydraulic forcing on the nearshore berm and shoreline migration

This chapter answers the sub-questions "What is the influence of the hydraulic forcing on the nearshore berm and shoreline migration?". First, the theoretical influence on the nearshore berm/bar and shoreline migrations is discussed. Secondly, the influence of the hydraulic forcing according to the time-series is analyzed. Thirdly, the theoretical description is tested on the empirical found relationships. The chapter ends with the concluding remarks.

6.1. Introduction

First, a description of the theoretical influence of the hydraulic forcing on the nearshore berm/bar and shoreline migration was given. The influence was described using the Feeder and Leeside effects at the alongshore transects y = 750, y = 1500, and y = 2250, see Section 6.2) for the choice of positions.

Subsequently, the influence of the hydraulic climate, characterized by the cross-shore and alongshore wave energy fluxes F_x and F_y, on the nearshore berm/bar and shoreline position time-series was analyzed at alongshore transect y = 750, y = 1500, and y = 2250. In line with the theoretical influence, the shoreline positions time-series at transect y = 750 and 2250 were related to the alongshore component of the wave energy. At alongshore location y = 1500, both the berm/bar and shoreline position time-series were presented together with the cross-shore component of the wave energy.

Lastly, the migration rates of the nearshore berm/bar and shoreline at alongshore positions y = 750, 1500, and 2250 were studied to find indications of the described theoretical relations within the time-series. At all transects, the migration rates were described and, subsequently, colored to cross-shore/alongshore wave power and moment in time to highlight potential patterns.

6.2. Influence based on theory

Theoretically, the influence of the hydraulic forcing on the nearshore berm and shoreline migration can be explained by the Feeder and Leeside-effects. The definitions of both effects are briefly restated.

Leeside effect

The nearshore berm nourishment provides shelter to the shoreline against energetic waves. In the case of inclining waves, the reduction of wave energy in the sheltered area leads to a decrease in the alongshore current, and, therefore, to a locally lower sediment capacity. This allows sediments to settle and, as a consequence, to local accretion. However, downstream of the sheltered area, the alongshore current and transport capacity recover, leading to local shoreline erosion.

Feeder effect
Large waves break at the seaward side of the nearshore berm nourishment. The remaining waves shoal and cause onshore sediment transport. This results in onshore berm migration and shoreline advance in the area behind the nourishment (Bruins, 2016).

Both two effects were used to describe the theoretical influence of the hydraulic forcing on the nearshore berm and shoreline migration at alongshore transects y = 750, y = 1500, and 7 = 2250. The alongshore location y = 1500 was chosen because it is near the alongshore center of gravity of the nourishment, and, therefore, should be influenced strongly by the Feeder effect. Alongshore positions y = 750 and y = 2250 are located at the sides developing shoreline bulge (Figure 5.12), and, therefore, most likely outside the sheltered zone. At this positions, the Leeside effect should influence the shoreline strongly. See Figure 6.3 for an illustration of the shoreline orientation and the relative wave angle of incidence relative.

Based on Feeder and Leeside effects, the influence of the hydraulic forcing at alongshore transect y = 750, 1500, and 2250 can be described as:

- Transect y = 750: incident waves coming from the North-East-East to the South-East-East lead to relative shoreline erosion (Leeside effect).
- Transect y = 1500: normally incident waves lead to relative shoreline accretion and shoreward berm/bar migration (Feeder effect)
- Transect y = 2250: incident waves coming from the North-East-East to the North-North-East lead to relative shoreline erosion (Leeside effect).

6.3. Influenced based on imagery time-series

The cross-shore and alongshore wave energy fluxes F_x and F_y were used to characterize the influence of the hydraulic forcing on the nearshore berm/bar and shoreline position and migration time-series at transects 7 = 750, 1500, and 2250. Before analyzing, the wave energy time-series F_x and F_y were constructed.

6.3.1. Hydraulic forcing

The wave energy flux, also called the waver power (US Army Corps of Engineers, 2015), is suggested as an important parameter for berm and shoreline dynamics (Short (1979), Miller and Dean (2007), Price and Ruessink (2011)). The vectors F_x and F_y describe the cross-shore and alongshore components. The alongshore component of the wave energy flux, F_y, can be used as a proxy of the alongshore current (van Enckevort and Ruessink (2003), Price and Ruessink (2011)).

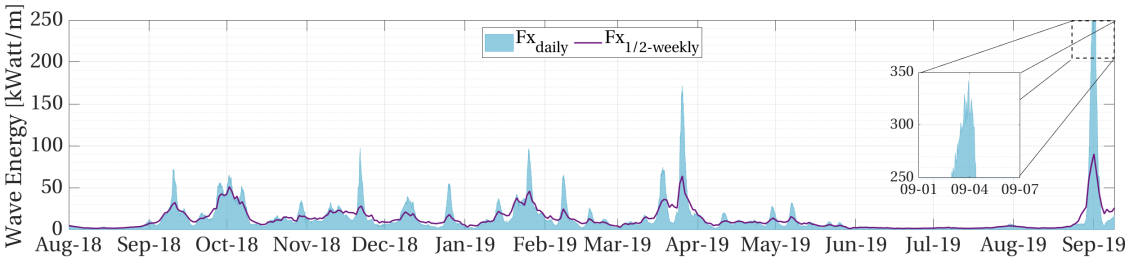

Figure 6.1: Top: the total daily and half-weekly wave energy signal from August 2018 to September 2019. Equation 6.1 was used to calculated the cross-shore wave energy fluxes.

$$E = \frac{1}{8}\rho g H_b^2 \qquad F_x = EC_g cos\theta_b \qquad F_y = EC_g sin\theta_b \tag{6.1}$$

The wave energy was calculated using the breaking wave height H_b, the density of seawater ρ, and the gravitational acceleration g. Additionally, the wave energy fluxes were found by multiplying the wave energy by the shallow water group velocity C_g (= $\sqrt{gh_b}$) and the angle of approach θ_b (Equation 6.1, Miller and Dean

(2007)). The water depth at breaking point h_b was calculated during the linear wave transformation (Appendix C). For both the cross-shore and alongshore fluxes, half-weekly signals were computed to represent a more average behavior. Besides, the cumulative signal of F_y was calculated to illustrate periods with a dominant angle of wave incidence.

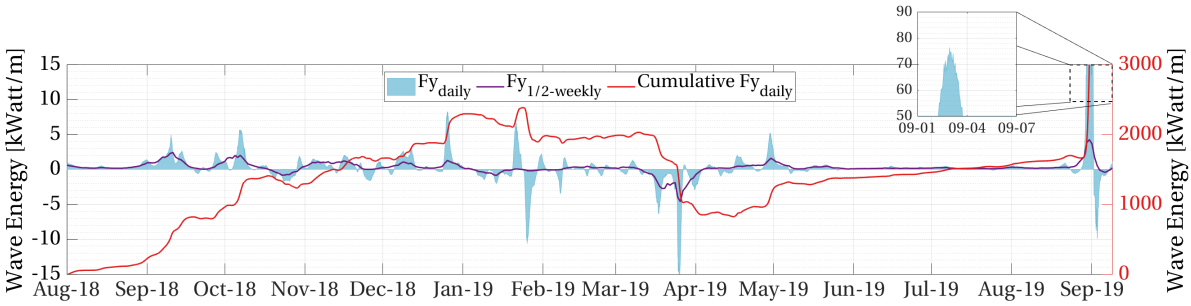

Figure 6.2: The alongshore daily, half-weekly, and daily cumulative wave power signal from August 2018 to September 2019. Equation 6.1 was used to calculated the alongshore wave energy fluxes.

The resulting cross- and alongshore wave energy flux time-series are illustrated by Figures 6.1 and 6.2. Additionally, Figure 6.3 can be used to relate the positive and negative values of the alongshore wave energy flux to the wave direction. In general, negative wave energy corresponds with waves coming from the North-East-East to North-North-East($\theta_b \leq 67.5°$), and positive wave energy with waves coming from the North-East-East to South-East-East ($\theta_b \geq 67.5°$).

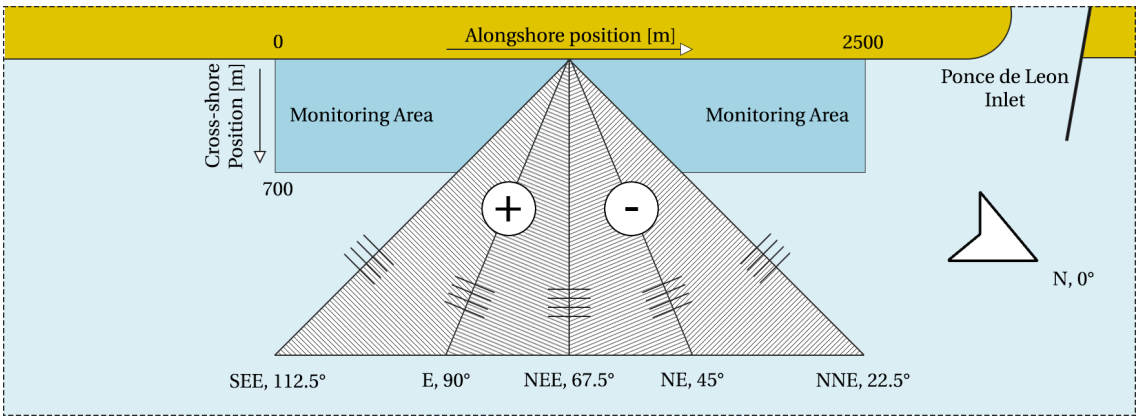

Figure 6.3: A schematic reproduction of the nearshore zone of New Smyrna Beach. The angle of incidence during the monitoring period varied between 22.5° and 112.5°, which translates to -45° degrees and 45° relative to the shore normal.

6.3.2. Position time-series analysis

In line with Section 6.2, the following relations between hydraulic forcing, berm/bar, and shoreline migration were analyzed:

- Transect y = 750: the influence of incident wave energy fluxes F_y on the relative shoreline migration.
- Transect y = 1500: the influence of normally incident wave energy fluxes F_x on the relative berm/bar and shoreline migration.
- Transect y = 2250: the influence of incident wave energy fluxes F_y on the relative shoreline migration.

Transect y = 750

The influence of incident wave energy fluxes F_y on the relative shoreline migration was analyzed at alongshore transect y = 750. First, the shoreline position time-series and the alongshore wave energy time-series

were described. Secondly, the correspondence between the two time-series was stated.

Regarding Figure 6.4, the following statements were made:

- During the monitoring period, the shoreline at transect y = 750 displays a clear advance/retreat trend. From August 2018 to February 2019, the shoreline gradually migrated offshore. Subsequently, from February to May 2019, a rapid shoreline retreat was found, followed by an advance until August. In the last two months, substantial onshore and offshore fluctuations were noted.
- The alongshore wave energy flux F_y varied throughout the time-series. The majority of the peaks correspond with positive wave energy events ($\theta_b \geq 67.5°$). Substantial negative alongshore wave energy peaks ($\theta_b \leq 67.5°$) occurred in February 2019 and March 2019, and a smaller one was found in October 2018.
- From August 2018 to February 2019, general shoreline advance of 5 meters corresponded with, on average, positive alongshore wave energy fluxes (- 0.75 and + 1.25kWatt/m). Subsequently, shoreline retreat of 15 meters (February to May 2019) coincided with a substantial negative alongshore wave energy peak (-5 kWatt/m). From March to August 2019, the shoreline migrated 10 meters offshore, which coincided with low but stable wave energy. The offshore and shoreward fluctuations (order 5 meters) in August and September 2019, both happened simultaneously with positive wave energy events (0.5 and 4 kWatt/m).

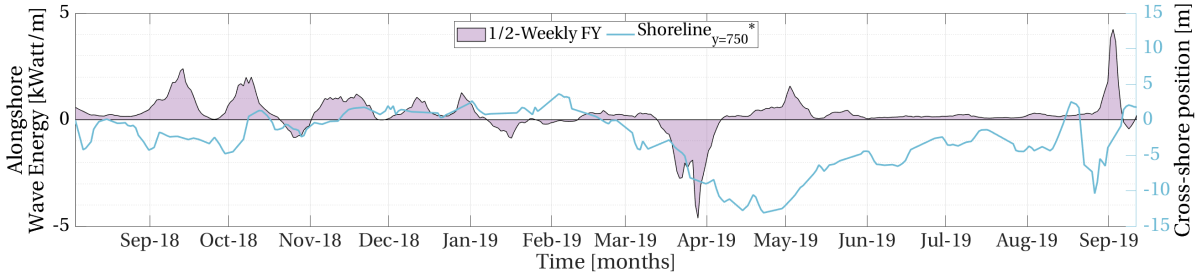

Figure 6.4: The half-weekly alongshore wave energy flux F_y and shoreline migration at transects y = 750 from August 2018 to September 2019. On the Y-axis, positive values indicate a relative offshore migration.

Transect y = 1500

The influence of normally incident wave energy fluxes F_x on the relative berm/bar and shoreline migration was analyzed at alongshore transect y = 1500. First, the position time-series and the cross-shore wave energy time-series were described. Secondly, the correspondence between the berm/bar, shoreline and wave energy time-series were stated.

Regarding Figure 6.5, the following statements can be made:

- From August 2018 to January 2019, the nearshore berm/bar steadily migrated in offshore direction. In February 2019, a substantial offshore movement was found, followed by shoreward and seaward fluctuation. From March 2019 to September 2019, the berm/bar migrated shoreward.
- The start of seaward shoreline migration was found in November 2018. From November to December 2018, the shoreline advance significantly. This period was followed by two months of stable shoreline positioning. From February to May 2019, the shoreline steadily moved in a seaward direction. Subsequently, little to no shoreline change occurred from May to August 2019. In the last two months, shoreline retreat was followed by shoreline advance.
- The wave energy flux F_x time-series displays four significant peaks in the months of October 2018 (50 kWatt/m), February 2019 (45 kWatt/m), April 2019 (65 kWatt/m), and September 2019 (90 kWatt/m). Additionally, smaller increments can be noticed in September 2018 (35 kWatt /m), November 2018 (24 kWatt/m), December 2018 (16 kWatt/m), and May 2019 (12 kWatt/m).
- From August 2018 to January 2019, no one-to-one relationship between the wave energy peaks and berm/bar migration can be seen. However, when focusing on more general behavior, offshore berm/bar migration (50 meters) was found during energetic wave conditions (0 – 50 kWatt /m). Subsequently, in February 2019, the wave energy peak of 45 kWatt/m coincided with an offshore movement 90 meters of the berm/bar. The third substantial wave energy peak (March 2019, 65 kWatt/m), co-occurred with

both shoreward (70 meters) and offshore (40 meters) berm/bar migration. In the remaining months, the berm moved steadily shoreward while the wave energy was relatively low. The peak in September did not result in any substantial berm/bar movement.

- From August to November 2018, stable shoreline positioning was found in correspondence with substantial cross-shore wave energy (50 kWatt/m). The shoreline advance of 30 meters in November 2018 coincided with the wave energy conditions of maximally 27.5 kWatt /m. From December 2018 to January 2019, stable shoreline positioning was found in co-occurrence with mildly energetic conditions. Subsequently, shoreline advance was found from February to May 2019. During this accreting period, the peaks in the wave energy time-series (50 kWatt/m in February, 65 kWatt/m in April) seem to correspond with increases in the offshore shoreline migration rate. In total, the shoreline advance 30 meters. Additionally, stable shoreline positioning and low energy wave conditions coincided from May to August 2019. In August and September, onshore migration of 30 meters corresponded with low energy conditions (5 kWatt/m), and offshore migration of 20 meters with substantial cross-shore energy conditions (70 kWatt/m).

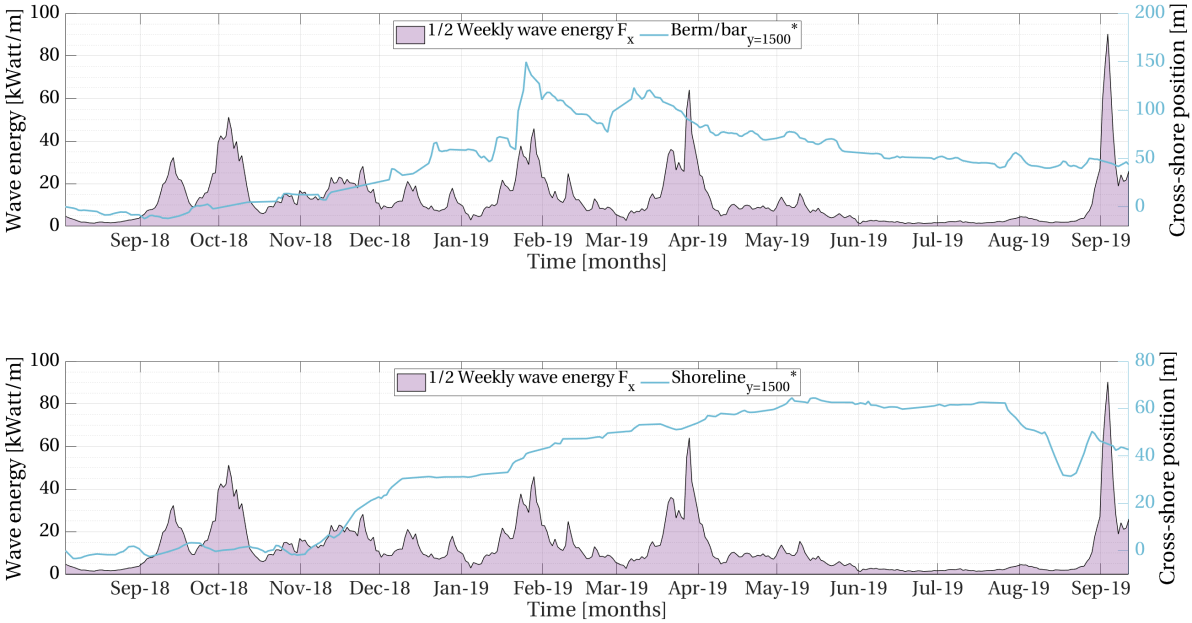

Figure 6.5: Top: the half-weekly wave energy flux F_x and shoreline migration at transects y = 1500 from August 2018 to September 2019. Bottom: the half-weekly wave energy flux F_x and berm/bar migration at transects y = 1500 from August 2018 to September 2019. On the Y-axis, positive values indicate a relative offshore migration.

Transect y = 2250

The influence of incident wave energy fluxes F_y on the relative shoreline migration was analyzed at alongshore transect y = 2250. First, the shoreline position time-series and the alongshore wave energy time-series were described. Secondly, the correspondence between the two time-series was stated.

Regarding Figure 6.6, the following statements can be made:

- In correspondence with the shoreline at transect y = 750, a clear erosion/accretion trend is visible in shoreline time-series at y = 2250. Shoreline retreat started in August 2018 and continued to March 2019, followed by a significant shoreline advance (March to May 2019), and a period of relative stability (May to September 2019).
- Restated from transect y = 750: the alongshore wave energy flux F_y varied throughout the time-series. The majority of the peaks correspond with positive wave energy events ($\theta_b \geq 67.5°$). Substantial negative alongshore wave energy peaks ($\theta_b \leq 67.5°$) occurred in February 2019 and March 2019, and a smaller one was found in October 2018.
- From August 2018 to January 2019, the general offshore shoreline migration trend corresponded with positive alongshore wave energy. In the five months, the shoreline eroded 15 meters, and the wave

energy varied between -1 and + 2.5 KWatt/m. In January, low negative (-1 KWatt/m) and positive alongshore wave energy (+ 0.5 KWatt/m) coincided with shoreline advance and retreat (5 meters). Additionally, the substantial negative wave energy peak in February (-5 KWatt /m) happened simultaneously with significant shoreline advance (15 meters). From April to September 2019, the positive wave energy co-occurred with steady decay of the shoreline positions (5 meters).

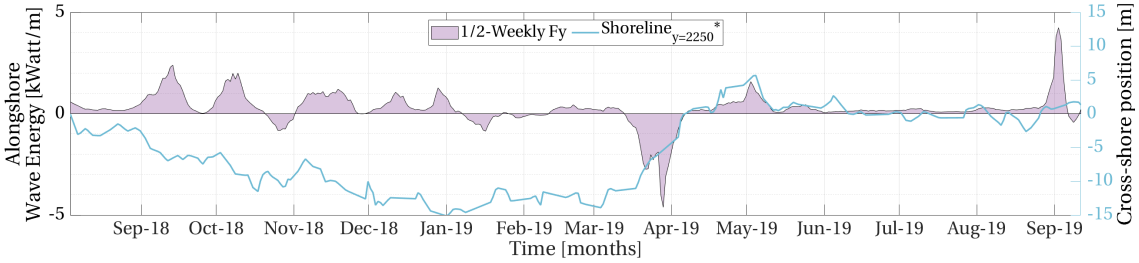

Figure 6.6: The half-weekly alongshore wave energy flux F_y and shoreline migration at transects y = 2250 from August 2018 to September 2019. On the Y-axis, positive values indicate a relative offshore migration.

6.4. Comparison theory and time-series

This section aimed to find indications of the theoretical influence of the hydraulic forcing in the berm/bar and shoreline migration time-series. The theoretical influence, described in Section 6.2 at alongshore transects y = 750, 1500, and 2250:

1. Transect y = 750: incident waves coming from the North-East-East to the South-East-East (negative alongshore wave energy) lead to relative shoreline erosion (Leeside effect).
2. Transect y = 1500: normally incident waves lead to relative shoreline accretion and shoreward berm/bar migration (Feeder effect)
3. Transect y = 2250: incident waves coming from the North-East-East to the North-North-East (positive alongshore wave energy) lead to relative shoreline erosion (Leeside effect).

At each transect, the migration rates of the berm/bar and shoreline were discussed first, to investigate to most dominant migration behavior. Second, the migration rates were color to wave energy to analyze the relationship between wave energy and migration behavior. Thirdly, the migration rates were color to time the see if more dominant behavior patterns were visible during specific periods of the year.

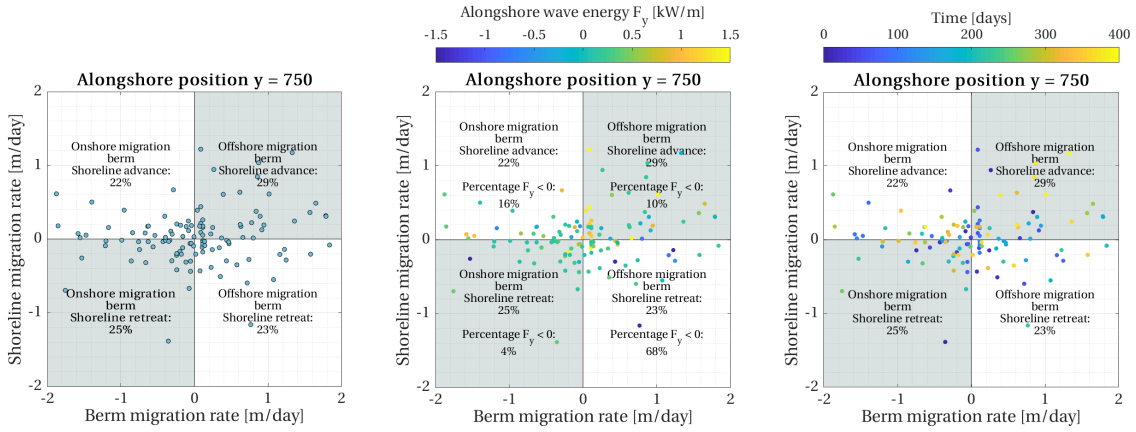

Figure 6.7: Left: the berm/bar and shoreline migration rates from August 2018 to September 2019 at alongshore transect y = 750. Middle: berm/bar migration rates color by alongshore wave energy. Right: berm/bar migration rates color by moment in time.

Transect y = 750

The migration rates at alongshore transect y = 750 were illustrated in Figure 6.7. The figure was analyzed from the left to the right image and led to the following statement:

- The berm/bar and shoreline migration rates at alongshore transect y = 750 are illustrated at four quartiles(Figure 6.7, left). As can be seen, the migration rates are evenly spread, as each quartile represents nearly 25 %. This indicates that shoreline erosion and accretion happened both approximately 50 % of the time.
- To reveal potential patterns, the migration rates are color by alongshore wave power(Figure 6.7, middle). Additionally, the percentages of negative alongshore wave power that occurred in the corresponding quartile are stated. Shoreline advance corresponds with 16 + 10 = 26 % of the total alongshore negative wave energy. On the other hand, shoreline erosion coincided with 4 + 68 = 72 % of the total negative alongshore wave energy.
- Time-wise, the input migration time-series can be divided into two periods: before and after finishing of the nourishment activities. To potentially clarify patterns within the data, the migration rates were color by moment in time (Figure 6.7, right). However, the data is scattered in time, and no real statements can be deducted.

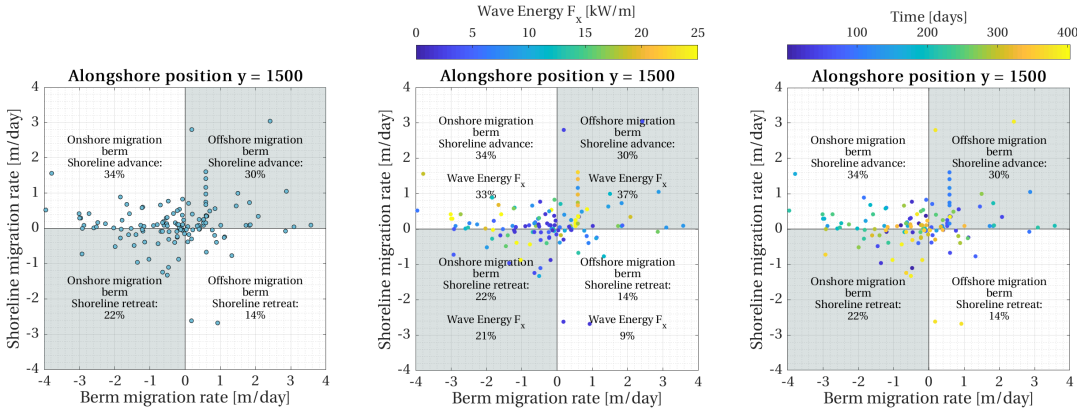

Figure 6.8: Left: the berm/bar and shoreline migration rates from August 2018 to September 2019 at alongshore transect y = 1500. Middle: berm/bar migration rates color by cross-shore wave energy. Right: berm/bar migration rates color by moment in time.

Transect y = 1500

The migration rates at alongshore transect y = 1500 were illustrated in Figure 6.8. The figure was analyzed from the left to the right image and led to the following statement:

- The berm/bar and shoreline migration rates at alongshore transect y = 1500 are illustrated at four quartiles(Figure 6.8, left). Compared to the migration rates at transect y = 750, shoreline advance occurred more frequently. During 34 + 30 = 64 % of the time, the shoreline accreted while negative shoreline erosion rates only occurred at 22 + 14 = 36 % of the time. Onshore berm migration and shoreline advance happened during most of the time (34%). Additionally, the maximum shoreline (+/- 3 m/day) and berm/bar (+/- 4 meters/day) migration rates were found to be higher than at alongshore transect y = 750 (+/- 1.5 and +/-2 meters/day).
- The migration rates color by cross-shore wave energy are illustrated in the middle image of Figure 6.8. Additionally, the percentages of cross-shore wave power that occurred in the corresponding quartile are stated. Shoreline advance occurred simultaneously with 33 + 37 = 70 % of the total cross-shore wave energy. On the other hand, only 21 + 9 = % coincided with shoreline retreat.
- The migration rates were color by moment in time to clarify potential patterns within the data (Figure 6.8, right). Additionally, the migration rates occurring after completion of the nourishment are illustrated with a black edge. Visually, the two left quartiles (onshore berm migration and shoreline advance/retreat) occurred more often from approximately 200 days (end of February 2019) to 400 days

(September 2019). Additionally, offshore berm migration and shoreline advance (top right quartile) happened mostly during the first 200 days of the time-series (August 2018 to February 2019)

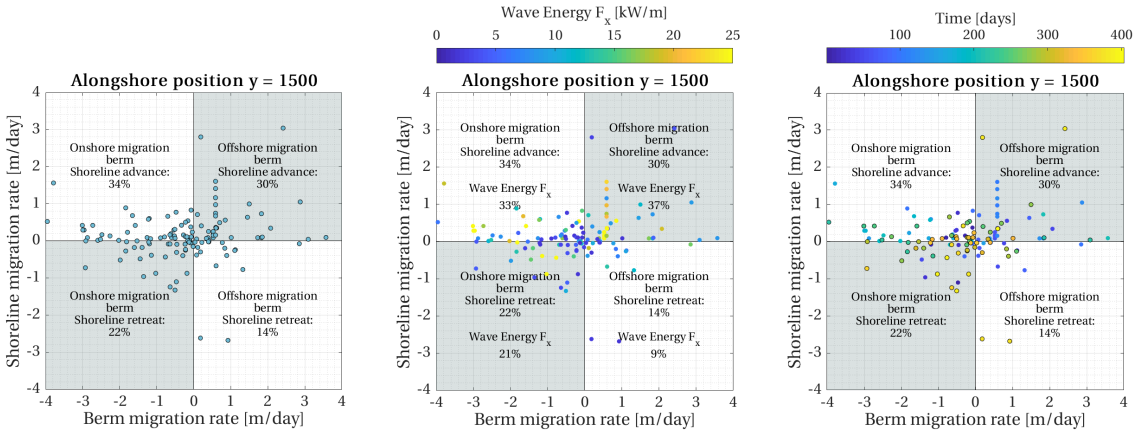

Figure 6.9: Left: the berm/bar and shoreline migration rates from August 2018 to September 2019 at alongshore transect y = 2250. Middle: berm/bar migration rates color by alongshore wave energy. Right: berm/bar migration rates color by moment in time.

Transect y = 2250

The migration rates at alongshore transect y = 2250 were illustrated in Figure 6.9. The figure was analyzed from the left to the right image and led to the following statement:

- The berm/bar and shoreline migration rates at alongshore transect y = 2250 are illustrated at four quartiles(Figure 6.9, left) and are found to be similar to the migration rates at alongshore transect y = 750. The maximum shoreline and berm/bar migration rates were approximately +/- 1 and +/- 2 meters/day. Additionally, the migration rates are evenly spread, resulting in quartiles that represent nearly 25 % of the conditions.
- The migration rates color by cross-shore wave energy are illustrated in the middle image of Figure 6.9. Additionally, the percentages of cross-shore wave power that occurred in the corresponding quartile are stated. Shoreline advance occurred simultaneously with 24 + 14 = 38 % of the total positive alongshore wave energy. On the other hand, only 21 + 40 = 61 % coincided with shoreline retreat.
- The migration rates were color by moment in time to highlight potential patterns within the data (Figure 6.9, right). By visually analyzing the scatter data, it seems that the two lower quartiles correspond with migration data from the period 0 – 200 days (the end of February 2019), while the top quartiles more match to data from the period 200 – 400 days (March to September 2019). This matches the statements from Section 6.3.2.

6.5. Concluding remarks

This section concludes Chapter 6 and answers the sub-question "What is the influence of the hydraulic forcing on the nearshore and shoreline migration?" The question was answered in twofold, first by describing the influence based on theory, and second, based on the analysis of the imagery time-series. Finally, the theoretical description was tested on the empirical found relationships. All analyses were performed at the sides of the alongshore nourishment placement (y = 750, 2250), and at the alongshore location of the center of gravity of the nourishment (y = 1500).

Influence based on theory

Theoretically, the influence of the hydraulic climate on the berm/bar and shoreline migration can be discussed by the Feeder and Leeside effect. Implying both the New Smyrna Beach site, the influence was described as:

- Transect y = 750: incident waves coming from the North-East-East to the South-East-East, or negative

alongshore wave energy, lead to relative shoreline erosion (Leeside effect).

- Transect y = 1500: normally incident waves, or positive cross-shore wave energy, lead to relative shoreline accretion and shoreward berm/bar migration (Feeder effect)
- Transect y = 2250: incident waves coming from the North-East-East to the North-North-East, or positive alongshore wave energy, lead to relative shoreline erosion (Leeside effect).

Influence based on imagery time-series
The hydraulic forcing, defined as the alongshore and cross-shore components of the wave energy, was related to the berm/bar and shoreline position time-series at transects y = 750, 1500, and 2250. Overall, no one-to-one relations were established, but certain correspondence in the time-series trends was found.

At transect y = 750, located outside of the sheltered area of the nourishment, the shoreline time-series were related to the alongshore component of the wave energy F_y. Except for May 2019, positive alongshore wave energy events up to 2.5 kWatt/m did not result in a significant change in shoreline (order 5 meters). On the contrary, shoreline retreat of 15 meters coincided with a substantial negative alongshore wave energy event (April, -5 kWatt/m).

At transect y = 1500, located at the alongshore center of gravity of the nourishment, the berm/bar and shoreline time-series were related to the cross-shore component of the wave energy F_x. From August 2018 to March 2019, offshore berm migration coincided with cross-shore wave energy. This period exactly matches the period of nourishing. From March to September 2019, onshore berm migration corresponded to cross-shore wave energy.

Additionally, stable shoreline positioning was found in correspondence with substantial cross-shore wave energy (50 kWatt/m) from August to November 2018. From November to May 2019, cross-shore wave energy corresponded with 30 meters of offshore shoreline movement. Stable shoreline positioning corresponded to low wave energy from May to August 2019. In the last two months, shoreline retreat (30 meters) was found during low energy conditions and, subsequently, shoreline advance (20 meters) coincided with significant shoreline energy.

At transect y = 2250, located outside of the sheltered area of the nourishment, the shoreline time-series were related to the alongshore component of the wave energy F_y. From August 2018 to January 2019, the general offshore shoreline migration trend corresponded with positive alongshore wave energy. Additionally, the substantial negative wave energy peak in February (-5 KWatt /m) happened simultaneously with significant shoreline advance (15 meters). From April to September 2019, the positive wave energy co-occurred with steady decay of the shoreline positions (5 meters).

Comparison
At alongshore transect y = 750, strong indications of the theoretical influence were found in the berm/bar migration time-series. Between August 2018 to September 2019, 72 % of the total negative wave energy was related to shoreline retreat.

At alongshore transect y = 1500, indications of the theoretical influence were found in the berm/bar and shoreline migration time-series. During 34 % of the time, onshore berm migration corresponded with shoreline advance. In total, 33 % of the cross-shore wave energy could be related to this migration behavior. Visually determined, onshore berm migration and shoreline advance occurred mostly from March to September 2019.

At alongshore transect y = 2250, indications of the theoretical influence were found in the berm/bar migration time-series. Between August 2018 to September 2019, 62 % of the total positive wave energy was related to shoreline retreat. Visually determined, offshore berm migration occurred mostly from March to September 2019.

7

Discussion

This chapter discusses the most relevant results of the study by comparing it to previous findings in the literature. Additionally, it elaborates on the assumptions and inaccuracies of the imagery extraction methods.

7.1. Reflection of results

This section reflects on the results of Chapter 5 and Chapter 6 in four steps. First, the results of this thesis are used to discuss the benefits of Argus monitoring. Second and third, the Feeder and Leeside effects are discussed by reflecting on the berm and shoreline position time-series. Fourth, the efficiency of nearshore berm nourishments is discussed.

7.1.1. Potential benefits of Argus monitoring

The berm/bar and shoreline position time-series obtained by the Argus imagery data display fluctuations of 5 to 10 meters on a timescale of days. In general, it is not uncommon to find natural fluctuations of the morphology in a coastal system with varying wave conditions. The variability of the beach morphology at Noordwijk, The Netherlands, is used as an example. Quartel et al. (2007) describe the daily to seasonal cross-shore behavior of a sandbar using Argus imagery data. On average, it was found that the daily migration behavior was 7 meters per day, while the seasonal migration was only 0.1 meters per day. Besides the natural variability of the berm/bar and shoreline positions, the imagery extraction approaches may partly contribute to the observed fluctuations.

Depending on the aim of the measurements, daily data can be preferred over individual bathymetry surveys taken at longer time intervals. The fluctuations in the daily berm migration signal are in the order of 5 to 10 % of the total migration signal. This can be acceptable if there is aimed at finding, for example, the yearly net migration rate. However, when the aim is to describe the effect of a single storm, the migration response can be in the same order as the observed fluctuations. In that case, daily data can be preferred to describe the morphodynamic response. By signal averaging, the fluctuations can be reduced, which makes the influence of the storm better visible. Therefore, daily data, such as Argus imagery, can help to correctly describe processes related to the behavior of nearshore nourishments and the corresponding shoreline.

The signal averaging was used in this thesis to highlight the influence of the nearshore berm on the nearshore zone of New Smyrna Beach. All berm/bar and shoreline position time-series were made relative to respectively the autonomous berm and autonomous shoreline signals. By making the time-series relative, potential noise due to varying water levels and run-up was removed. Besides the removal of these daily variations, the seasonal sand bar and shoreline dynamics described by Hoefel and Elgar (2003) and Stive et al. (2002) were eliminated from the times-series. The autonomous signals were calculated as the average of the signals obtained at nearly 1,000 meters left and right from the nourishment center. At these locations, it was assumed that the nourishment was not able to influence the sandbar and shoreline systems. All in all, the daily Argus imagery data enabled the construction of position time-series covering the berm/bar and shoreline migration due to the nourishment only.

7.1.2. The Feeder effect

No one-to-one relationships were found between the berm/bar migration and cross-shore wave energy fluxes at New Smyrna Beach. This implies that significant berm/bar migration was not necessarily linked to individual energetic wave events. However, from a broader perspective, relative offshore berm/bar migration was found with energetic wave conditions in the first six months. In the remaining seven months, the berm/bar migrated relatively onshore with both energetic and non-energetic conditions (Figure 7.1).

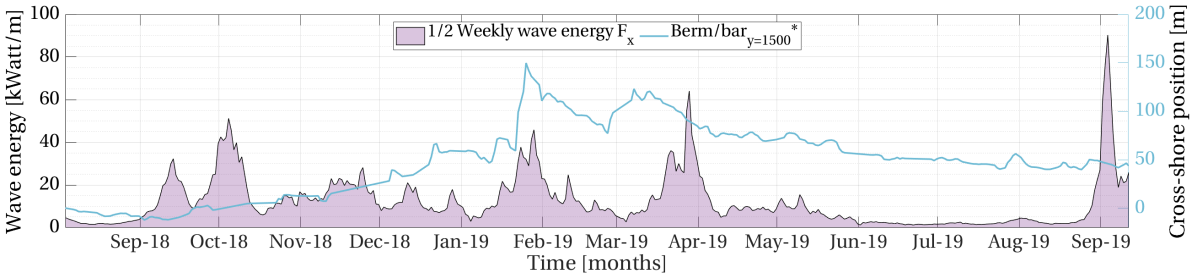

Figure 7.1: The half-weekly cross-shore wave energy (left axis) and the relative berm/bar migration (right axis) near the nourishment center from August 2018 to September 2019.

In 1999, a nearshore berm nourishment similar to New Smyrna Beach was carried out at Egmond, The Netherlands (van Duin et al., 2004b). The development of the nearshore berm nourishment and double sandbar system was analyzed to help understand the behavior at New Smyrna Beach. The nourishment, constructed with a split barge, was placed just seaward of the outer sandbar (Figure 7.2, left). After 18 months, the outer bar was migrated shoreward, and a through had established between the nourishment and the outer bar. The nourishment seemed to replace the sandbar locally and acted as the new outer bar (Figure 7.2, middle). After 30 months, the nearshore berm nourishment was decreased in height, and no further onshore migration of the sandbar was found (Figure 7.2, right). In general, the observed onshore and subsequent stable positioning of the sandbar is somewhat remarkable because the net annual sandbar migration at Egmond was directed offshore

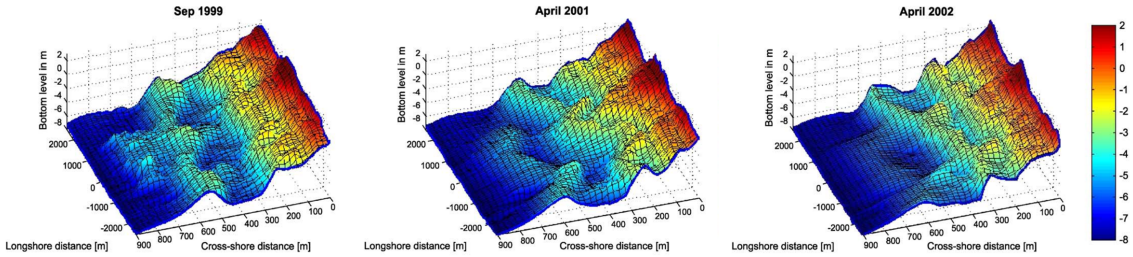

Figure 7.2: Measured Egmond bathymetries in meters relative to NAP: September 1999 (left), April 2001 (middle), and April 2002 (right). Adapted from: van Duin et al. (2004b).

The following description is hypothesized to characterize the nearshore berm nourishment and sandbar migration behavior at New Smyrna Beach. It has similarities with earlier observations found at Egmond and, therefore, confirms the findings of van Duin et al. (2004b):

- As predicted by the active classification (Hands and Allison (1991) and Brutsché et al. (2019)), the nearshore berm nourishment migrated towards the shore after placement (Figure 7.3, i and ii). However, the time-series in Figure 7.1 suggests an offshore migration of the berm/bar in the first six months. The way of analyzing can explain the deviation between the imagery data and time-series. In this report, the sandbar dynamics were monitored to observe the influence and/or attachment of the nearshore berm nourishment. Eventually, the onshore migrating berm caused offshore migration of the sandbar (see the next bullet-point). Because, from that point onward, no deviation could be made between the berm and sandbar, the terminology berm/bar was used.
- In line with the findings at Egmond, the nearshore berm nourishment locally replaced the original sandbar (Figure 7.3, iii). In the shadow zone, the old sandbar migrated shoreward under the influence

of the remaining shoaling waves (Hoefel and Elgar (2003), Ruessink et al. (2007)). This phenomenon, earlier found by Wijnberg and Holman (2008), is called a shoreward propagating accretionary wave (SPAW). Price et al. (2017) confirmed the onshore migration of SPAWs during less energetic wave conditions. These conditions can occur due to the seasonality of the wave climate, or in this case, by the sheltering effect of the nourishment. The onshore migration caused the SPAW to attach to the inner sandbar and to the initiation of a second SPAW, which, on its turn, migrated shoreward. Finally, this second SPAW attached to the shoreline.

- After the completion of the nourishment in March 2019, no new sediment volumes were deposited in the nearshore zone of New Smyrna Beach. This allowed the system to form alongshore continues sandbars. In time, the system is trying to return to its original state, leading to an onshore migration of the sandbar in cross-shore direction. (Figure 7.3, iv). The onshore migration can also be seen in Figure 7.4.

This research aimed to find indications of the Feeder effect by comparing the migration results of the berm/bar to wave energy fluxes. Although no one-to-one relationships were found, the Argus imagery data illustrates the onshore migration of the nourishment clearly. Additionally, the hypothesized SPAWs cause accretion to the beaches of New Smyrna. The combination of onshore berm migration and the feeding of the shoreline is the exact definition of the Feeder effect. The hypothesized migration of the nourishment, sandbars, and SPAW's is schematized in Figure 7.4. Therefore, it is suggested that the Feeder effect plays an essential role in the shoreline dynamics of New Smyrna Beach.

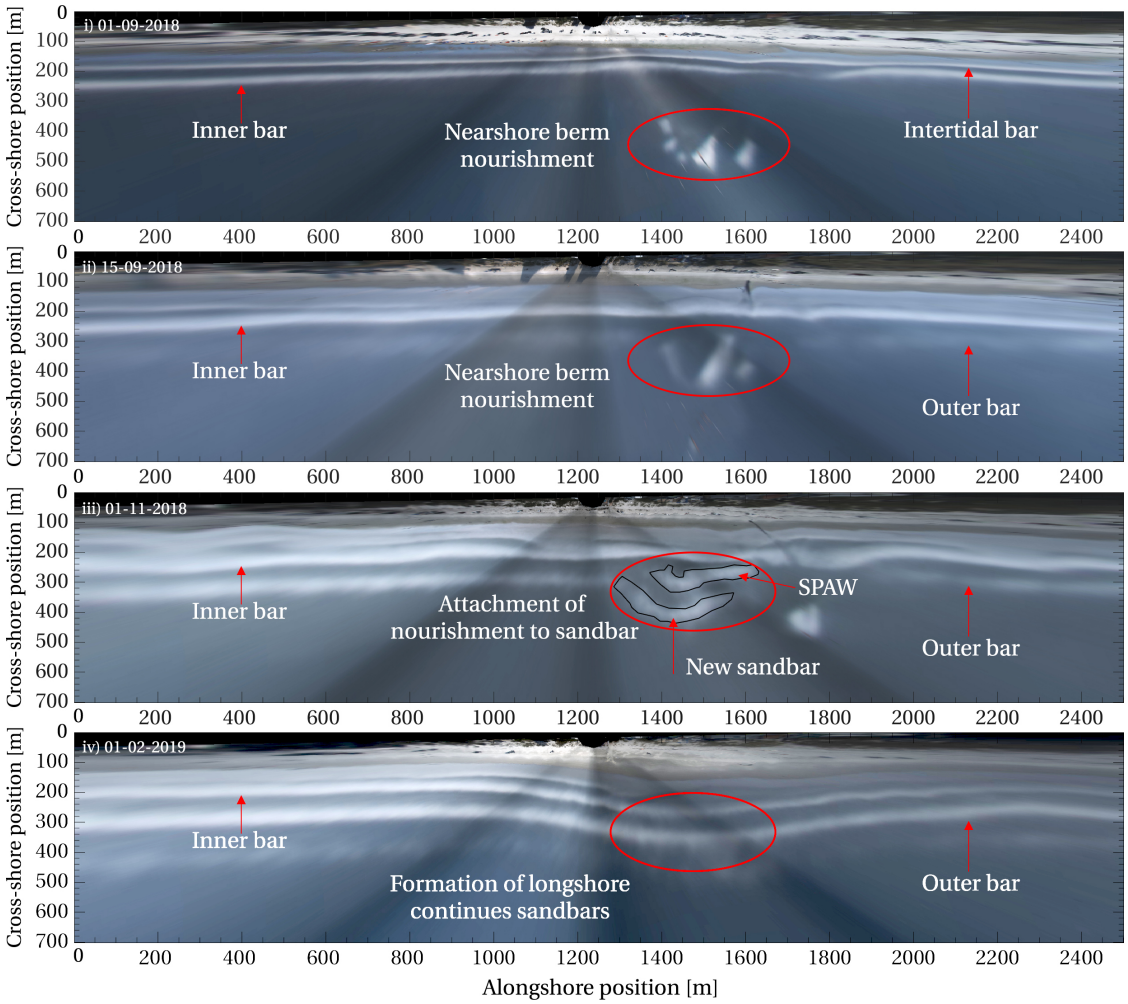

Figure 7.3: Timex imagery of NSB on September 1, 2018 (i); September 15, 2018 (ii); November 1, 2018 (iii); February 02, 2019 (iv), illustrating the migration of the nearshore berm and sandbars.

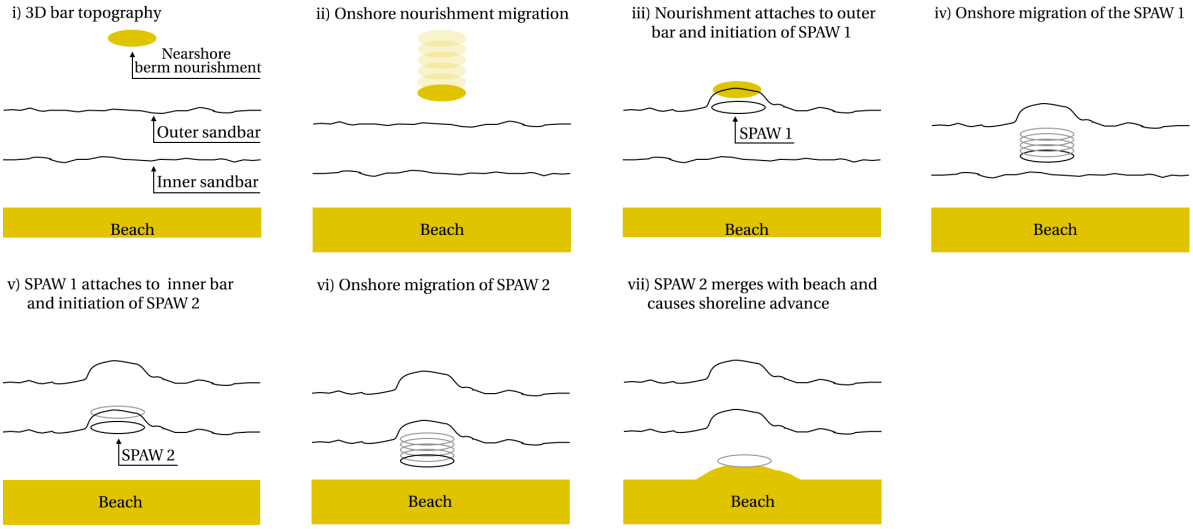

Figure 7.4: The migration of the nearshore berm nourishment, outer sandbar, inner sandbar, SPAWs, and shoreline characterize the hypothesized Feeder effect at New Smyrna Beach.

7.1.3. The Leeside effect

No one-to-one relationships were found between the downdrift shoreline migration and alongshore wave energy fluxes at New Smyrna Beach. This implies that significant downdrift shoreline migration was not necessarily linked to individual oblique energetic wave events. However, two strong indications of the Leeside effect were found.

First, clear erosion/accretion patterns at the side of the developing shoreline bulge were observed (Figure 5.12). These erosion patterns were found downdrift of the shoreline bulge, which matches the described relation between shoreline migration and alongshore wave energy of the Leeside effect (Mulder et al., 1995). Second, the shoreline positions in December and April further strengthen the suggested presence of the Leeside effect (Figure 7.6, middle, and bottom). Both shorelines are shaped similarly to the theoretically expected shoreline of the Leeside effect. For clarity, the shoreline at the start of nourishing is also displayed (Figure 7.6, top). Theoretically, the presence of the Leeside effect at New Smyrna Beach could also be suggested by comparing the time-series of alongshore wave energy fluxes with the alongshore location of the most seaward extend of the shoreline bulge. However, any potential correlation between the two is distorted due to the varying alongshore location of sediment deposition (Figure 7.5).

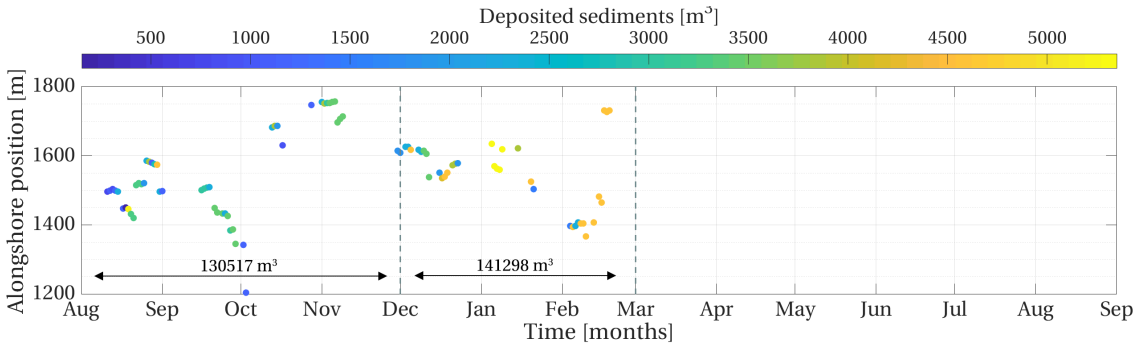

Figure 7.5: The volume of sand place in the nearshore zone of New Smyrna Beach varied in time and alongshore location.

Potentially, the Leeside effect can be influenced by other processes. For example, at New Smyrna Beach, a possible explanation of the significant difference between the two downdrift erosion levels may lie in the volume of deposited sediments (Figure 7.5). The cumulative amount of placed sediment on April 02, 2019, was approximate twice the size of that on December 01, 2018. According to the Leeside effect, the main reason for

shoreline erosion is the decrease and subsequent increase in sediment transport capacity, which is caused by the sheltering of the nourishment. Because the nourishment was smaller in December than in April, less erosion would be expected. Another possibility would be the increased blocking effect of the shoreline bulge. Similar to the Leeside effect, the blocking effect results in a reduction of the alongshore current, and, therefore, to downdrift erosion (Bosboom and Stive, 2015). Compared to April, the most shoreward extent was relatively small in December, leading to less erosion. Lastly and less applicable to New Smyrna Beach, high angle waves for which transport decreases for increasing wave angles can result in the growth of the shoreline bulge (Ashton and Murray, 2006). This positive feedback can only occur at relative wave angles larger than 45 degrees (Figure 7.8, right).

This research aimed to find indications of the Leeside effect by comparing the migration results of the shoreline to the alongshore wave energy. Although no one-to-one relationships between observed the shoreline erosion and the alongshore wave energy fluxes were established, the general trend matched the definition of the Leeside effect. Additionally, the Timex of December 2018 and April 2019 data further strengthen the suggested presence of the Leeside effect. Until this moment, the presence of the Leeside effect was only suggested during a nearshore berm placement at Egmond, The Netherlands (van Duin et al., 2004b).

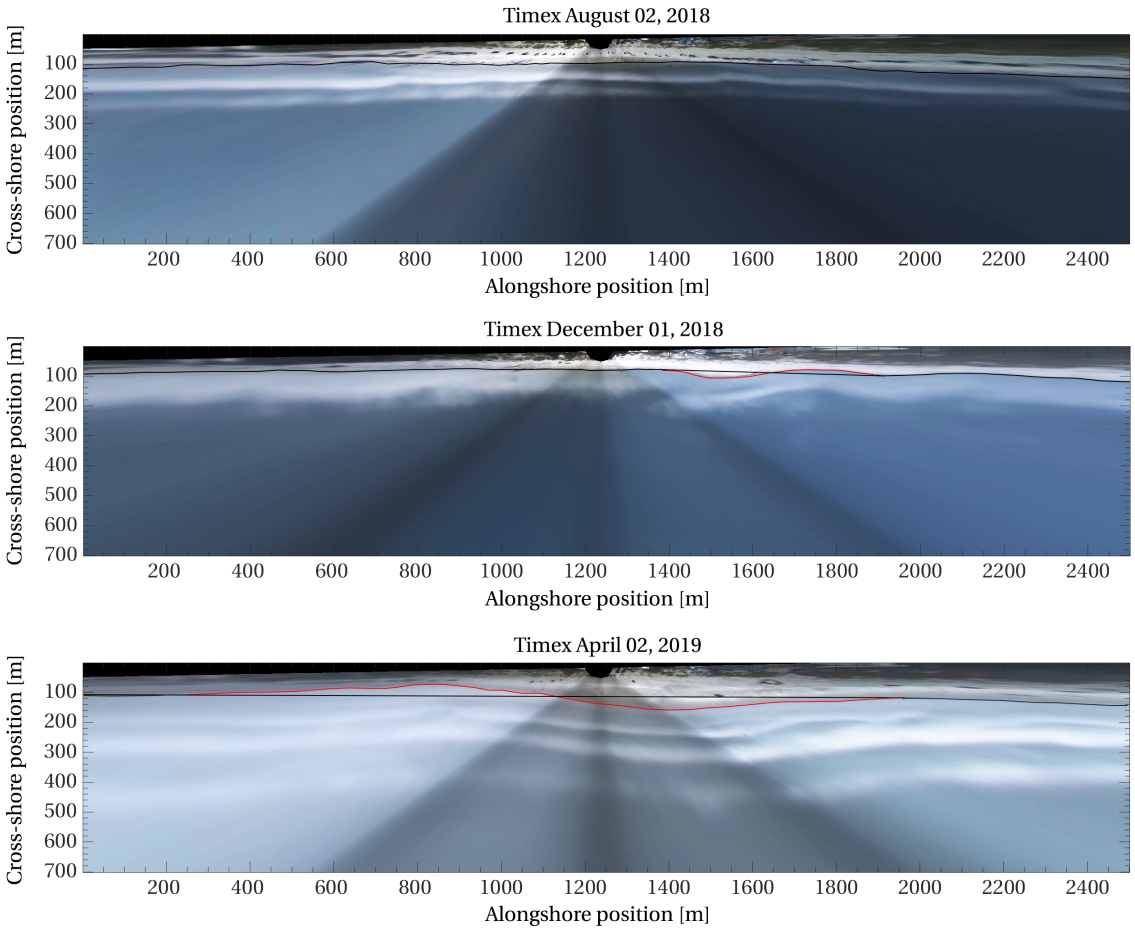

Figure 7.6: Timex imagery of New Smyrna Beach on August 02, 2018, December 01, 2018, and April 2, 2019, illustrating the development of the shoreline shape and the suggested influence of the Leeside effect.

7.1.4. Efficiency of nearshore berm nourishments

The observed increase of beach width behind the nearshore berm nourishment is relatively rare. Until now, only 1 out of 27 analyzed nearshore berm nourishments resulted in a significant increase of the sub-aerial beach (Brutsché et al., 2014). The low efficiency is underlined by Van Rijn (2011), stating that the ratio of initial nourishment volume and sediment increase in the beach zone (-1 to +3 meter above mean sea level)

due to a nearshore berm nourishment is about 2 % to 5 % after 3 – 5 years. However, at New Smyrna Beach, a clear increase in the dry beach area was already found after three months. Two months after finishing of the nourishment activities, the maximum increase of beach surface area was reached: 45,000 m^2 (Figure 7.7). After six months, the area was reduced by 1/3 to a value of 30,000 m^2. Although the exact efficiency of the nourishment cannot be calculated due to the lack of bathymetry data, it is evident that the shoreline response is more distinct compared to earlier observations.

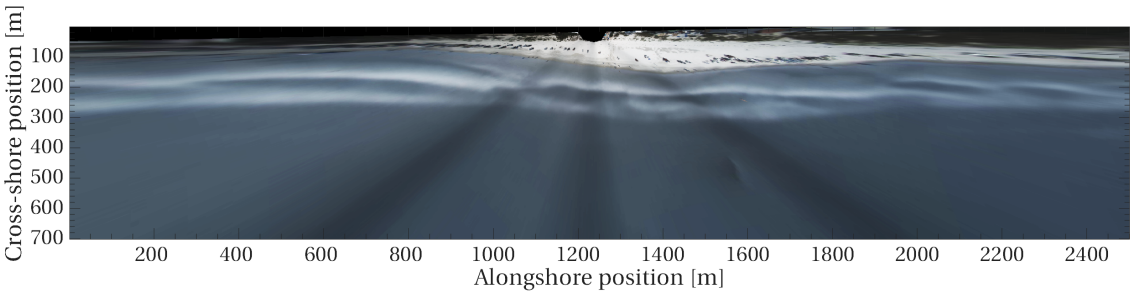

Figure 7.7: Timex imagery of New Smyrna Beach on May 01, 2019, illustrating the maximal shoreline advance due to the nearshore berm nourishment.

Based on the reduction of 15,000 m^2 in 4 months, it can be predicted that the beach will return to its original state within a year. However, theoretically, the erosion rates of a shoreline perturbation reduce in time. This can be explained by describing the alongshore and cross-shore erosion components. In the alongshore direction, the erosion of the shoreline bulge depends on the wave angle relative to the coast (Ashton and Murray, 2006). With relative wave angles lower than 45 degrees, the crest of the shoreline bulge will erode, while accretion occurs upstream and downstream (Figure 7.8, left). In time, the diffusion of the bulge leads to lower relative wave angles, and, therefore, to lower erosion rates. In the cross-shore direction, the increased beach volume due to the nourishment decays exponentially and initial losses up to 25 % of the total nourished volume can be expected (Verhagen, 1996). Therefore, according to theory, it is predicted that the increased beach surface area will erode more slowly in time. After 3.5 years, 10 % of the maximum increased beach surface area should still be present (Verhagen, 1996).

Various reasons can be the cause of the larger observed effect of the nearshore berm on the shoreline of New Smyrna Beach. An explanation may lie in the fact that there are strong indications of both the Feeder and Leeside effects. Regarding the Feeder effect, it is not uncommon to find suggestions at the shallow placements. The relation between the Feeder effect and placement depth was described earlier by Hallermeier (1981). However, the effects of the Leeside are observed less often. For instance, no signs of the Leeside effect were observed during two extensive research of nearshore berm nourishments placed at a similar depth (Brutsché et al. (2014), Hoekstra et al. (1997)). Although to a lesser extent than at New Smyrna Beach, the berm's function as a sediment source (Feeder effect) was confirmed for both cases. One distinct difference between the three placements is the cross-shore nourishment density: NSB $\approx 875 m^3/m$, Egmond $\approx 375 m^3/m$, Terschelling $\approx 475 m^3/m$. This implies that, besides the placement depth, the cross-shore density of the nourishment might play an important role in the presence and strength of the Feeder and Leeside effects. However, the validation of this statement is not in the scope of this study.

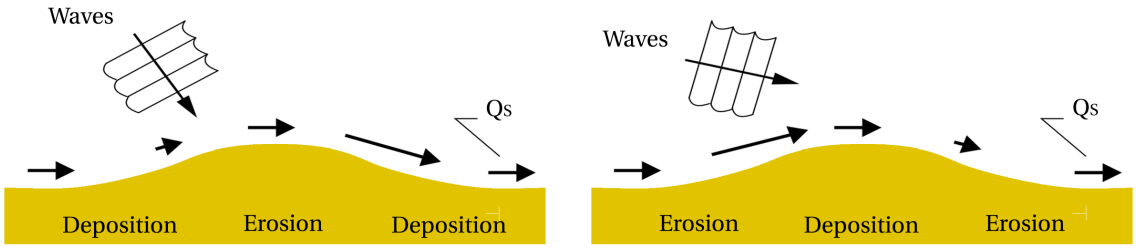

Figure 7.8: Illustrations describing the shoreline shape in relation with the incoming wave angle. Wave angles lower than 45 ° relative to the coast cause negative feedback (left), while angles larger than 45 ° result in positive feedback (right). Adapted from: Ashton and Murray (2006).

7.2. Assumptions and inaccuracies

This section discusses the inaccuracies and uncertainties of the extraction approach of the sediment outflow, berm/bar, and shoreline positions in sequence.

7.2.1. Sediment outflow positions

The sediment outflow position extraction method used several assumptions to obtain the location of the pipe outflow. First, it assumed no relocation of the pipeline throughout the day. Second, the center of gravity of the pipe outflow was tracked manually. Both the assumption and the extraction method involve positions uncertainties. Furthermore, it was possible to track 74 % of the days at which nourishment activities took place. This leaves 26 % of the days at which deposited sediments could not be assigned to a deposition location. The sediment outflow positions were only used for interpreting the migration time-series of the berm/bar and shoreline. Therefore, any (incorrect) assumptions and untracked days will not one-to-one lead to significant inaccuracies further in the study.

7.2.2. Nearshore berm/bar positions

The BLIM model was used for the nearshore berm position extraction. The model approach was tested for the four Argus imagery types, and the optimal type was selected based on visual inspection. However, an empirical comparison between the found locations of persistent wave breaking and the actual berm/bar crest would provide a more reliable selection.

Additionally, the extraction approach used several assumptions. The most important is the relation between wave breaking and underlying bathymetry. In unsaturated wave climates, the berm crest corresponds well with the location of persistent wave breaking. However, in the case of a saturated wave climate, the deviation between both locations increases to a difference in the order of 10 meters. Therefore, the input imagery data set was restricted to water level and wave height. However, to secure a sufficient temporal density of the output, saturated wave conditions were not ruled out. Furthermore, observing larges waves using video imagery has more uncertainty then smaller waves. Large waves violate the flat water surface (used during the georectification process) assumption more, resulting that wave breaking areas appear more smeared in the offshore direction. Also, larger waves break further offshore, where the pixel resolution is worse, which again leads to more smearing.

Concludingly, the potential variability between the measured berm/bar positions and actual positions is largest with energetic wave conditions, and lead to overestimated (offshore) migration rates. Regarding the research, this can lead to more difficulty in finding consistent relationships between hydraulic forcing and berm/bar migration. The selection of the Timex based on visual inspection will not have significant consequences because the use of Timex is already validated in other literature.

7.2.3. Shoreline positions

Most automated shoreline detection models had difficulties in defining the shoreline of New Smyrna Beach. Although each model algorithm was based on different site characteristics, non led to accurate results. This can be explained in two-fold. One, the site characteristics did not match the characteristics at which the models were developed and validated. Two, the input imagery contained features which complicated the shoreline extraction. Both statements were (partly) true. The SLIM and CCD models were developed using shorelines which site characteristics differ significantly from New Smyrna Beach, which makes the possibility of an accurate shoreline extraction less likely. Additionally, the Imagery data set of New Smyrna Beach contains much beach noise (beach-goers, parasols, vehicles) and has a varying brightness level throughout the image (a result of the merging process). Moreover, it has been found that the percentage of succeeding of the shoreline detection models varies significantly on the site characteristics (Plant et al., 2007). Altogether, it is not surprising that tested shoreline detection models did not result in accurate shoreline positioning.

Besides the automated shoreline detection models, a manual determination approach was tested. In line with the manual determination approach for the sediment outflow positions, it was tested by one person. Therefore, the resulting shorelines are subjective. This can cause incorrect and biased shoreline position time-series, which, on its turn, can lead to a more challenging to establish relationship with the hydraulic forcing. Furthermore, the shoreline obtained from the manual determination approach had a spatial point density of 1 in 50 meters. In other words, this approach assumes a constant shoreline within 50 meters, something which is unlikely to be true.

8

Conclusions

By analyzing the nearshore berm nourishment of 2018 at New Smyrna Beach, this research aimed to increase the understanding of the development of nearshore berm nourishments in relation with the corresponding shoreline evolution. The objective of the thesis was translated into the main research question:

How does a nearshore, concentrated berm nourishment influence the beach during and after nourishment activities?

The conclusions and recommendations of the research are described in this chapter. First, the conclusions of the three research sub-questions are stated. Together, they answer the main research question. Second, recommendations for future research are given.

8.1. Converting images to berm and shoreline positions

This section answers the research sub-question "How can the nearshore berm and the shoreline positions be optimally extracted from the New Smyrna Beach imagery data?". The extraction methods of the sediment outflow positions, nearshore berm positions, and shoreline positions are discussed in order.

Sediment outflow position extraction

The monitoring starting point of the nearshore berm were the placement locations. From August 2018 to March 2019, sand was deposited in the nearshore zone of New Smyrna Beach via a pipeline. The visibility of the pipe outflow on georectified and merged Snapshots, Timex, Variance, Brightest, and Darkest imagery types were compared to find the type that resulted in the most accurate outflow positions. The 10-minute averaging effect of the Timex imagery canceled most noise and resulted in the cleanest image compared to other imagery types. Additionally, the pipeline location on the Timex imagery represents the average location, which removes the variability in the pipeline position due to wave motions while sampling. In 74 % of the time, it was possible to obtain the outflow position via manual determination. The estimated precision of the manual determination approach is in the order of 5 meters.

Nearshore berm position extraction

The BLIM model was found to be an accurate approach to extract the nearshore berm positions from the Argus imagery data. The model assumes that the locations of wave breaking correspond with the locations of the nearshore berm crest. However, using the imagery data, the sub-tidal bar and the nourishment berm cannot be seen as separate entities and are therefore analyzed as one (the berm/bar positions). It was chosen to monitor the nearshore berm positions near the local inner sandbar. The Timex, Variance, Brightest, and Darkest imagery types were tested to find the input type that resulted in the most accurate nearshore berm positions during alternating wave conditions. The Timex imagery was found to be the only imagery type that delivered accurate berm/bar positions during mildly energetic and energetic wave conditions. To remove potential inaccurate berm/bar migration due to varying water levels, the Timex imagery data-set was filtered to water level and wave height. Additionally, Timex images with insufficient image quality (sun-glare, fog, broken cameras, etc.) were manually rejected. Eventually, this led to a time-series of 359 berm/bar positions in the alongshore, which is, on average, once a day. The estimated accuracy of the used approach was in the

order of 10 meters.

Shoreline position extraction
Four extraction approaches were tested to find the optimal method for converting imagery data to shoreline position time-series. The SLIM model turned out to be unsuitable for the New Smyrna Beach site, while the CCD and PIC models did not lead to accurate and consistent shoreline positions. On the other hand, the manual extraction approach showed promising results and was therefore selected to use. The shoreline was defined as the visual separation line between water and sand. The Timex imagery type displayed this separation line most consistently, and was, therefore, used as the input type. The image contrast and blue tones were increased to improve the visibility of the separation line between sand and water. To remove potential inaccurate shoreline migration due to varying water levels, the Timex imagery data-set was filtered to water level and wave height. Eventually, this led to a time-series of 165 shoreline positions, which is, on average, once every three days. The estimated precision of the manual determination approach is in the order of 10 meters.

8.2. Description of the nearshore berm and shoreline migration

This section answers the research sub-question "How did the nearshore berm and shoreline migrate during and after the nourishment activities?" by stating the theoretical expected migration behavior, and subsequently, the migration behavior found in the imagery time-series.

Migration behavior based on theory
Based on the wave climate, nourishment location, and nourishment characteristics, the nearshore berm nourishment at New Smyrna Beach was classified as active, which corresponded to a theoretical shoreward migration of the berm. Because of this active classification, the shoreline was expected to migrate seawards in the area near the nourishment placement, and shoreward downdrift of the placement area.

Migration behavior based on imagery time-series
The conversion of the imagery data to time-series led to 359 berm/bar positions with an accuracy of order 10 meters and 165 shoreline positions with an approximated precision of order 10 meters. Both time-series were used to describe the berm/bar and shoreline migration during the nourishment operation (August 2018 – March 2019) and after completion (March 2019 – September 2019).

In September 2018, one month into the nourishment activities, offshore berm/bar migration was found near the alongshore center of gravity of the nourishment. This development continued till February 2019, at which the maximal offshore berm/bar position of 150 meters relative to the surrounding coastal stretches was found. Afterward, the berm/bar gradually moved shoreward again. In September 2019, the berm/bar near the alongshore center of gravity of the nourishment had almost returned to its original position.

In November 2018, four months into the nourishment activities, the first shoreline advance was noticed near the alongshore center of gravity of the nourishment. The advance continued till May 2019, followed by a period of stable shoreline positioning. Eventually, at this location, the start of shoreline retreat was found in August 2019. Changes in beach width varied in the alongshore direction with the north side occasionally displaying different behavior than the south side. From August 2018 to April 2019, shoreline retreat up to 20 meters was found at the north side of the shoreline bulge. On the south side, the erosion values were less, and even shoreline accretion occurred. In the remaining months, an opposite behavior was found, resulting in more erosion at the south side and north at the right. In total, the maximum shoreline increase was nearly 80 meters (May), and the final shoreline increase approximately 50 meters (September). In total, the beach gained more than 3,000 m^2 of surface area, spread over 1.2 kilometers.

8.3. Influence of the hydraulic forcing on the nearshore berm and shoreline migration

This section answers the research sub-question "What is the influence of the hydraulic forcing on the nearshore berm and shoreline migration?" by stating the influence based on theory, and subsequently, the influence found in the imagery time-series. Finally, the theoretical description is tested on the empirical found relationships.

Influence based on theory
Theoretically, the influence of hydraulic forcing on berm/bar and shoreline migration can be described by the Feeder and Leeside effects. Both two effects were used to describe the theoretical influence of the hydraulic forcing on the nearshore berm and shoreline migration of New Smyrna Beach. The influence was described at two positions.

- Near the alongshore center of gravity of the nourishment: normally incident waves cause onshore berm migration and shoreline advance.
- Outside the sheltered area: incident waves cause downdrift shoreline erosion.

Influence based on imagery time-series
The cross-shore and alongshore wave energy fluxes F_x and F_y were used to characterize the influence of the hydraulic forcing on the nearshore berm/bar and shoreline position time-series. The relation between wave direction and the sign of the alongshore wave energy fluxes is illustrated in Figure 8.1. In words, positive alongshore wave energy fluxes are related to waves coming from the south-east-east to north-east-east, while negative alongshore wave energy correspond with waves coming from the north-east-east to north-north-east.

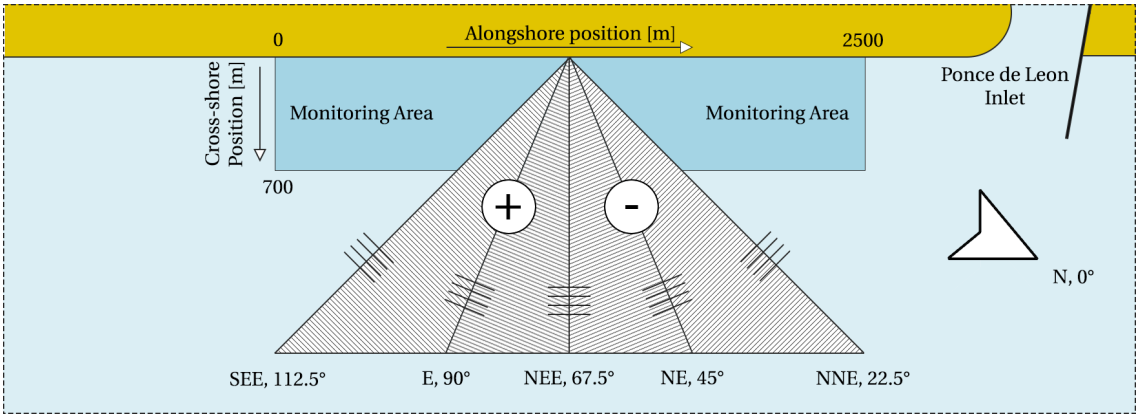

Figure 8.1: A schematic reproduction of the nearshore zone of New Smyrna Beach. The angle of incidence during the monitoring period varied between 22.5° and 112.5°.

Outside and south of the sheltered area, negative alongshore wave energy events corresponded with shoreline erosion. Additionally, positive alongshore wave energy coincided with relatively stable shoreline positioning (order 5 meters). Exceptions were two positive wave energy events in August/September 2019, which led to both erosion and accretion.

At the alongshore center of gravity of the nourishment, offshore berm/bar migration corresponded with cross-shore wave energy (August 2018 to March 2019). From March to September 2019, the relation flipped and onshore berm migration coincided with cross-shore wave energy. Furthermore, the shoreline migration at this transect was stable from August to November 2018. From November to May 2019, shoreline advance co-occurred with cross-shore wave energy events. After a period with low wave energy and stable shoreline positioning, instant shoreline erosion and accretion were found in September 2019. This coincided with, respectively, a low and high wave energy event.

Outside and north of the sheltered area, the majority of the positive alongshore wave energy events corresponded with shoreline erosion. The wave event in September 2019 was an exception; positive alongshore wave energy coincided with stable shoreline positioning. Additionally, shoreline accretion was found during negative alongshore wave energy events.

Comparison influence based on theory and time-series
It was aimed to find indications of the theoretical influence of the hydraulic forcing in the berm/bar and shoreline migration time-series.

Outside and south of the sheltered area, strong indications of the theoretical influence were found in the shoreline migration and wave energy flux time-series. Between August 2018 to September 2019, 72 % of the

total negative wave energy was related to shoreline retreat.

At the alongshore center of gravity of the nourishment, indications of the theoretical influence were found in the berm/bar, shoreline migration, and wave energy flux time-series. During 34 % of the time, onshore berm migration corresponded with shoreline advance. Additionally, 33 % of the cross-shore wave energy could be related to this migration behavior. Onshore berm migration and shoreline advance occurred mostly after finishing of the nourishment (March to September 2019).

Outside and north of the sheltered area, strong indications of the theoretical influence were found in the shoreline migration and wave energy flux time-series. Between August 2018 to September 2019, 61 % of the total positive wave energy was related to shoreline retreat. Furthermore, it was visually determined that most shoreline advance occurred from August 2018 to February 2019, and most shoreline retreat from February to September 2019.

8.4. Answer to research question

The research question "How does a nearshore, concentrated berm nourishment influence the beach during and after nourishment activities?" was answered in two-fold:

Shoreline evolution
During the nourishment activities, the nearshore berm nourishment caused the development of a bulge shaped shoreline. One month after completion, the most offshore extent of the bulge grew to a maximal position of 80 meters relative to August 2018 and the surrounding coastal stretches. In September 2019, six months after completion, 50 of the in total 80 meters of shoreline advance remained. The bulge itself had an estimated alongshore width of more than 1.2 kilometers and a dry surface area over 3,000 m^2. During the total monitoring period, alternating shoreline retreat up to 20 meters was found downdrift of the shoreline bulge.

Shoreline mechanisms
Several mechanisms influenced the New Smyrna Beach during and after completion of the nourishment. In the cross-shore direction, both the Feeder and Leeside effects were suggested to cause shoreline advance near the nourishment. Both effects were suggested to influence the shoreline more strongly during the nourishment activities and decrease in influence after completion. In the alongshore direction, the Leeside effect was suggested to imply shoreline erosion downdrift of the sheltered zone. Additionally, in time, the developed shoreline bulge diffused and caused the feeding of adjacent beaches with sediments.

8.5. Recommendations

This research aimed to increase the understanding of the development of nearshore berm nourishments in relation with the corresponding shoreline evolution. The relation was described for New Smyrna Beach, but to further improve the understanding, additional research is needed. The recommendations are divided into suggestions concerning future nearshore berm nourishments at New Smyrna Beach and the research to increase the understanding of the Feeder and Leeside effects.

Recommendation considering nearshore berm nourishments at New Smyrna Beach

- If the beach state is not an acute problem, it is recommended to nourish in the more calm wave season (May – September). The period in which the nourishment activities take place contributes to the response of the shoreline. Normally, placement during high energy conditions (September to May) will lead to a faster shoreline response compared to low wave energy conditions. However, the operational working conditions are more difficult due to the significant wave breaking. Storms can lead to unworkable conditions, which eventually elongate the period of nourishing, and thus, cost money.
- Recommendations concerning the shape and placement location can be made for future nearshore berm nourishments placed by pipe outflow at New Smyrna Beach. A compact shape of nearshore berm nourishments is preferred over an alongshore elongated shape. The decrease and subsequent increase of sediment transport capacity at the edges of the shadow zone of the nourishment lead to shoreline erosion. To minimize this shoreline erosion, the size of the shadow zone has to be limited. Additionally, a shallow placement in the surfzone is suggested over a placement in deeper water. The wave breaking and wave shoaling result in sediment transport in shoreward direction.

Recommendation to increase the understanding of the relation between nearshore berm and shoreline

- Future research on image to data extraction is suggested. Argus imagery data is an excellent source for investigating long-term effects such as the Feeder and Leeside effects. However, most available imagery extraction methods are only capable of generating accurate outcome if the site conditions match the conditions of the development site. Because this is rarely the case, additional research on Artificial Neural Network (ANN) models is suggested. In contrary to most models, an ANN is not developed on a specific site, and should, therefore, be applicable for all conditions. Furthermore, to overcome variable image brightness due to the sun and overlap areas from merging, the use of obliques is recommended.
- Alongshore current and/or sediment transport measurements are suggested to be used in further studies to examine the presence and importance of the Leeside effect on shoreline development. This research indicated the presence of the Leeside effect by examining the shoreline migration with the hydraulic forcing time-series. As an assumption, the alongshore wave energy was used as an approximation for the alongshore current. However, the use of alongshore current or alongshore sediment transport measurements would lead to a more accurate relation description. A possible method for obtaining an alongshore current estimation is by a video-based particle image velocimetry (Holland et al., 2001). Compared to this study, imagery data with a higher temporal density, e.g. 2.5 Hz, is required to generate flow vectors.
- The use of stereo analysis is suggested as an overall recommendation to analyze the development of nearshore berm nourishments in relation with the corresponding shoreline. Stereo analysis, or stereoscopy, is a technique that extracts 3D-information from overlapping images, acquired from different locations. In addition to berm and shoreline positions, bathymetry, and wave height estimation can be generated from the Argus imagery data (). This extra information will result in a more detailed relation description between the wave climate and dynamics in the morphology.

References

Aarninkhof, S. G. J. (2003). *Nearshore Bathymetry derived from Video Imagery*. PhD thesis, TU Delft.

Aidala, J. A., Burke, C. E., and Mclellan, T. N. (1992). Hydrodynamic Forces and Evolution of a Nearshore Berm at South Padre Island, Texas. In *Hydraulic Engineering: Saving a Threatened Resource—In Search of Solutions*, pages 1234 – 1239.

ASBPA, APTIM, and USACE RSM (2018). National Beach Nourishment Database.

Ashton, A. D. and Murray, A. B. (2006). High-angle wave instability and emergent shoreline shapes: 1. Modeling of sand waves, flying spits, and capes. *Journal of Geophysical Research: Earth Surface*, 111(4):1–19.

Beck, T. M., Rosati, J. D., and Rosati, J. (2012). An Update on Nearshore Berms in the Corps of Engineers: Recent Projects and Future Needs. Technical report, U.S. Army Engineer Research and Development Center, Vicksburg, MS.

Bokuniewicz, H. J., Gebert, J., Gordon, R. B., Kaminsky, P., and Pilbeam, C. C. (1977). Field study of the effects of storms on the stability and fate of dredged material in suqaqueous disposal areas. Technical report.

Bosboom, J. and Stive, M. M. J. (2015). *Coastal dynamics I*. VSSD, Delft, 15 edition.

Browder, A. E. and Dean, R. G. (2000). Monitoring and comparison to predictive models of the Perdido Key beach nourishment project, Florida, USA. *Coastal Engineering*.

Bruder, B., Brodie, K., Spore, N., Renaud, A., and Hodgends, K. (2019a). Continious monitoring of a nearshore berm placement at New Smyrna Beach, FL via coastal imagery. In Wang, Ping (University of South Florida, U., Rosati, Julie D. (US Army Corps of Engineers, U., and Vallee, Matthieu (University of South Florida, U., editors, *Coastal Sediments 2019*, pages 2443–2457, Tampa/St. Petersburg, Florida. World Scientific.

Bruder, B., Hathaway, K., and Brodie, K. (2019b). Design and Deployment of Mini-Argus Systems for Rapid Coastal Imaging. Technical report, U.S. Army Engineer Research and Development Center.

Bruins, R. (2016). *Morphological behaviour of shoreface nourishments along the Dutch coast*. PhD thesis, TU Delft.

Brutsché, K. E., Mcfall, B. C., Bryant, D. B., and Wang, P. (2019). Literature Review of Nearshore Berms. Technical report, U.S. Army Engineer Research and Development Center.

Brutsché, K. E., Wang, P., Beck, T. M., Rosati, J. D., and Legault, K. R. (2014). Morphological evolution of a submerged artificial nearshore berm along a low-wave microtidal coast, Fort Myers Beach, west-central Florida, USA. *Coastal Engineering*, 91:29–44.

Caulk, A., Gannon, J., Shaw, J., and Hartig, J. (2000). *Best management practises for soft engineering of shorelines*. Greater Detroit American Heritage River Initiative, Detroit, Michigan.

Cheng, J., Wang, P., and Smith, E. (2016). Hydrodynamic Conditions Associated with an Onshore Migrating and Stable Sandbar. *Journal of Coastal Research*, 32(1):153–163.

Clark, R. (2019). Critically Eroded Beaches in Florida. Technical report, FDEP.

Delft Hydraulics (2001). Longshore Sand Transport. Technical report, Deltares (WL).

Dronkers, J. (2016). *Dynamics of Coastal Systems*, volume 25 of *Advanced Series on Ocean Engineering*. WORLD SCIENTIFIC, Singapore, Singapore, second edi edition.

Foster, G. A., Healy, T. R., and Lange, W. P. D. (1994). Sediment Budget and Equilibrium Beach Profiles Applied to Renourishment of an Ebb Tidal Delta Adjacent Beach, Mt. Maunganui, New Zealand. *Journal of Coastal Research*, 10(3):564 – 575.

Guedes, R. M., Calliari, L. J., Holland, K. T., Plant, N. G., Pereira, P. S., and Alves, F. N. (2011). Short-term sandbar variability based on video imagery: Comparison between Time-Average and Time-Variance techniques. *Marine Geology*, 289(1-4):122–134.

Hall, J. V. and Herron, W. J. (1950). Test of nourishment of the shore by offshore deposition of sand. Technical report.

Hallermeier, R. J. (1981). A profile zonation for seasonal sand beaches from wave climate. *Coastal Engineering*, 4(0378-3839):253–277.

Hamm, L., Capobianco, M., Dette, H., Lechuga, A., Spanhoff, R., and Stive, M. (2002). A summary of European experience with shore nourishment. *Coastal Engineering*, 47(2):237–264.

Hands, E. B. and Allison, M. C. (1991). Mound Migration in Deeper Water and Methods of Categorizing Active and Stable Depths. Technical report.

Harley, M. D., Kinsela, M. A., Sánchez-García, E., and Vos, K. (2019). Shoreline change mapping using crowdsourced smartphone images. *Coastal Engineering*, 150(April):175–189.

Healy, T., Harms, C., and de Lange, W. (1991). Dredge spoil and inner shelf investigations off Tauranga Harbour, Bay of Plenty, New Zealand. *Coastal Sediments '91; Volume 2*, (July):2037–2051.

Hoefel, F. and Elgar, S. (2003). Wave-Induced Sediment Transport and Sandbar Migration. *Science*, 299:1885 – 1887.

Hoekstra, P., Houwman, K., Kroon, A., Ruessink, B., Roelvink, J., and Spanhoff, R. (1997). Morphological Development of the Terschelling Shoreface Nourishment in Response to Hydrodynamic and Sediment Transport Processes. In *Coastal Engineering 1996*, volume 3, pages 2897–2910, New York, NY. American Society of Civil Engineers.

Holland, K. T., Holman, R. A., Lippmann, T. C., Stanley, J., and Plant, N. (1997). Practical Use of Video Imagery in Nearshore Oceanographic Field Studies. *IEEE Journal of Oceanic Engineering*, 22(1):81 – 92.

Holland, K. T., Puleo, J. A., and Kooney, T. N. (2001). Quantification of swash flows using video-based particle image velocimetry. *Coastal Engineering*, 44(2):65–77.

Holman, R. A., Sallenger Jr, A. H., Lippmann, T. C., and Haines, J. W. (1993). The Application of Video Image Processing to the Study of Nearshore Processes. *Oceanography*, 6(3):75–85.

Holman, R. A. and Stanley, J. (2007). The history and technical capabilities of Argus. *Coastal Engineering*, 54(6-7):477–491.

Huisman, B., Van Thiel de Vries, J., Walstra, D., Roelvink, J., Ranasinghe, R., and Stive, M. (2013). Advection and diffusion of shore-attached sand nourishments. *Coastal Dynamics*, (June):845–858.

Huisman, B. J., Walstra, D. J. R., Radermacher, M., de Schipper, M. A., and Ruessink, B. G. (2019). Observations and modelling of shoreface nourishment behaviour. *Journal of Marine Science and Engineering*, 7(3).

IBRD and IDA (2020). Urban Development.

Koetje, K. M. and Palmsten, M. L. (2020). Coastal Imaging Station Design Toolbox. *SoftwareX*, 11(100377).

Kroon, A., Hoekstra, P., Houwman, K., and Ruessink, G. (1994). Morphological Monitoring of a Shoreface Nourishment Nourtec: Experiment at Terschelling, The Netherlands. *Coastal Engineering*, pages 2222 – 2236.

Larson, M. and Kraus, N. C. (1992). Analysis of Cross-Shore Movement of Natural Longshore Bars and Material Placed to Create Longshore Bars. Technical report.

Lippmann, T. C. and Holman, R. A. (1989). Quantification of Sand Bar Morphology: A Video Technique Based on Wave Dissipation. *Journal of Geophysical Research*, 94(C1):995–1011.

Mesa, C. (1996). Nearshore berm performance at Newport Beach, California, USA. In *Coastal Engineering*.

Miller, J. K. and Dean, R. G. (2007). Shoreline variability via empirical orthogonal function analysis: Part II relationship to nearshore conditions. *Coastal Engineering*, 54(2):133–150.

Mulder, J. P. M., van de Kreeke, J., and van Vessem, P. (1995). Experimental Shoreface Nourishment, Terschelling (NL). In *Coastal Engineering 1994*, volume 3, pages 2886–2899, New York, NY. American Society of Civil Engineers.

Otay, E. N. (1994). *Long-term evolution of nearshore disposal berms*. PhD thesis, University of Florida.

Pape, L. (2008). BLIM Toolbox Manual. (November):43.

Plant, N. G., Aarninkhof, S. G. J., Turner, I. L., and Kingston, K. S. (2007). The Performance of Shoreline Detection Models Applied to Video Imagery. *Journal of Coastal Research*, 233(233):658–670.

Plant, N. G. and Holman, R. A. (1997). Intertidal beach profile estimation using video images. *Marine Geology*, 140(1-2):1–24.

Price, T., van Kuik, N., de Wit, L., Dionísio António, S., and Ruessink, B. (2017). Shoreward Propagating Accretionary Waves (SPAWs): Observations from a multiple sandbar system. *Proceedings Coastal Dynamics 2017*, pages 1081–1089.

Price, T. D. and Ruessink, B. G. (2011). State dynamics of a double sandbar system. *Continental Shelf Research*, 31(6):659–674.

Quartel, S., Ruessink, B. G., and Kroon, A. (2007). Daily to seasonal cross-shore behaviour of quasi-persistent intertidal beach morphology. *Earth Surface Processes and Landforms*, 32(9):1293–1307.

Ruessink, B. G., Kuriyama, Y., Reniers, A. J., Roelvink, J. A., and Walstra, D. J. R. (2007). Modeling cross-shore sandbar behavior on the timescale of weeks. *Journal of Geophysical Research: Earth Surface*, 112(3).

Short, A. D. (1979). Three dimensional beach-stage model. *Journal of Geology*, 87(5):553–571.

Smit, M. W. J., Aarninkhof, S. G. J., Wijnberg, K. M., González, M., Kingston, K. S., Southgate, B. G., Ruessink, B., Holman, R. A., Siegle, E., Davidson, M., and Medina, R. (2007). The role of video imagery in predicting daily to monthly coastal evolution. *Coastal engineering*, 54(6-7):539–553.

Smith, W. and Jackson, L. (1990). The siting of beach nourishment placements. *Shore and Beach, American Shore and Beach Preservation Association*, 58(1):17–24.

Stive, M. J., Aarninkhof, S. G., Hamm, L., Hanson, H., Larson, M., Wijnberg, K. M., Nicholls, R. J., and Capobianco, M. (2002). Variability of shore and shoreline evolution. *Coastal Engineering*, 47(2):211–235.

Turner, I. L. and Adamantidis, C. A. (2001). Analysis of shoreline change: Northern Gold Coast Coastal Imaging System. Technical report, School of Civil and Environmental Engineering.

Turner, I. L., Leyden, V. M., Symonds, G., Mcgrath, J., Jackson, A., Janear, T., Aarninkhof, S., and Elshoff, I. (2000). Predicted and observed coastline changes at the Gold Coast artificial reef. In *Coastal Engineering 2000 - Proceedings of the 27th International Conference on Coastal Engineering, ICCE 2000*, volume 276, pages 1836–1847.

US Army Corps of Engineers (2015). Coastal Engineering Manual-Part II. Technical report.

van de Ven, D. and van Zelst, V. (2019). Biogeomorphological effects of nourishment, NL.

van Duin, M. J., Wiersma, N. R., Walstra, D. J., van Rijn, L. C., and Stive, M. J. (2004a). Nourishing the shoreface: Observations and hindcasting of the Egmond case, The Netherlands. *Coastal Engineering*, 51(8-9):813–837.

van Duin, M. J. P., Wiersma, N. R., Walstra, D. J. R., van Rijn, L. C., and Stive, M. J. F. (2004b). Nourishing the shoreface: Observations and hindcasting of the Egmond case, The Netherlands. *Coastal Engineering*, 51(8-9):813–837.

van Enckevort, I. and Ruessink, B. (2003). Video observations of nearshore bar behaviour. Part 2: alongshore non-uniform variability. *Continental Shelf Research*, 23(5):513–532.

van Enckevort, I. M. J. and Ruessink, B. G. (2001). Full Access Effect of hydrodynamics and bathymetry on video estimates of nearshore sandbar position. *Journal of Geophysical Research*, 106(C8):16969–16979.

van Rijn, L. and Walstra, D. (2004). Analysis and modelling of shoreface nourishments. Technical report.

Van Rijn, L. C. (2011). Coastal erosion and control. *Ocean and Coastal Management*, 54(12):867–887.

Vera-Cruz, D. (1972). Artificial Nourishment of Copacabana Beach. *Coastal Engineering*, pages 23 – 59.

Verhagen, H. J. (1996). Analysis of beach nourishment schemes. *Journal of Coastal Research*, 12(1):179–185.

Wijnberg, K. M. and Holman, R. A. (2008). Video-observations of shoreward propagating accretionary waves. *River, Coastal and Estuarine Morphodynamics: RCEM 2007 - Proceedings of the 5th IAHR Symposium on River, Coastal and Estuarine Morphodynamics*, 2(September):737–743.

Williams, A. T., Rangel-Buitrago, N., Pranzini, E., and Anfuso, G. (2018). The management of coastal erosion. *Ocean and Coastal Management*, 156:4–20.

Work, P. A., Asce, A., and Otay, E. N. (1996). Influence of Nearshore Berm on Beach Nourishment. In *25th International Conference on Coastal Engineering*, number 287, pages 3722–3735.

A

History of nearshore berm nourishments

This appendix illustrates the characteristics of nearshore berm nourishments from 1935 to 2010. Besides the placed volume and water depth, the berms are specified to migration type.

Table A.1: Summary of nearshore berm nourishments. Retrieved from Brutsché et al. (2019).

Location	**Year**	**Volume** $10^3[m^3]$	**Water depth [m]**	**Berm type**	**Reference**
Santa Barbara, CA	1935	154	6	stable	Hall and Herron (1950)
Atlantic City, NJ	1942	2700	5-8	stable	Hall and Herron (1950)
Long Beach, NJ	1948	460	9	stable	Hall and Herron (1950)
Durban, South African	1970	2500	7-16	stable/active	
Copacabana Beach, Brazil	1970	2000	4-6	active	Vera-Cruz (1972)
Long Island Sound, CT	1974	1170	18	stable	Bokuniewicz et al. (1977)
Lake Erie, OH	1975	18	17	stable	
New River Inlet, NJ	1976	27	2-4	active	
Tauranga Bay, New Zealand	1976	2000	11-17	stable	Healy et al. (1991)
Dam Neck, VA	1982	650	10-11	stable	
Sand Island, AL	1987	268	6	active	
Fire Island, NY	1987	350	8	x	
Jones Inlet, NY	1987	300	8	x	
Mobile, AL (outer mound)	1988	14300	11-14	s	
Coos Bay, OR	1988	4000	20-26	dispersed	
Silver Strand, CA	1988	115	5-6	active	
Kira Beach, Australia	1988	1500	7-10	active	Smith and Jackson (1990)
South Padre Island, TX	1989	335	8	active	Aidala et al. (1992)
Mt. Maunganui, New Zealand	1990	80	4-7	active	Foster et al. (1994)
Perdido Key, FL	1992	3060	5-6	stable	Otay (1994)
Port Canaveral, FL	1992	100	5-7	active	
New Port Beach, CA	1992	1275	7-8	stable/active	Mesa (1996)
Terschelling, the Netherlands	1993	2010	2-10	active	Kroon et al. (1994)
Egmond, the Netherlands	1999	900	8	active	van Duin et al. (2004a)
Ocean Beach, CA	2005	690	9-14	active	
Ft. Myers Beach, FL	2009	175	2-3	active	Brutsché et al. (2014)

B

Tidal harmonic constituents NSB

This appendix displays the harmonic constituents of Daytona Beach, located 13 kilometers north of New Smyrna Beach. The harmonics were used to predict the tide at New Smyrna Beach.

Table B.1: Tidal harmonic constituents for station 8721164, New Smyrna Beach, Florida, retrieved from the NOAA.

constituent #	**name**	**amplitude [m]**	**speed [degr/hr]**	**phase [degr]**
1	M2	1.87	28.984104	226.3
2	S2	0.31	30	241.8
3	N2	0.44	28.43973	206.9
4	K1	0.32	15.041069	121.6
5	M4	0.03	57.96821	144.8
6	O1	0.24	13.943035	131.6
7	M6	0.01	86.95232	274.4
8	MK3	0.01	44.025173	273.4
9	S4	0.02	60	293.6
10	MN4	0.01	57.423832	137.5
11	NU2	0.09	28.512583	203.1
12	S6	0.01	90	116.4
13	MU2	0.06	27.968208	215.2
14	2N2	0.06	27.895355	193.1
15	OO1	0.02	16.139101	124.9
16	LAM2	0.02	29.455626	270
17	S1	0.03	15	82.7
18	M1	0.01	14.496694	142.3
19	J1	0.02	15.585443	128.6
20	MM	0	0.5443747	0
21	SSA	0.2	0.0821373	48.7
22	SA	0.32	0.0410686	195
23	MSF	0	1.0158958	0
24	MF	0	1.0980331	0
25	RHO	0.01	13.471515	128.8
26	Q1	0.05	13.398661	129.1
27	T2	0.03	29.958933	223
28	R2	0.01	30.041067	97.3
29	2Q1	0.01	12.854286	91.3
30	P1	0.1	14.958931	120.8

C

Linear wave transformation

This Appendix describes the process for transforming the offshore wave climate nearshore, using linear wave theory. The resulting wave height and direction are used for analyzing the berm and shoreline migration patterns at New Smyrna Beach.

C.1. Input

The offshore wave data is obtained from wave buoy station 41009 of the National Data Buoy Center (NDBC). The buoy is located 90 kilometers south and 30 kilometers offshore of New Smyrna Beach. The extracted data contains the significant wave height, the direction of dominant waves, and the dominant wave period, sampled every 10-minutes. The local depth at the wave buoy is 42 meters and a breaker criterium of 0.75 is used.

C.2. Methodology

The offshore wave climate is transformed nearshore using the following assumptions: parallel depth contours, linear refraction, shoaling, and conservation of wave energy, which indicates that energy loss due to bed friction and turbulence is not incorporated. Additionally, it is expected that waves with an angle between -90 and +90 relative to the shore normal will migrate offshore.

The nearshore significant wave height H can be calculated by multiplying the offshore value H_0 with refraction coefficient K_{ref} and shoaling coefficients K_{sh} (Equations C.1, Bosboom and Stive (2015)).

$$H = K_{ref} * K_{sh} * H_0 \tag{C.1}$$

The refraction and shoaling coefficients can be calculated using Equations C.2 and C.3. The unknown variables are the nearshore angle of wave incidence, the offshore and nearshore wave group velocity. These can be found solving equations C.4.

$$K_{ref} = \left(\frac{cos(\alpha_0)}{cos(\alpha)}\right)^{\frac{1}{2}} \; ; \; K_{sh} = \left(\frac{c_{g0}}{c_g}\right) \tag{C.2}$$

$$\alpha = \sin^{-1}\left(\frac{L}{L_0} * sin(\alpha_0)\right) = \sin^{-1}\left(\frac{c}{c_0} * sin(\alpha_0)\right) \tag{C.3}$$

On its turn, the offshore and nearshore group and individual wave velocity are required. The (group) velocities can be found with Equations C.4. The nearshore values are calculated with n = 1 and the offshore values with n = 0.5.

$$\begin{aligned} &c_{g(0)} = n * c_{(0)} \,; \quad c_{(0)} = L_{(0)} / T_{(0)} \,; \quad L_{(0)} = 2\pi / k_{(0)} \,; \\ &k_{(0)} \text{ via } \omega^2_{(0)} = g k_{(0)} \tanh(k_{(0)} h) \,; \quad and \;\; \omega_{(0)} = \frac{2\pi}{T_{(0)}} \,; \end{aligned} \tag{C.4}$$

C.3. Results

Following the methodology of Section C.2, the offshore wave climate is transformed nearshore. The resulting wave heights are calculated in meters at breakpoint and the wave direction is the direction from which the wave are coming from in degrees . Figures C.1 to C.2 are displaying the offshore and nearshore parameters.

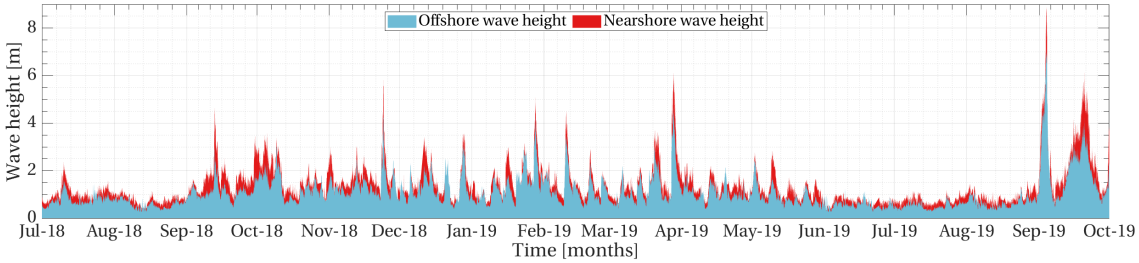

Figure C.1: The offshore and nearshore wave heights from July 2018 to October 2019 in meters.

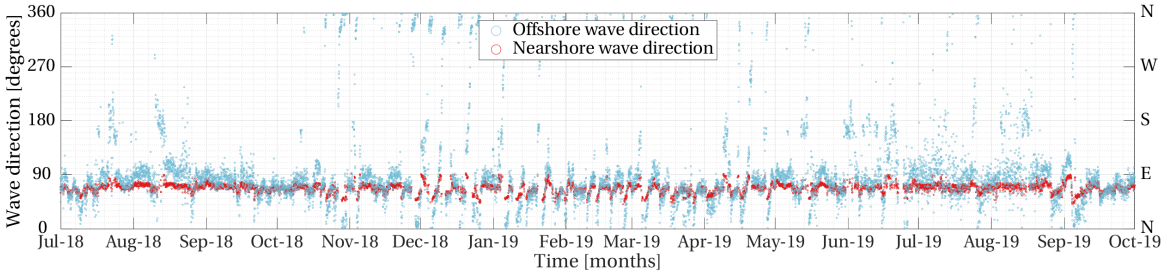

Figure C.2: The offshore and nearshore wave directions from July 2018 to October 2019 in degrees.